

GIANT MOLECULAR CLOUDS AND MASSIVE STAR FORMATION IN THE SOUTHERN MILKY WAY

P. García

Departamento de Astronomía, Universidad de Chile, Casilla 36–D, Santiago, Chile

I. Physikalisches Institut, Universität zu Köln, D-50937, Cologne, Germany

pablo@ph1.uni-koeln.de

L. Bronfman

Departamento de Astronomía, Universidad de Chile, Casilla 36–D, Santiago, Chile

Lars-Åke Nyman

Joint ALMA Observatory (JAO), Alonso de Cordova 3107, Vitacura, Santiago, Chile

European Southern Observatory (ESO), Alonso de Cordova 3107, Vitacura, Santiago, Chile

and

T. M. Dame

Harvard-Smithsonian Center for Astrophysics, 60 Garden Street, Cambridge MA 02138

Received _____; accepted 11th February 2014

Submitted to *The Astrophysical Journal*

ABSTRACT

The Columbia - U. de Chile CO Survey of the Southern Milky Way is used for separating the CO(1-0) emission of the fourth Galactic quadrant within the solar circle into its dominant components, giant molecular clouds (GMCs). After the subtraction of an axisymmetric model of the CO *background* emission in the inner Southern Galaxy, 92 GMCs are identified, and for 87 of them the two-fold distance ambiguity is solved. Their total molecular mass is $M(H_2) = 1.14 \pm 0.05 \times 10^8 M_\odot$ accounting for around 40% of the molecular mass estimated from an axisymmetric analysis of the H_2 volume density in the Galactic disk (Bronfman et al. 1988b) $M(H_2)_{disk} = 3.03 \times 10^8 M_\odot$. The large scale spiral structure in the Southern Galaxy, within the solar circle, is traced by the GMCs in our catalog; 3 spiral arm segments: the *Centaurus*, *Norma*, and *3-kpc expanding* arm are analyzed. After fitting a logarithmic spiral arm model to the arms, tangent directions at 310° , 330° , and 338° , respectively, are found, consistent with previous values from the literature. A complete CS(2-1) survey toward IRAS point-like sources with FIR colors characteristic of UC HII regions is used to estimate the massive star formation rate per unit H_2 mass (MSFR), and the massive star formation efficiency (ϵ) for GMCs. The average MSFR for GMCs is $0.41 \pm 0.06 L_\odot/M_\odot$, and for the most massive clouds in the *Norma* arm it is $0.58 \pm 0.09 L_\odot/M_\odot$. Massive star formation efficiencies of GMCs are on average 3% of their available molecular mass.

Subject headings: Galaxy: structure — galaxies: spiral — ISM: clouds — ISM: molecules — stars: massive

1. INTRODUCTION

Within the Galactic disk, at 100 parsecs scales, the molecular gas is contained mostly in the form of giant molecular clouds (GMCs) (Dame et al. 1986; Bronfman et al. 1988b; Williams & McKee 1997). The large scale clumpy structure of the CO emission in longitude-velocity diagrams is clear evidence of the organization of the gas into these large objects (Bronfman et al. 1989). The principal characteristic of GMCs is the role they play as tracers of the large scale structure in the Galaxy and as birthplaces of most of the massive stars in the Galactic disk.

As for the origin of GMCs, it is accepted that, in the disk of the Milky Way, they are formed as the molecular gas enters in the spiral wave pattern of the gravitational potential energy of the Galactic disk (Elmegreen 1994). Tidal shear forces among GMCs are weaker within the spiral arms than for the interarm regions making the gravitational collapse more feasible (Luna et al. 2006). Other mechanisms, such as the growth by collisions are, apparently, too inefficient to reproduce the observed power law mass distribution of GMCs (Elmegreen 1993; Tan et al. 2013).

GMCs are excellent tracers of large scale Galactic structure. The best example is found in the *Carina* spiral arm, traced over 20 kpc in the outer Galaxy by more than 40 GMCs, between $l = 270^\circ$ and $l = 330^\circ$ in Galactic longitude (Grabelsky et al. 1987, 1988). Dame et al. (1986) reconstructed a 3 spiral arm model for the first Galactic quadrant based on their catalog defined in CO and suggested that the containment of the largest molecular clouds in the arms demonstrates that CO emission is enhanced in the arms not only because the clouds are hotter as suggested by Sanders et al. (1985), but mainly because they are larger and contain more mass.

GMCs are the known places of massive star formation. Massive stars ($M > 8 M_{\odot}$) originate mainly inside dense, compact clumps (UC HII regions) in giant molecular clouds (Evans 1999; Mac Low & Klessen 2004; Krumholz & McKee 2005; Tan 2005; Luna et al. 2006; McKee & Ostriker 2007; Zinnecker & Yorke 2007; Schuller et al. 2010). At large scales, Bronfman et al. (2000) showed that the radial distribution of massive star forming regions follows, on average, that of the molecular gas in the inner Galactic disk for all galactocentric radii and that the massive star formation is highest at the peak of the southern “molecular ring” (understood as an azimuthally averaged molecular gas distribution of the Galactic disk), between $0.5 \leq R/R_{\odot} \leq 0.6$ in galactocentric radius. For the fourth Galactic quadrant (IVQ), Luna et al. (2006) showed that massive star formation occurs in regions with high molecular gas density, roughly coincident with the line of sight tangent to spiral arms. At smaller scales, giant molecular clouds harbor most of the massive star formation in the Galaxy (Luna et al. 2006; Mac Low & Klessen 2004; McKee & Ostriker 2007; Zinnecker & Yorke 2007). An example of this is the extremely high velocity molecular outflow, signature of massive star formation (Krumholz 2006, and references therein), in the G331 region (Bronfman et al. 2008; Merello et al. 2013).

While extensive work has been carried out to identify and find the physical characteristics and spatial distributions of GMCs in the first Galactic quadrant (IQ) within the solar circle (Dame et al. 1986; Scoville et al. 1987; Solomon et al. 1987), no equivalent catalog of GMCs in the IVQ within the solar circle has been published yet. For the IQ, different methods have been used to define the GMCs: topologically closed surfaces in the three dimensional LBV (longitude, latitude, velocity) CO data phase space (Scoville et al. 1987; Solomon et al. 1987); “*clipping*” the CO data below a certain temperature threshold

(Myers et al. 1986); and subtraction from the observed CO emission of a synthetic dataset generated from an axisymmetric model of the Galactic molecular gas distribution (background subtraction; (Dame et al. 1986)), to “extract” the GMCs from the complex CO *background* emission in which they are immersed. In this work, we use the CO dataset from the Columbia - U. de Chile Southern CO Survey of the Milky Way (Bronfman et al. 1989) (hereinafter referred to as CO Survey) to define GMCs in the 3-dimensional phase space through the subtraction, from the CO data, of an axisymmetric model (ASM; (Bronfman et al. 1988b)) of the complex CO *background* emission following Dame et al. (1986).

We estimate the massive star formation rate and massive star formation efficiency of GMCs in our catalog by taking advantage of a complete CS(2-1) survey toward IRAS point-like sources with FIR colors characteristic of UC HII regions (Bronfman et al. 1996) complemented by a new unpublished CS(2-1) survey (L. Bronfman et al., in preparation). Hereinafter we refer to the whole CS(2-1) dataset as CS(2-1) survey and to the IRAS point-like UC HII regions as IRAS/CS sources. We select massive star forming regions from the IRAS point source catalog, because most of the embedded massive star luminosity is emitted around $100\mu m$ in the Mid- and Far-Infrared (see Figure 2 in Faúndez et al. (2004)). The IRAS point sources are selected by their FIR colors, using the Wood & Churchwell (1989) criterion for UC HII regions, which trace well the population of young embedded massive stars (Faúndez et al. 2004) emitting also in the millimeter continuum. This continuum survey shows that massive cold cores, the very early stages of MSF, are associated to the central UC HII region. The CS(2-1) emission is a great tracer in that it is only excited in regions of densities above $10^4 - 10^5 \text{ cm}^{-3}$. We detected the line emission for about 75% of the candidates. This is a complete sample of the most massive and luminous regions of massive star formation in the Galaxy. There are more recent Galactic surveys

in the Mid-Infrared and Sub-Millimeter regions of the spectrum (GLIMPSE, MIPS GAL, and ATLAS GAL), but (a) there is no complete line surveys to determine their kinematic information and (b) only a small fraction of the luminosity from massive star forming regions comes in the NIR and sub-mm wavelengths (Faúndez et al. 2004; Tanti et al. 2012).

In Section 2 we present for the first time a complete catalog of molecular clouds in the IV quadrant from $l = 300^\circ$ to $l = 348^\circ$, within the solar circle. Distances, masses, and other physical properties of these objects are determined, and their statistical distributions are discussed. In Section 3, the large scale spiral structure traced by GMCs within the Galactic disk is analyzed. In Section 4 we study the massive star formation rate per unit H_2 mass (MSFR) and massive star formation efficiency (ϵ) for GMCs. In Section 5 the main conclusions of the present work are summarized. In Appendix A the effect of subtracting a model from the CO data is described, and in Appendix B, the two-fold distance ambiguity resolution for GMCs in our catalog is explained.

2. GMCs IN THE FOURTH GALACTIC QUADRANT

2.1. GMCs Identification

Giant molecular clouds, within the solar circle, are generally surrounded by and superimposed on an extended *background* of CO emission (Dame 1983) while, outside the solar circle, GMCs appear to be isolated and well defined (May et al. 1997). Therefore, one of the main difficulties we confront in describing GMCs is their definition in phase space (longitude-latitude-velocity). Figure 1 shows a longitude-velocity diagram of the CO emission detected in the Columbia - U. de Chile CO Survey made by integrating the

emission over the latitude range $b = \pm 2^\circ$. Superimposed on the CO data, 284 IRAS/CS sources, used in Section 4 to determine the massive star formation rate and efficiency of GMCs, are plotted as filled circles in a reddish color scale, representing the Far-Infrared flux of the sources. The principal characteristics of the CO survey are summarized in Table 1. The complexity of the emission is evident in the figure. The most accepted interpretation of such a *background* is related to the presence of numerous smaller and more diffuse clouds than GMCs (Dame 1983; Dame et al. 1986; Solomon et al. 1987; Bronfman et al. 1988b) distributed across the inner Galaxy. Since the *background* is seen only in the longitude-velocity diagram, it is also plausible that such smaller and more diffuse clouds are largely confined to spiral arms, along with the GMCs. In addition to this problem, and for Galactic longitudes $l \geq 328^\circ$, the presence of more than one spiral arm feature along the line of sight (Russeil 2003) also contributes to the complex structure of the CO emission.

In order to identify the largest molecular clouds in the longitude-velocity diagram, similar to the analysis done by Dame et al. (1986) for the first Galactic quadrant, a synthetic dataset was generated using the ASM of the CO emission by Bronfman et al. (1988b) (see the insert on the left lower corner of the Figure 2), and subtracted from the observed CO dataset, creating a LBV background subtracted data cube. In this data cube, individual boxes were defined containing the main emission features. As a consistency check, we used the spatial and radial velocity distribution of the IRAS/CS sources to trace the extension of such structures in phase space. The physical information of GMCs was then derived from their spatial maps and spectra. A detailed explanation of the method utilized to define the clouds is presented in Appendix A. After the subtraction of the CO *background* emission, the largest molecular clouds appear as isolated structures, allowing us to assign a (v, b, l) box in phase space to each one of the 92 clouds presented in our catalog. GMCs in the IVQ are presented in Figure 2, a longitude-velocity diagram of the model

subtracted CO emission from the CO Survey in units of antenna temperature.

The observational information of each cloud, contained in its phase space, is utilized in deriving its physical parameters (radius, mass, etc). Integrating the phase space box over its angular extension, the composite spectrum of the cloud $T_A(v) = \sum T_A(v, l, b) \Delta b \Delta l$, with $\Delta b = \Delta l = 0''.125$, is generated and a Gaussian profile fitted to obtain the radial velocity center (V_{lsr}), the velocity width ($\Delta v(FWHM)$), and intensity ($I_{CO} = \int T(v) dv$). In some cases because of the large velocity dispersion of the clouds, larger than the cloud separation, there is a partial blend of the CO profiles along the line of sight between two clouds. In those cases, and in order to properly estimate the CO intensity for each individual cloud, two Gaussian were fitted simultaneously. An example of a two Gaussian profile fit to recover the kinematic information and CO emission of the cloud GMC G333.625–0.125 is shown in Figure 3.

The physical parameters such as position and angular size are derived from the spatial map for each GMC. An example of the spatial map for a GMC in our catalog is presented in Figure 4 corresponding to GMC G331.500–0.125 (number 43 in Table 2). The limits in phase space were identified after the subtraction of the *background* model emission. The bluish color scale represents the CO intensity of the cloud ($I(l, b) = \sum T_A(v, l, b) \Delta v$, with $\Delta v = 1.3 \text{ kms}^{-1}$) and the white square the CO peak intensity. Superimposed on the contours are 10 IRAS/CS sources associated to this cloud, identified as orange filled circles in the figure (the beam size for the CS sources is $50''$ from the SEST Telescope at 100 GHz). The correlation of the point sources with the gas results evident, proving that massive star formation occurs primarily in GMCs. Similar spatial maps for all the clouds in our catalog are available on request.

2.2. Distance Determination

The determinations of heliocentric distances to GMCs is crucial to obtain many of their physical parameters. Currently, a huge effort is being made to obtain distances to massive star forming regions (such as water and methanol masers) in the northern hemisphere via trigonometric parallaxes (Sanna et al. 2013, The BeSSeL Survey), and it is planned to extend this work to southern hemisphere sources (Reid et al. 2009a). Since this is an ongoing work, distances for southern massive star forming regions are not available yet. On the other hand, due to optical extinction in the Galactic disk, kinematic distances are usually the only ones available for objects beyond ~ 3 kpc. Using the radial velocity of the source and a rotation curve (under the assumption of pure circular motion of the gas around the Galactic centre), a kinematic distance to the source can be determined. In the outer Galaxy, given the radial velocity of the source, a unique kinematic distance can be assigned to it. This is not the case for the inner Galaxy where, due to geometric effects, the radial velocity of the source can come from two different places along the same line of sight. This geometric effect is known as the two-fold distance ambiguity of the inner Galaxy. After the determination of the two possible kinematic distances for a source within the solar circle, the distance ambiguity must be removed in order to calculate distance dependent physical parameters. In this simple way, distances can be obtained for GMCs in our catalog.

In order to estimate the kinematic distances to the GMCs in the present work, we adopt the rotation curve derived by Alvarez et al. (1990) from the same dataset analyzed here, assuming an heliocentric distance to the Galactic center of $R_{\odot} = 8.5$ kpc and a circular velocity of the local standard of rest, $\Theta_{\odot} = 220 \text{ kms}^{-1}$:

$$\Theta(R) = 209.2 + 10.5 \frac{R_{\text{GAL}}}{R_{\odot}} \quad [\text{kms}^{-1}]. \quad (1)$$

Effects such as blending along the line of sight and deviations from the common assumption of pure circular motion are among the main sources of uncertainty in kinematic distances. Large scale streaming motions have been observed in a number of regions (Burton 1988; Brand & Blitz 1993). They produce deviations from pure circular motion and may introduce uncertainties of up to 5% in the estimation of galactocentric radii with corresponding uncertainties in the estimated heliocentric distances that may go from 0.6 kpc to 1.7 kpc, if the streaming motion is along the line of sight (Luna et al. 2006). There are also several good examples in the fourth Galactic quadrant of large velocity perturbations caused by the action of energetic events such as, for instance, the large hole in the longitude-velocity diagram at 325° , -40 kms^{-1} attributed by Nyman et al. (1987) to a single event causing multiple supernova explosions and stellar winds.

Based on measurements of trigonometric parallaxes and proper motions of high-mass star forming regions in the Galactic plane, Reid et al. (2009b) investigated deviations from a flat rotation curve by fitting a rotation curve of the form $\Theta(R) = \Theta_{\odot} + (d\Theta/dR)(R - R_{\odot})$, with $\Theta_{\odot} = 254 \text{ kms}^{-1}$ and $R_{\odot} = 8.4 \text{ kpc}$. Two values for the derivative $d\Theta/dR$ are obtained: 1.9 and 2.3. We tested both models and found no significant differences with the kinematic distances derived from the rotation curve in equation 1. For both values of $d\Theta/dR$, kinematic distances for clouds closer than 7.5 kpc (68 GMCs) are systematically underestimated. For $\sim 80\%$ of these clouds, differences are less than 15%, on the order of the estimated errors. For the remaining 20% of these clouds, the largest difference is less than 30%. For clouds with heliocentric distances larger than 7.5 kpc (19 GMCs), the distance estimations are essentially the same (less than 5% difference).

The well known two-fold distance ambiguity is an important source of uncertainty in kinematic distances within the solar circle. In the present work, the ambiguity between far and near distance has been removed by several methods: (a) spatial association with optical objects and the existence of visual counterparts; (b) absorption measurements against HII regions or IRAS/CS sources associated to the cloud for which the distance ambiguity has been solved. Other criteria such as: the latitude criterion (distance off the Galactic plane), the size-to-linewidth relationship also known as the “*first Larson’s Law*” (Larson 1981), and continuity of spiral arms are complementary to the former criteria. The proximity of the CO radial velocity to the terminal velocity ($|v| < 10 \text{ km s}^{-1}$) is used to assign the tangent distance to the cloud. From the 92 GMCs previously defined, we were able to solve the two-fold distance for 87 of them, which are the ones used in the coming sections to analyze the properties of GMCs in our catalog. A detailed analysis of the methods utilized in removing the two-fold distance ambiguity is presented in Appendix B.

After the distance ambiguity was removed for most of the GMCs in our catalog, we have compared our distance ambiguity resolution criteria with that used for the 6.7 GHz methanol (CH_3OH) masers by Green & McClure-Griffiths (2011, and references therein) as a consistency check. In most cases there is a good agreement between the distance assigned to the methanol masers and the distance determined in the present work for their parent GMCs. A detailed discussion of this consistency check can be found in appendix B.

2.3. Physical Properties

The physical parameters characterizing the GMCs identified here are summarized in Table 2. The first column represents the identification number of each GMC, from smaller to larger Galactic longitudes, and from lower to higher Galactic latitudes. The second and third columns represent the Galactic longitude l and Galactic latitude b of the CO peak intensity in the spatial map of each GMC (as described in Figure 4). The fourth column represents V_{lsr} of each cloud, estimated from the Gaussian fit to its composite spectrum. Radial velocities with a * symbol were corrected by $+12.2 \text{ kms}^{-1}$ to take into account the anomaly in terminal radial velocities between $l = 300^\circ - 312^\circ$ found by Alvarez et al. (1990). The fifth column is the linewidth $\Delta v(FWHM)$ of each GMC composite spectrum. Column 6 gives the heliocentric kinematic distance D to each cloud. Column 7 gives the adopted distance (N = near, F = far, and T = tangent) and, as upper indexes, the criteria used in removing the distance ambiguity (see footnotes at the bottom of the table). Column 8 contains the radius for each GMC, defined as $R = R_{ang} \times D$, with R_{ang} the effective angular radius defined as $\pi R_{ang}^2 = A_{ang}$, and A_{ang} the angular area. Since this criterion depends on the intensity threshold in the velocity integrated spatial map, above which the observed position belong to the cloud, Ungerechts et al. (2000) proposed the estimation of the effective physical radius weighting it by the CO intensity of the cloud. We keep our estimation of the effective physical radius mainly to be consistent with the previous northern catalog of Dame et al. (1986). Column 9 gives the Virial mass (M_{virial}) of GMCs in our catalog. Under the assumption of virial equilibrium, we estimate virial masses as follows:

$$M_{virial} = \frac{5\Delta v(FWHM)^2 R}{8 \ln(2)G}, \quad (2)$$

where G is the gravitational constant. The last column contains the molecular mass $M(H_2)$ for each cloud estimated as follows :

$$M(H_2) = m_{H_2} L_{CO} \chi. \quad (3)$$

A mean molecular weight per H_2 molecule corrected for helium abundance of $m_{H_2} = 2.72m_H$ (Allen 1973) is used. The χ factor is the Galactic average $W(CO)$ -to- $N(H_2)$ conversion factor $\chi = 1.56 \pm 0.05 \times 10^{20} [K \text{ kms}^{-1}]^{-1} \text{ cm}^{-2}$ (Hunter et al. 1997) between the integrated CO main beam temperature W_{CO} ($W_{CO} = \int T dv$), and the molecular column density $N(H_2)$. The factor L_{CO} represents the CO luminosity of the cloud estimated as:

$$L_{CO} = \frac{I_{CO} D^2}{\eta}, \quad (4)$$

where $\eta = 0.82$ is the main beam efficiency correction of the antenna temperatures (Bronfman et al. 1989) and I_{CO} in units of $K \text{ kms}^{-1} \text{ sr}^2$ is the integrated CO intensity of the cloud. To obtain I_{CO} for each GMC we perform the integral of $T(v)$ over the Gaussian model fit for each cloud ($I_{CO} = \int T(v) dv$). However, the peak temperature of $T(v)$ depends strongly on the level of the background emission model used to define the clouds (see section 2.1). To remove such uncertainty, before computing I_{CO} , the Gaussian fit is performed again over the original observed dataset, but fixing V_{lsr} and $\Delta v(FWHM)$ to the values obtained previously in the cloud definition process, and leaving the peak temperature as the only free parameter. The value of I_{CO} is then calculated from this new Gaussian fit, and is independent of the level of the background model used to define the clouds. The procedure is further explained in Appendix A.

2.4. Statistical Properties

2.4.1. Size-to-Linewidth Relationship

The theoretical interpretation of the apparently universal size-to-linewidth relationship of molecular clouds has been a matter of debate for many years, and often different theoretical interpretations have been suggested. One of the first attempts was done by Larson (1981). They noticed that the power index ($\sim 1/3$) is similar to the Kolmogorov law of incompressible turbulence and argued that the observed non thermal linewidths originate from a common hierarchy of interstellar turbulent motions and the structures in the clouds can not have formed by simple gravitational collapse. On the other hand, Solomon et al. (1987) argued that the Kolmogorov turbulent spectrum is ruled out by the “new” data with a power index of $\sim 1/2$. They suggest that the size-to-linewidth relation arises from the virial equilibrium of the clouds since their mass determined dynamically agrees with other independent measurements and they are not in pressure equilibrium with warm/hot ISM. Presently, MHD-models have shown that supersonic turbulence is sufficient to explain the observed slope of the size-to-linewidth relation and that self-gravity may be important on large and small scales (Evans 1999; Kritsuk 2007).

The size-to-linewidth relationship $\Delta v(FWHM) = AR^\alpha$ for clouds in Table 2 is presented in Figure 5. A least-squares fit yields:

$$\Delta v(FWHM) = (1.26 \pm 0.35) R^{0.50 \pm 0.07}. \quad (5)$$

The mean value of the full width and half maximum for clouds in our sample is $\Delta v(FWHM) = 9.3 \text{ kms}^{-1}$ which implies a mean velocity dispersion $\sim 4.0 \text{ kms}^{-1}$. The mean physical radius of the clouds in Table 2 is $R = 60 \text{ pc}$. The values $A = 1.26 \pm 0.35$ and

$\alpha = 0.50 \pm 0.07$ are in agreement with the values in Dame et al. (1986) $A = 1.20 \pm 0.22$ and $\alpha = 0.50 \pm 0.05$ (since their estimations for the galactocentric radii do not scale linearly with R_\odot , we have explicitly adopted their radii estimates in Figure 5 and 6). Solomon et al. (1987) found a power law relationship of the form $\sigma_v = 1.0 \pm 0.1 S^{0.5 \pm 0.05}$, where σ_v is the velocity dispersion of the cloud, and S is its physical radius. The difference in the proportionality factor A is due to the different definition of the physical radius of the clouds (geometrical average in their case) and the use of the velocity dispersion instead of the $\Delta v(FWHM)$ for the fit. The slope of the relationship results surprisingly similar to the value obtained in the present work, specially if the different methods employed in defining GMCs are considered. The same occurs in Scoville et al. (1987). They reported a relationship of the form $\sigma_v = 0.5 \pm 0.1 S^{0.55 \pm 0.05}$, close to our values, within the error.

2.4.2. H_2 Density-to-Size Relationship

The H_2 volume density $n(H_2)$ can be expressed as a function of the cloud’s mass and radius:

$$n(H_2) = \frac{M(H_2)}{2m_H 4\pi R^3/3}. \quad (6)$$

The existence of a power law relationship between the $n(H_2)$ and R for molecular clouds ($n(H_2) = BR^{-\beta}$) was first reported by Larson (1981). This relationship is shown in Figure 6 for the clouds in our catalog. A least-squares fit to the physical quantities of GMCs in Table 2 gives:

$$n(H_2) = (8.91 \pm 4.31) \times 10^2 R^{-0.89 \pm 0.12}. \quad (7)$$

The dispersion of the data points is large. This is mainly due to the radius dependence in equation 6 and the corresponding difficulties in defining such a radius. Nonetheless, a trend in Figure 6 is recognizable. The fit results are close to those values obtained by Grabelsky et al. (1987) for GMCs in the Carina spiral arm ($B = 2.67 \pm 1.75 \times 10^2$, $\beta = 0.94 \pm 0.16$), in particular the slope (within error uncertainties). Since most clouds there do not suffer from the distance ambiguity and are very well defined, we believe that the determination of such an observational relationship should be more accurate for clouds in the outer Galaxy. On the other hand, the fit parameters are quite different from the values found by Dame et al. (1986) ($B = 3.6 \pm 1.2 \times 10^3$, $\beta = 1.3 \pm 0.1$), even if GMCs with densities above 100 cm^{-3} in their catalog are excluded and a new fit to their data is made, and there seems to be no easy way to conciliate both estimates. We believe this might be due to the different rotation curve utilized in their work.

2.4.3. *Virial Mass-to-CO Luminosity Relationship and the $W(\text{CO})$ -to- $N(\text{H}_2)$ Conversion Factor*

A relationship between virial mass and CO luminosity of the form $M_{\text{virial}} = CL_{\text{CO}}^\delta$ is presented in Figure 7. A power law fit represented by the dotted line yields:

$$M_{\text{virial}} = (13 \pm 8) L_{\text{CO}}^{0.90 \pm 0.05}. \quad (8)$$

The correlation between virial masses and CO luminosities results evident from the figure. The fit parameters $C = 13 \pm 8$ and $\delta = 0.90 \pm 0.05$ are similar to previous estimates in Solomon et al. (1987), $C = 39 \pm 12$ and $\delta = 0.81 \pm 0.03$, although the slope in our relationship is closer to unity than in their work. The difference in the

proportionality factor C is mainly due to the recovery of CO flux in our catalog. The well behaved correlation puts the CO luminosity as a good tracer of mass in the inner Galaxy.

A linear relationship between the virial mass and the CO luminosity might be used in estimating a $W(\text{CO})$ -to- $N(H_2)$ conversion factor for GMCs close to virial equilibrium. In such case, the slopes found in equations 5 and 7 are expected to follow the relationship $\alpha + \beta/2 = 1$ (Dame et al. 1986; Bertoldi & McKee 1992). For our sample, this relationship yields $\alpha + \beta/2 = 0.95$ supporting the idea that GMCs in our catalog are close to virial equilibrium. If we consider that the virial mass is close to the real mass of the clouds, the χ factor can be evaluated directly from the proportionality between the virial and molecular masses. The solid straight line in Figure 7 represents a least-squares fit procedure yielding $M_{\text{virial}} = (3.7 \pm 0.2) L_{\text{CO}}$. The corresponding $W(\text{CO})$ -to- $N(H_2)$ average conversion factor, if GMCs are in virial equilibrium, is:

$$\chi_{\text{GMCs}} = 1.71 \pm 0.09 \times 10^{20} \text{ [K kms}^{-1}\text{]}^{-1} \text{ cm}^{-2}. \quad (9)$$

This value is consistent within 10% with the χ conversion factor of $1.56 \pm 0.05 \times 10^{20} \text{ [K kms}^{-1}\text{]}^{-1} \text{ cm}^{-2}$ from Hunter et al. (1997) utilized here (see Figure 7).

From a theoretical point of view, Shetty et al. (2011) discussed possible variations in gas simulations of the χ factor for typical conditions in the Milky Way disk. They reported that the χ factor is not expected to be constant within individual molecular clouds, although in most cases it is similar to the Galactic value. From simulations, their best fit model resembling typical conditions of the disk, predicts an average value of $\chi = 2 \times 10^{20} \text{ [K kms}^{-1}\text{]}^{-1} \text{ cm}^{-2}$ which is somewhat larger than our observational estimated value. Glover & Mac Low (2011) showed that “there is a sharp cut-off in CO abundance at

mean visual extinctions $A_v \leq 3$,” where photodissociation becomes important. This is not the case for H_2 which is argued to be controlled principally by the product of density and the metallicity, and insensitive to photodissociation. This could imply a different conversion factor for clouds and inter-cloud medium. Ungerechts et al. (2000) studied GMCs in the Perseus spiral arm traced by the ^{12}CO and ^{13}CO lines. They adopt a factor $\chi = 1.9 \times 10^{20} [\text{K km s}^{-1}]^{-1} \text{ cm}^{-2}$ which is larger than the value of Hunter et al. (1997), and suggest that the “relatively large virial masses or equivalently, the low CO luminosities in relation to the linewidths show that χ could be even higher than the adopted value.”

2.5. Molecular Mass Spectrum and Comparison with the Total Molecular Mass of the Galactic Disk

The molecular mass spectrum of clouds in Table 2 is shown in Figure 8. Following Williams & McKee (1997) we adopted a logarithmic mass bin interval of $\Delta_{\log} = 0.30$ in constructing the mass spectrum of the clouds. Since the shape of the mass spectrum depends strongly on the selected mass bin (Williams & McKee 1997; Rosolowsky 2005), the adopted mass bin interval allows us to make a direct comparison between our results and the results presented in Williams & McKee (1997) in analyzing the catalogs of Solomon et al. (1987); Scoville et al. (1987). The vertical dotted lines in Figure 8 indicates our completeness limit (around $1.3 \times 10^6 M_{\odot}$), where about 75% molecular mass is concentrated toward the high mass end of the spectrum, meaning that we are in fact detecting most of the molecular mass in the catalog. Error bars are estimated as \sqrt{N} , where N is the number of clouds that fall into each mass bin. Triangles represent the central mass of each mass bin. A least-squares fit to the data is performed in the range indicated by the solid line. The dashed line is an extrapolation of the fit to the lower mass end of the distribution. The least-squares fit yields:

$$\frac{dN}{dM} \propto M^{-1.50 \pm 0.40}. \quad (10)$$

The mass distribution of GMCs determines how the molecular mass is distributed among GMCs. For the inner Galaxy, observational evidence has shown a slope of the mass spectrum for GMCs $\gamma < 2$ (Dame 1983; Casoli et al. 1984; Sanders et al. 1985; Solomon et al. 1987; Solomon & Rivolo 1989; May et al. 1997; Williams & McKee 1997; Blitz & Rosolowsky 2004; Rosolowsky 2005; Blitz et al. 2007). The value for the index of the mass distribution of GMCs in the inner Galaxy $\gamma = 1.50 \pm 0.40$ in the present work, $\gamma = 1.81 \pm 0.14$ for the Solomon et al. (1987) GMCs catalog, and of $\gamma = 1.67 \pm 0.25$ for the clouds in Scoville et al. (1987), strongly suggests that most of the molecular mass is concentrated toward the largest molecular clouds in the Galactic disk.

The total molecular mass in form of GMCs in our catalog is $M(H_2) = 1.14 \pm 0.05 \times 10^8 M_\odot$. The most massive cloud in the catalog is GMC G337.750+0.000 with a molecular mass of $M(H_2) = 8.7 \times 10^6 M_\odot$. This last result shows that that molecular mass upper limit $M_{max} = 6 \times 10^6 M_\odot$, established in other GMCs catalogs, may depend on the way GMCs are defined. From stability arguments it is clear that a mass upper limit must exist, but here we find it is higher than the previous value in the literature.

2.5.1. Comparison with Axisymmetric Model Mass

The total molecular mass obtained for all the clouds in our catalog is of $1.14 \pm 0.05 \times 10^8 M_\odot$. The sum of the virial masses for all cloud is very similar, $1.21 \pm 0.03 \times 10^8$

M_{\odot} . Errors are estimated from the standard deviations of the physical parameters from the Gaussian fits. In comparison, the molecular mass derived, for the same region sampled here, from the axisymmetric analysis of Bronfman et al. (1988b) is $3.03 \times 10^8 M_{\odot}$. Therefore, we account for only about 40% of the axisymmetric model mass in our cloud decomposition analysis. Such kind of difference had been detected already for the first Galactic quadrant by Williams & McKee (1997), which estimated about 80% of axisymmetric model mass not accounted for in the catalogs of Solomon et al. (1987) and Scoville et al. (1987).

A possible explanation for this result may arise from the χ conversion factor used here to determine the GMCs mass, which is the same conversion factor, averaged over the whole Galactic plane, used to calculate the axisymmetric model mass. It is possible to postulate different conversion factors for the GMCs and the inter-cloud medium (ICM). For instance, using the same conversion factor, half of the total mass is in GMCs and the other half in the ICM, but using a conversion factor for GMCs twice that for the ICM, one would obtain 2/3 of the mass in GMCs and 1/3 in the ICM. Such a difference between χ_{GMCs} and χ_{ICM} is consistent with results obtained from comparing LTE column densities measured with ^{13}CO with those obtained from CO observations of GMCs and ICM regions (A. Luna et al. 2013, in preparation).

In terms of the distance, the molecular mass in our catalog is distributed as follows: 59% is contained in 64 clouds at the near distance and 39% in 20 clouds at the far distance (the remaining 2% is contained in the 3 clouds for which the tangent distance was assigned) reflecting the fact that the model of the CO *background* emission is less sensitive to the mass at the far distance. The beam dilution causes GMCs at the near distance to be more easily detected than the clouds at the far distance, but this difference is not

too large as shown by the percentage of molecular mass detected at the near and far distance.

3. GMCs AS TRACERS OF THE LARGE SCALE STRUCTURE IN THE FOURTH GALACTIC QUADRANT: SPIRAL ARMS FEATURES

In this section we examine the large scale structure traced by the GMCs in our catalog. In longitude-velocity space, spiral arms features appear as opening loops as a consequence of the rotation of the Galaxy (Bronfman et al. 2000, Figure 5). Since we have already removed the distance ambiguity for the GMCs in our catalog, we attempt to reconstruct the spiral structure of the Southern Galaxy, within the solar circle, by following the position of the clouds in both longitude-velocity space and in the Galactic plane.

3.1. Identification of Spiral Arms Features

The large scale spiral structure can be inferred in the longitude-velocity diagram of the IVQ . Using the model subtracted dataset and location of giant molecular clouds in the longitude-velocity diagram (only clouds with their two-fold distance ambiguity removed), we reconstruct a tentative picture of the spiral structure in the IV quadrant (Figure 9). Clouds with different colors are used for each spiral arm. We distinguish three main large scale features across the Galactic plane: the *Centaurus* spiral arm (near and far sides traced by clouds in red and orange boxes respectively), the *Norma* spiral arm (blue boxes for the near and far side of the arm), and the *3-kpc expanding* arm (black boxes for the near and far side of the arm). We assign the cloud in the yellow box to the near side of the *Carina* spiral arm identified by Grabelsky et al. (1987). The clouds at positive velocities

are tracing the far side of the *Carina* arm (Bronfman 1986; Grabelsky et al. 1988) and, as they are beyond the solar circle, are out of the scope of the present work.

The most prominent spiral feature in Figure 9 is by far the *Centaurus* spiral arm, very clearly traced by 50 GMCs in our catalog, over 40° in its near side (red boxes), and over 15° in its far side (orange boxes). The near side of the arm extends roughly from 305° to 348° , and from -70 kms^{-1} to -30 kms^{-1} , while its far side extends roughly from 35° to 321° , and from -20 kms^{-1} to 0 kms^{-1} . Close to the far side velocity of the *Centaurus* arm is the well known feature, the Coalsack at 303° and 0 kms^{-1} .

The *Norma* spiral arm is shown as blue boxes in Figure 9, extending roughly from 327° to 348° , and from -110 kms^{-1} to -50 kms^{-1} . The detection of the far side of the arm is particularly difficult in these case since, at some spots far emission overlaps with near emission. Such is the case for the GMC G334.125+0.500 (number 48 in Table 2). In the latitude-velocity maps of Bronfman et al. (1989), the near emission appears as wide lanes along Galactic latitude while the far emission has a small angular extension but it is very extended along the velocity axis. The far side of the *Norma* arm also harbors the most massive clouds in our catalog, namely GMC G336.875+0.125 and GMC G337.750+0.000. This statement would change if GMC G342.750+0.000 (number 76 in Table 2) had the wrong distance assignment. We have adopted the near distance to this cloud after the evidence we have collected from the literature but its distance ambiguity resolution is still not as solid as in other cases. If the cloud was indeed at the far distance, it would be associated to the far side of the *3-kpc expanding* and it would have the same molecular mass as the most massive cloud in our catalog: GMC G337.750+0.000, located at the far side of the *Norma* spiral arm. For further discussion on cloud 76 see Appendix B.

The *3-kpc expanding* arm, the closest to the center of the Galaxy, is traced by clouds on its near side, between 335° and 348° , and between -150 kms^{-1} and -100 kms^{-1} , and on its far side, between 345° and 348° , and between -100 kms^{-1} and -60 kms^{-1} . The near side of the *3-kpc expanding* arm has long been recognized in CO and 21 cm longitude-velocity diagrams as a nearly linearly feature in the range $l = 348^\circ$ to 12° , with an expanding motion of -53 kms^{-1} toward $l = 0^\circ$. Recently, Dame & Thaddeus (2008) identified the far side of the arm over the same longitude range as a similar parallel feature displaced $\sim 100 \text{ kms}^{-1}$ to positive velocities. At longitudes further from the Galactic center, the loci of the near and far arms are difficult to trace, and theoretical predictions vary widely (e.g. Cohen & Davies (1976); Romero-Gómez et al. (2011b)). We find 13 clouds at $l < 338^\circ$ with velocities and kinematic distances that suggest they trace the near side of the arm, and 4 more that may trace the far side (GMC 339.125+0.000, GMC 345.1250.250, GMC 346.000+0.000, and GMC 347.250+0.000). Although the velocities of these clouds, -100 kms^{-1} to -60 kms^{-1} , are far below the velocity of the far arm at $l > 348^\circ$ as traced by Dame & Thaddeus (2008), just such a sharp drop in the far arm velocities at lower longitudes is predicted by the recent modeling of Romero-Gómez et al. (2011b). Furthermore, the derived distances of these clouds are consistent with that of the far arm as estimated by Dame & Thaddeus (2008).

In the following, we define limits in Galactic longitude and CO VLSR velocity to produce spatial maps of each one of the arms. In Figure 9, the insert on the left lower corner contains the radial velocity and Galactic longitude limits (orange lines) for each one of the spiral arms over plotted on the CO data of the Columbia Survey. We set such limits following the distribution of the GMCs in the spiral arms. The limits in radial velocity and Galactic longitude of the boxes defined for the clouds belonging to the same spiral

segment are used to establish the extension of the arm in longitude-velocity space. The view in Galactic longitude and latitude of the spiral arms is presented in Figure 10. In the figure, the CO Columbia Survey (without the subtraction of the axisymmetric model of the *background* emission) is used. The color scale of the gas represents the CO intensity ($I(l, b) = \sum T_A(v, l, b) \times \Delta v$) of the arms. The integration limits along the velocity axis were taken from the insert in Figure 9. For the *3-kpc expanding* arm and the *Norma* arm, their near and far sides are plotted on the same map. Overplotted on the figure are the 284 IRAS/CS sources utilized in the present work (section 4) to estimate the massive star formation rate per unit H_2 mass and massive star formation efficiency. The sources are presented as filled circles in a reddish color scale representing the flux of each IRAS/CS source (see Figure 1). The correlation of the CO intensity and the distribution of IRAS/CS sources results evident, being the latter well concentrated toward the plane within $b = \pm 1^\circ$ in all three arms. Since most parts of the arms are traced by GMCs, the role that they play as places of most of the massive star formation in the Galactic disk is evident in the figure.

3.2. Empirical Model of the Spiral Arms in the Southern Galaxy, Within the Solar Circle

A face-on view of molecular clouds in the Galaxy, including our results and previous ones, is presented in Figure 11. In the fourth Galactic quadrant, GMCs in our catalog are plotted as filled circles with the corresponding color to its parent spiral arm (as defined in Figure 9) over the physical area covered in the present work (area filled with gray color), between Galactic longitudes $l = 300^\circ$ and $l = 348^\circ$. The size of the circles is proportional to the molecular mass of GMCs (last column in Table 2). Also plotted are giant molecular clouds (black filled circles) from the catalog of Grabelsky et al. (1987), tracing the *Carina*

spiral arm outside the solar circle. For the first Galactic quadrant, GMCs from the catalog of Dame et al. (1986) are plotted as black filled circles between Galactic longitudes $l = 12^\circ$ and $l = 60^\circ$, tracing the *Sagittarius*, *Scutum*, and *4-kpc* spiral arms, as identified by the author. For the catalogs of Grabelsky et al. (1987) and Dame et al. (1986) their heliocentric distances were corrected by a factor 0.85 to account for the different R_\odot adopted, and molecular masses are those given by the authors, for simplicity. The dotted circle between the Sun and the Galactic Center represents the “tangent distances” in the inner Galaxy, i.e., the distance at the CO terminal velocity. At the position of the Galactic Center, the “*molecular bar*” is represented as a dashed-dotted line. The parameters for the molecular bar were taken from Englmaier & Gerhard (1999) (for consistency with the work of Russeil (2003)), with a radius of 3.5 kpc and an orientation angle of $22^\circ.5$ measured from the Galactic Center and in clockwise direction. Currently, there is a relative broad consensus that our Galaxy is a moderate barred Galaxy, and that the Galactic bar has two main components: a triaxial bulge (also referred as the “thick bar”) inclined in an angle with values found in the literature between 15° and 30° and with a semimajor axis between 3.1 kpc and 3.5 kpc long, and a long “thin bar” inclined $\sim 45^\circ$ (though more recent works suggest angles between 25° and 35°) with a semimajor axis of 4 kpc. The former is mainly traced by old star population while the later is traced by current star formation such as methanol masers (Green et al. 2011; Romero-Gómez et al. 2011a, and references therein). Whether the angular separation between the thick and thin bars is real or just a projection artifact is still a matter of debate (Romero-Gómez et al. 2011a). In terms of star formation activity, an increase in star formation is expected where the thin bar and the *3-kpc expanding* arm meet. Between Galactic longitude 345° and 351° , and radial velocities -30 kms^{-1} and $+10 \text{ kms}^{-1}$ such an increase in star formation activity is observed in the methanol maser distribution of Green et al. (2011). It is interesting to notice that, if one assumes a 45° inclination angle and semimajor axis of 3.4 kpc for the thin long bar,

the three GMCs at the far side of the *3-kpc expanding* arm would match its southern end almost exactly.

We aim to quantify empirically, the parameters describing the principal spiral features presented here. Following Russeil (2003) we fit a logarithmic spiral arm model to the positions of the clouds tracing each of the three spiral features seen in Figure 9 as:

$$R(\phi) = r_o e^{-p\phi}. \quad (11)$$

In the logarithmic spiral arm model, the origin of the reference frame to measure the angle ϕ (in radians) is set to the position of the Galactic center, and ϕ is measured clockwise, with $\phi = 0^\circ$ at Galactic longitude $l = 0^\circ$. The relationship in equation 11 is defined by two parameters: r_o (kpc) meaning the initial radius of the spiral arm, and the pitch angle p , defined as the angle between the tangent to the corresponding galactocentric radius at a certain point in the spiral arm, and the tangent direction to the arm at the same position. It is important to notice that the pitch angle is measured clockwise in the present work yielding, by definition, only positive values, meaning that the $-p\phi$ expression in equation 11 results positive and, by consequence, the galactocentric radius of the arm increases as the angle ϕ moves toward negative values, i.e., into the fourth Galactic quadrant. The model in Equation 11 is not intended to account for possible variations of the pitch angle along the spiral arm (Russeil 2003). In the fitting procedure, we weighted all clouds by the error in galactocentric radius. Other weights such as molecular mass, yield the same results within error uncertainties. In Table 3 we summarized the results of the fit procedures for the spiral arms identified in our sample. The last column in Table 3 accounts for the tangent direction to each spiral arm seen from the Sun, i.e., as measured in Galactic longitude. The

spiral arm models for the clouds in our catalog are plotted as thick color lines in Figure 11. Tangent directions to the model spiral arms are plotted as color straight lines.

In the following, we discuss the face-on view of GMCs in the Galaxy. The most prominent feature, as expected from Figure 9, is the *Centaurus* arm, traced over 10 kpc in the inner Galaxy. The tangent direction to the arm model in Table 3 around 310° is consistent with previous estimates (Alvarez et al. 1990; Bronfman 1992; Englmaier & Gerhard 1999). The arm is quite open and spatially closer to the Carina spiral arm than to the other spiral arm segments in the IV quadrant. The pitch angle of this arm $p = 13^\circ.4$ is consistent with the values obtained by Russeil (2003) ($\sim 11^\circ$) and Dame & Thaddeus (2011) ($\sim 14^\circ$). The far side of the arm is better traced by GMCs than the near side mainly because, at far distances, the CO *background* is much less prominent due to beam dilution effects. The *Norma* spiral arm is the second major spiral feature in our catalog and contains the most massive clouds in our sample. The tangent direction to the model arm $\sim 330^\circ$ is consistent with the values found by Alvarez et al. (1990) and Bronfman (1992) of 328° . The pitch angle of the arm $p = 6^\circ.6$ in Table 3 is consistent with previous estimates (Russeil 2003, and references therein).

We put special attention to the *3-kpc expanding* arm. The far side of the *3-kpc expanding* arm appears well traced by four clouds, but the spiral structure disappears at the near distances. We extended the fit of the logarithmic model for this arm to the position of the Galactic bar. The correlation between the clouds at the far distance and the position of the bar results evident, and is also consistent with the distance determined by Dame & Thaddeus (2008) for the far side of the arm (11.8 kpc). The tangent direction for the arm $\sim 338^\circ$ is also very consistent with the value found by Alvarez et al. (1990) and

Bronfman (1992) of 337° . A dense ridge of masers near $l = 338^\circ$ is identified as the tangent point of the *3-kpc expanding* arm in the work of Green et al. (2011). Using the ATLASGAL 870 μm Survey, Beuther et al. (2012) identified an increase in the sub-millimeter clumps distribution at $l = 338^\circ$ also attributed to the tangent point of the *3-kpc expanding* arm. These results are fully consistent with the tangent direction we find from the logarithmic spiral model of the *3-kpc expanding* arm. The GMCs associated with this spiral arm might be responding to the presence of a Galactic bar, deviating their radial velocities from the assumption of pure circular motion. No previous estimation of the *3-kpc expanding* arm pitch angle $p \sim 5^\circ.6$ in Table 3 is found in the literature. On the observational side, the methanol masers distribution follows an oval structure in the longitude-velocity diagram that could be physically related to an elliptical structure in the face-on disk (Green et al. 2011). Such structure accounts for the parallel lanes of the maser distribution at the far and near distances seen in the longitude-velocity diagram toward the Galactic Center and, to some degree, also accounts for the tangent point at $l = 338^\circ$. Beuther et al. (2012) shows the *3-kpc expanding* arm as a continuous elliptical structure in the Galactic disk following the work of Reid et al. (2009b). On the modeling side, Romero-Gómez et al. (2011a) applied for the first time the “Invariant Manifolds” theory to model spiral arms features in the Galactic disk. Romero-Gómez et al. (2011b) approximately reproduces the observed longitude-velocity CO emission of the near and, to a lesser extent, the far side of the *3-kpc expanding* arm. Their *PMM04-2 bar* model naturally forms a continuous elliptical structure surrounding the composite Galactic bar (thick and thin bars). A continuous elliptical structure of the *3-kpc expanding* arm seems to be also supported by the spatial distribution of GMCs associated to this arm in our catalog.

Concerning the region enclosed between the *Norma* and the *3-kpc expanding* arm in Figure 11, Green et al. (2011) suggest that part of the *Perseus* arm could harbor some

of the methanol masers found toward the tangent direction of the *3-kpc expanding* arm, and in the radial velocity range from -60 kms^{-1} and -85 kms^{-1} . They suggest that these sources could be attributed to the origin of the *Perseus* arm. In our catalog, only the GMC G339.125+0.250 associated to the far side of the *Norma* arm falls within this range. In Figure 11 we do not see any clear indication of the starting point of the arm in the region between the *Norma* and the *3-kpc expanding* arms, place where the starting point of the *Perseus* arm would be found according to the spiral arms models of Russeil (2003). Since we are not sensitive to low mass clouds at the far distance, if only low mass GMCs were tracing the starting point of the *Perseus* arm, we would not be able detect them.

The transformation from longitude-velocity phase space to geometrical space in the inner Galaxy has to be taken cautiously. Perturbations in the velocity field caused by density waves (Burton 1971) and energetic events, like supernovae, as well as by the cloud-cloud velocity dispersion, introduce large uncertainties in the derived kinematic distances (typically between 10% and 20%). Such effects will inevitably wash out much of our description of the spiral structure in the derived distribution of clouds, even if the clouds are confined to a well defined spiral pattern (Combes 1991). This is particularly true for the clouds tracing the *3-kpc expanding* arm, since its expanding velocity, around 53 kms^{-1} introduces large uncertainties in to the position of the arm in phase and geometrical space. Another example of deviations of the pure circular motion is the hole at 329° , -60 kms^{-1} in the longitude-velocity diagram surrounded by molecular clouds with velocity differences of up to 30 kms^{-1} along the line of sight that, according to formaldehyde (H_2CO) absorption measurements, are probably at the near side of the *Centaurus* arm. Usually, large variations in model parameters such as pitch angle, initial radius, and tangent direction are found depending on the tracer (21 cm emission, HII regions, stellar population, etc.) used to identify the large scale structure in the Galactic disk (Englmaier & Gerhard 1999; Russeil

2003).

Despite all difficulties involved in transforming CO radial velocities into heliocentric distances, the spiral structure in the southern Milky Way stands out clearly when traced by giant molecular clouds. In the present work, and with a simple logarithmic spiral arm model we reproduce some characteristics found by other authors, such as the tangent directions to the spiral arms in the southern Galaxy. More sophisticated models are necessary to account for the details of the parameters in each spiral arm. The purpose here is to test the consistency with previous work of the large scale spiral structure traced by GMCs in the fourth Galactic quadrant.

4. MASSIVE STAR FORMATION RATE PER UNIT H₂ MASS AND THE STAR FORMATION EFFICIENCY DERIVED FOR GMCs

There is close relationship between GMCs and massive stars in our study. While our CO Survey is the best available tracer of GMCs, the CS(2-1) survey is the best tracer of UC HII regions. We find a close relationship between GMCs and massive stars in our study. Since most of the UV photons emitted by massive stars are absorbed and re-emitted by the surrounding dust in the Far-Infrared part of the electromagnetic spectrum (Kennicutt 1998), the Far-Infrared (FIR) emission of UC HII regions is a good tracer of the massive star formation (Luna et al. 2006). On the other hand, the CS(2-1) emission requires high molecular gas densities, $10^4 - 10^5 \text{ cm}^{-3}$, to become excited, resulting also in a good tracer of massive star formation regions. In order to estimate the massive star formation rate per unit H₂ mass (MSFR) and the star formation efficiency ϵ of giant molecular clouds in our catalog, we use the catalog of IRAS point-like sources.

The FIR flux of the UC HII regions is obtained directly from the four bands ($12\mu m$, $25\mu m$, $60\mu m$, and $100\mu m$) of the IRAS point-like sources catalog. Since the IRAS catalog does not provide velocity information of the sources necessary to locate them along the radial velocity axis, we use the CS(2-1) line. We obtain the kinematic information of the UC HII regions from the CS(2-1) survey of Bronfman et al. (1996) of IRAS point-like sources with FIR colors characteristic of UC HII regions in the whole Galaxy complemented by a new survey to be published elsewhere. The new data amounts to 19% of the detections .

There is a clear correlation between the molecular gas and the IRAS/CS sources, in particular, toward the position of spiral arms traced by GMCs. The IRAS/CS sources utilized in the present work are plotted over the CO emission in the longitude-velocity diagram from the Columbia Survey in Figure 1. The reddish color scale represents the FIR fluxes of the UC HII regions. IRAS/CS sources with positive velocities were excluded from the present work since they are located outside the solar circle. From Figure 1 the correlation between the gas and the position of the IRAS/CS sources results evident and, in particular, their concentration to the position of the spiral features, such as the prominent *Centaurus* arm (near side from 305° to 348° , and from -70 kms^{-1} to -30 kms^{-1} , and far side from 35° to 321° , and from -20 kms^{-1} to 0 kms^{-1}). The 284 IRAS/CS sources are plotted in different velocity ranges, corresponding to spiral arms in the Southern Galaxy, in Figure 10. We see that most of the sites of massive star formation are well concentrated within $\pm 1^\circ$ of the Galactic plane and are well correlated with giant molecular clouds tracing the spiral arms. The *3-kpc expanding* arm contains around 4% of the UC HII regions in the present work. Concerning the *Norma* arm, two prominent regions of massive star formation appear at 331.5° and between 336° and 338° . This spiral arm contains around 14% of the IRAS/CS sources. Since the near side of the *Centaurus* arm is the largest spiral segment in the longitude-velocity diagram, it contains most of the UC HII regions in our sample (57% of the

IRAS/CS sources). Important regions of massive star formation in this spiral arm appear between 310° and 313° , at 331° , and between 332° and 334° . The *far* side of the *Centaurus* arm contains around 4% of the IRAS/CS sources. Although these sources have small FIR fluxes, they are very luminous since they are located at the far distance of the spiral arm.

The first step in estimating the massive star formation rate (MSFR) of the clouds in our catalog is related to the association of each IRAS/CS source to its parent GMC. The association between UC HII regions and GMCs is established using the following criteria: (a) the Galactic coordinates (b, l) of the IRAS/CS source fall inside the spatial range defined for each GMC, and (b) the CS radial velocity of the IRAS/CS source falls within the $3 \times \sigma_v$ velocity range, where σ_v is the velocity dispersion of the parent GMC. We associated 214 sources ($\sim 75\%$ of the total 284 IRAS/CS sources within the covered area in this work) with their parent GMCs. The remainder 49 IRAS/CS sources are either associated with less bright GMCs not considered in our catalog, or have peculiar velocities for their parental GMCs. Since these sources represent only $\sim 20\%$ of the total number of IRAS/CS sources, we consider the remaining 75% as a fair representation of the massive star formation within giant molecular clouds in our catalog. An example of associated IRAS/CS sources to their parent GMC is found in Figure 4.

The FIR luminosity (L_{FIR}) of embedded stars in giant molecular clouds is summarized in Table 4. The first column represents the GMCs identification (*clouds*). The second column shows the number of UC HII associated to the cloud. The third column contains the total Far-Infrared flux F_{IRAS} of the massive star forming regions associated to each giant molecular cloud. The FIR flux of each UC HII region was derived directly from the fluxes reported in the four bands of the IRAS point-like catalog (version 1) as follows:

$$F_{IRAS} = 4\pi \sum_{\nu} \nu F_{\nu}. \quad (12)$$

The fourth column contains the Far-Infrared luminosity L_{FIR} derived for each GMC as $L_{FIR} = F_{IRAS}D^2$ where F_{IRAS} is the total Far-Infrared flux for each cloud and D is its distance. The fifth column contains the massive star formation efficiency ϵ of GMCs described in section 4.2. In our sample, the total molecular mass of the GMCs which harbor at least one massive star formation region is $\sim 9.7 \times 10^7 M_{\odot}$, which accounts for 85% of the total molecular mass in form of GMC and from the 60 GMCs in Table 4 with at least one UC HII region associated, 36 of them have molecular masses larger than $10^6 M_{\odot}$. In general, the most massive clouds exhibit most of the massive star formation in the Galactic disk. The total FIR luminosity in Table 4 emitted by the UC HII regions associated with giant molecular clouds is $3.66 \times 10^7 L_{\odot}$. From Table 4, the *Norma* spiral arm concentrates most of the massive star formation in the Southern Galaxy. The eleven giant molecular clouds in this arm account for a total FIR luminosity of $1.85 \times 10^7 L_{\odot}$, equivalent to the 50% of the total FIR luminosity contained in GMCs. The GMC G337.750+0.000 (number 54 in Table 2) belonging to the far side of this arm is the most prominent massive star forming region in the inner fourth Galactic quadrant, with a FIR luminosity of $6.45 \times 10^6 L_{\odot}$, around 35% of the total FIR luminosity in the *Norma* spiral arm.

4.1. Massive Star Formation Rate Per Unit H₂ Mass

We calculate the massive star formation rate per unit H₂ mass defined as MSFR = L_{FIR}/M for GMCs in our catalog, following Bronfman et al. (2000). In Figure 12, the observational relationship between the FIR luminosity in Table 4 and molecular masses for

GMCs in Table 2 is shown. For the plot, we used only FIR luminosities of GMCs from Table 4 that have more than one UC HII region associated to reduce the statistical error of the relationship. The colors of the filled circles are related to the spiral arms in Figure 9.

The two red crosses in the plot are the GMC G309.125–0.375 and GMC G313.875–0.125 belonging to the *Centaurus* spiral arm were left out of the fit in Figure 12 due to their deviation from the general trend. For GMC G309.125–0.375 there are neither other IRAS/CS sources in (l,b,v) space close to the clouds nor non-detections in the CS data, so the low FIR luminosity seems to be real and not an artifact of the criteria used in associating UC HII regions to GMCs. For GMC G313.875–0.125, there are two IRAS/CS sources close to the cloud in (l,b,v) space, but do not fulfill the association criteria. The total IRAS FIR flux of the sources is $3293 L_{\odot} \text{ kpc}^{-2}$, which would increase L_{FIR} by a factor 1.8. Nonetheless, this increase would not conciliate the position of the cloud within the general trend in Figure 9. Besides, no non-detections in the CS data are present. A possible reason for the deviation of the clouds from the trend in Figure 9 could be related to some “missing” UC HII regions during the process of selecting them by FIR colors in the IRAS catalog.

The massive star formation rate is obtained from a least-squares fit to the proportionality relationship between the FIR luminosity and molecular mass of GMCs which yields $L_{FIR} = 0.41 \pm 0.07 M(H_2)$. Additionally, a least-squares fit to the four most massive ($M(H_2) > 3 \times 10^6 M_{\odot}$) and most active ($L_{FIR} > 2 \times 10^6 L_{\odot}$) star forming GMCs of the sample, GMC G328.250+0.375, GMC G331.500–0.125, GMC G336.875+0.125, and GMC G337.750+0.000 belonging to the *Norma* spiral arm (blue filled circles in the region enclosed by the dotted lines) was performed yielding $L_{FIR} = 0.58 \pm 0.09 M(H_2)$.

The clouds belonging to the far side of the *Norma* arm are, within our catalog, the most massive and with the highest massive star formation rate in the Southern Galaxy. Bronfman et al. (2000) showed that the mean massive star formation rate per unit H_2 mass is higher in the Southern Galaxy than in the Northern Galaxy, being around $\sim 0.21 L_\odot/M_\odot$ for $0.2 \leq R/R_\odot \leq 1$; around $\sim 0.28 L_\odot/M_\odot$ for $0.4 \leq R/R_\odot \leq 0.8$; and with a peak around $\sim 0.41 L_\odot/M_\odot$ for $0.5 \leq R/R_\odot \leq 0.6$ (without correction for helium abundance). They suggested that such an enhancement of massive star formation appears to be dominated by the presence of the *Norma* spiral arm, where a large fraction of the most FIR luminous sources are found.

In order to compare our results with those in Bronfman et al. (2000), we first divide their estimates by $m(H_2)^*/m(H_2) = 2.72m(H)/2m(H) = 1.36$, where $m(H_2)^*$ is the H_2 molecular mass corrected for helium abundance utilized in this work. The clouds in Table 4 are located between $0.37 \leq R/R_\odot \leq 0.94$. Their MSFR is about a factor two higher than one derived by Bronfman et al. (2000) for almost the same region of the Galactic disk ($\sim 0.21 L_\odot/M_\odot$ for $0.4 \leq R/R_\odot \leq 0.8$). The four most massive GMCs in the sample are located between $0.55 \leq R/R_\odot \leq 0.60$ in Galactocentric radius and coincide with the position of the MSFR peak found by Bronfman et al. (2000). Their MSFR is also about a factor of two higher than the one found by Bronfman et al. (2000) at the peak of the distribution of embedded stars $\sim 0.30 L_\odot/M_\odot$ between Galactocentric radii $0.5 \leq R/R_\odot \leq 0.6$. This shows that most massive star formation activity in the southern Galaxy not only occurs in the *Norma* spiral arm, but in its most massive clouds. It is interesting to notice that, the factor two difference between the MSFRs in GMCs found here and by Bronfman et al. (2000) for the average and peak values, is the same difference we have between the molecular mass in form of GMCs here and the axisymmetric model molecular mass estimated by Bronfman et al. (1988b). According to this evidence, it appears reasonable to use the

massive star formation rate per unit H_2 mass of the most massive clouds in the *Norma* spiral arm as a standard scale to compare the massive star formation activity in the rest of the Galaxy.

The massive star formation rates estimated here and in Bronfman et al. (2000) are a strict lower limit because only UC HII regions are contributing to it. Since the diffuse FIR emission from dust contained in the clouds is not considered in the IRAS point-like source catalog, and some embedded OB star are probably illuminating dust regions with large angular sizes, escaping from the identification as ultra-compact sources, the total FIR flux derived for a particular cloud is a lower limit to the real value, giving a lower limit for the MSFR.

4.2. Massive Star Formation Efficiency ϵ

The values for the massive star formation efficiency of the GMCs in our catalog are given in the last column of Table 4. To derive the massive star formation efficiency ϵ we first transform the FIR luminosity of the clouds into the corresponding massive star formation rate \dot{M} in units of $\text{M}_\odot\text{yr}^{-1}$. Following Luna et al. (2006) we convert the FIR-Infrared luminosity of the clouds as follows:

$$\dot{M} = 6.5 \times 10^{-10} \left(\frac{L_{\text{FIR}}}{L_\odot} \right) \text{M}_\odot\text{yr}^{-1}. \quad (13)$$

Using the \dot{M} computed in equation 13, the massive star formation efficiency for GMCs in our catalog can be determined as:

$$\epsilon = \tau_{OB} \frac{\dot{M}}{M_{GMC}}, \quad (14)$$

where $\tau_{OB} = 10^8$ yr, is assumed to be a typical lifetime for an OB star region (Luna et al. 2006, and references therein). The estimated massive star formation efficiencies shown in Table 4 are derived for the molecular mass of clouds in our catalog. All efficiencies derived here are of a few percents of the available molecular mass of the clouds, and the average value is 3%. This is consistent with the values found in the literature (Mac Low & Klessen 2004; Luna et al. 2006; Zinnecker & Yorke 2007; McKee & Ostriker 2007). Our estimates reinforce the common idea that GMCs are inefficient in forming massive stars, implying that processes other than simple gravitational collapse must control the MSFR in the clouds.

5. SUMMARY

Using the Columbia - U. de Chile CO Survey of the Southern Milky Way we present the first catalog of GMCs in the fourth Galactic quadrant, within the solar circle. Their average size, linewidth, and mass are estimated and their statistical properties are determined.

GMCs Identification and Physical Properties

We identify 92 molecular complexes in the inner Southern Galaxy and remove the two-fold distance ambiguity for 87 of them. The total molecular mass of GMCs is $M(H_2) = 1.14 \pm 0.05 \times 10^8 M_\odot$. The evidence in our catalog from the observational size-to-linewidth ($\Delta v(FWHM) \propto R^\alpha$) and size-to- H_2 volume density ($n(H_2) \propto R^{-\beta}$) relationships suggests that GMCs are close to virial equilibrium ($\alpha + \beta/2 = 0.95$). The

mass spectrum of the clouds (slope $\gamma = 1.50 \pm 0.40$) shows that most of the molecular mass is concentrated to the high mass end of the distribution. From the total molecular mass in our sample, 60% is located at the near distance while the remaining 40% is at the far distance. The completeness limit of the molecular mass spectrum is at 75% of the total mass.

Total GMCs Mass and Axisymmetric Model

The total molecular mass of GMCs in our catalog accounts for 40% of the molecular mass derived from the axisymmetric analysis of the H_2 volume density in the fourth Galactic quadrant, while in previous studies it was only 20%. From the virial analysis, we estimate an average $W(\text{CO})$ -to- $N(H_2)$ conversion factor GMCs $\chi_{GMCs} = 1.71 \pm 0.09 \times 10^{20} [\text{K km s}^{-1}]^{-1} \text{ cm}^{-2}$ which is consistent with the Galactic average value $\chi = 1.56 \pm 0.05 \times 10^{20} [\text{K km s}^{-1}]^{-1} \text{ cm}^{-2}$ (Hunter et al. 1997). The average Galactic value of the conversion factor in Hunter et al. (1997) is estimated for both, cloud and inter-cloud medium simultaneously. A higher conversion factor for GMCs and a lower conversion factor for the inter-cloud medium could also reproduce the estimated average Galactic value and increase the molecular mass of GMCs reducing the difference even further.

Large Scale Spiral Structure

We trace here three large scale spiral arms within the solar circle: the *Centaurus*, *Norma*, and *3-kpc expanding* arms. The *Carina* arm is not traced because of its wide latitude. After fitting a logarithmic spiral arm model for each of the arms, tangent directions are found to be at roughly 310° , 330° , and 338° respectively. These values are consistent with previous determinations of the tangent directions done by Alvarez et al. (1990) and Bronfman (1992). The *Centaurus* arm is the most prominent feature in the southern Galaxy. Its pitch angle $p = 13^\circ.4$ is large compare to the pitch angles of the *Norma* ($p = 6^\circ.6$) and *3-kpc* ($p =$

5°.6) arms. The spatial maps of the arms show that the molecular gas contained in GMCs and UC HII regions (IRAS/CS sources) are tightly correlated, being the *Norma* spiral arm the feature with the most massive clouds in our sample. The positions of the far clouds in the *3-kpc expanding* arm converge to the location of the far side of the arm traced in Dame & Thaddeus (2008) down to $l = 348^\circ$.

Massive Star Formation Rate for GMCs

Massive stars form in GMCs. Making use of the CS(2-1) survey (Bronfman et al. 1996) toward IRAS point-like sources with FIR colors characteristic of UC HII regions (Wood & Churchwell 1989) and a new unpublished CS(2-1) survey, we analyzed massive star formation GMCs. The total molecular mass of GMCs with massive star formation activity accounts for 85% of the total molecular mass in our sample, and 60% of them have masses larger than $6 \times 10^6 M_\odot$. From the spiral features identified in our catalog, the *Norma* spiral arm is the most active in forming massive stars. The GMCs in this arm have a total FIR luminosity of $1.85 \times 10^7 L_\odot$, equivalent to 50% of the total FIR luminosity in our sample. The GMC G337.750+0.000 is the most prominent massive star forming region in the inner southern Galaxy, with a FIR luminosity of $6.45 \times 10^6 L_\odot$, equivalent to 35% of the total FIR luminosity in the arm. The observational evidence is consistent with the idea that, in general, the most massive clouds exhibit most of the massive star formation in the Galactic disk.

The massive star formation rate per unit H_2 mass (MSFR) and the massive star formation efficiency ϵ are estimated for GMCs in our catalog. From the molecular mass of GMCs in our sample, the massive star formation rate is $MSFR = 0.41 \pm 0.06 L_\odot/M_\odot$. A separate estimation for the most massive and most active massive star forming GMCs in our sample, GMC G328.250+0.375, GMC G331.500–0.125, GMC G336.875+0.125, and

GMC G337.750+0.000 belonging to the *Norma* spiral arm, yields $\text{MSFR} = 0.58 \pm 0.09$ L_{\odot}/M_{\odot} .

The MSFR in GMCs is about a factor two higher than the values derived for the Galactic plane ~ 0.21 L_{\odot}/M_{\odot} between $0.4 \leq R/R_{\odot} \leq 0.8$ and peak value ~ 0.31 L_{\odot}/M_{\odot} for $0.5 \leq R/R_{\odot} \leq 0.6$ (where part of the *Norma* arm is located) derived by Bronfman et al. (2000) after a correction for Helium abundance is applied to their results. The discrepancy could be explained in terms of the molecular mass difference between GMCs in the present catalog and the molecular mass derived from the axisymmetric model analysis done by Bronfman et al. (1988b). We derive an average massive star formation efficiency ϵ for GMCs of $\sim 3\%$ percent of their available molecular mass.

We gratefully acknowledge Prof. Patrick Thaddeus for his seminal contributions to this work. We thank Hector Alvarez and Abraham Luna for their early help with the analysis. We remember Prof. Jorge May (R.I.P.) for his unconditional dedication to this project. P.G. and L.B acknowledge support from Basal Center For Astrophysics And Associated Technologies PFB-06.

A. AXISYMMETRIC MODEL SUBTRACTION

A.1. The Axisymmetric Model

In order to isolate the largest molecular clouds in the fourth Galactic quadrant from the CO *background* emission in which they are immersed, similar to the work of Dame et al. (1986), an axisymmetric model of CO *background* emission was generated and subtracted

to the full 3-dimensional (v, b, l) observed CO dataset. We assumed that the *background* emission follows the same radial distribution of the molecular mass in the fourth Galactic quadrant determined by Bronfman et al. (1988b). Following Dame et al. (1986) the *background* level was adjusted so that 65% of the non local ($|v| < 20 \text{ kms}^{-1}$) emission was removed from the survey.

On large scales, the effect of subtracting the axisymmetric model from the CO dataset can be observed in Figure 13. The figure shows standard longitude-velocity diagrams at Galactic latitude $b = 0^\circ$ of CO and ^{13}CO emission. The different panels represent: (a) CO(1-0) emission from the Columbia CO Survey, (b) CO(1-0) emission of the Columbia CO Survey with the axisymmetric model subtracted, and (c) ^{13}CO (1-0) emission from Bronfman et al. (1988a). The insert on the left lower corner in panel (a) represents the axisymmetric model subtracted from the CO data to produce the longitude-velocity diagram in panel (b). The emission of the rare ^{13}CO isotope is less saturated than the CO line, being a better molecular mass tracer at high densities ($\sim 10^3 \text{ cm}^{-3}$), and its narrow line facilitates separation of individual clouds along the velocity axis (Dickman 1978; Frerking et al. 1982; Liszt et al. 1984; Liszt 1995). From Figure 13 results evident that the subtraction of the *background* model from the CO dataset dramatically improves the similarity between the ^{13}CO and ^{12}CO longitude-velocity diagrams, suggesting that such a subtraction effectively distinguish the clouds from the CO *background* in which they are immersed.

The large scale features are preserved after the model subtraction. The total CO intensity with no correction for the main beam efficiency ($I = \sum T_A(v, l, b) \Delta v \Delta b \Delta l$, with $\Delta v = 1.3 \text{ kms}^{-1}$, and $\Delta b = \Delta l = 0^\circ.125$) is $6.9 \times 10^3 \text{ K kms}^{-1} \text{ degree}^2$ and $2.4 \times 10^3 \text{ K kms}^{-1} \text{ degree}^2$ for the observed and subtracted model datasets, respectively, indicating that

65% of the total emission was removed. The subtraction of the model from the observed CO dataset does not modify the overall shape of the intensity distribution, preserving the large scale features of the emission. In Figure 14 the CO intensity distribution as a function of Galactic longitude ($I(l) = \sum T_A(v, l, b) \Delta v \Delta b$) is presented for the model subtracted (CO MSD) and the observed (CO Survey) datasets. The tangent directions to spiral arms at 309° , 328° , and 337° (Bronfman 1992) are present in both datasets.

A.2. Impact of the Model Subtraction on Individual Clouds

We investigate variations in the molecular mass $M(H_2)$ due to changes in the peak antenna temperature T_{peak} from the recovery of the CO flux lost during the subtraction of the *background* axisymmetric model from the observed dataset. In the following, we refer to the values calculated in the model subtracted dataset as “MSD” and the values determined for the clouds in our catalog as “GMCs.” The values of T_{peak} and $M(H_2)$ for both datasets are presented in Table 5. The relationship for each quantity between both datasets is shown in Figure 15. A least-squares fit between $T_{peak}(MSD)$ versus $T_{peak}(GMCs)$, and $M(H_2)(MSD)$ versus $M(H_2)(GMCs)$ yields:

$$\Delta v(FWHM)_{GMCs} = \Delta v(FWHM)_{MSD} \text{ (by construction),} \quad (A1)$$

$$T_{peak_{GMCs}} = (2.14 \pm 0.10) T_{peak_{MSD}}^{0.98 \pm 0.04}, \quad (A2)$$

$$M(H_2)_{GMCs} = (2.14 \pm 0.10) M(H_2)_{MSD}. \quad (A3)$$

From Figure 15 we see that T_{peak} changes linearly from the model subtracted dataset to the GMCs catalog. The differences between the subtracted model dataset and the values of the GMCs in our catalog are only due to the CO flux recovery. After we have accounted for the loss of CO flux (see section 2.3), the (average) T_{peak} value increase by a factor 2.14 as shown in equation A2, and this is directly mirrored in the increase of molecular mass shown in equation A3.

B. NOTES ON INDIVIDUAL GMCs.

In this appendix we review the resolution for the two-fold distance ambiguity for giant molecular clouds in our sample. After making an exhaustive search in the literature we use nine criteria to distinguish between near and far distances. In most cases, more than one criterion is used to remove the distance ambiguity and when all methods converge to the same solution, we assign the near or far distance to the cloud. The criteria are the following:

- (a) Spatial Association with optical objects of the RCW catalog (Rodgers et al. 1960) and visual counterparts for HII regions (Caswell & Haynes 1987): usually and because of the high extinction in optical wavelengths, optical emission is detectable only for objects closer than 6 kpc within the Galactic plane locating any cloud, with an optical counterpart, almost certainly at the near distance.
- (b) IRAS/CS sources with already removed distance ambiguity associated to a GMC: in this case, the distance ambiguity resolution of the IRAS/CS source is assigned to the cloud, but the kinematic distance derived from the rotation curve is used in estimating

all the physical quantities of the parent GMC.

- (c) Presence (or absence) of absorption features of species such as formaldehyde (H_2CO) or the hydroxyl radical (OH) against the $\text{H}\alpha$ continuum emission of HII regions (Caswell & Haynes 1987), or HI absorption features in molecular clouds of the cold (10 - 30 K) atomic hydrogen against the warm (100 - 10^4 K) 21 cm continuum emission across the Galactic plane (Roman-Duval et al. 2009). In the first method, depending on the radial velocity of the recombination and absorption features, and on the CO radial velocity V_{lsr} of the cloud, it is possible to distinguish between far or near distance to the cloud in several cases. For instance, if the absorption feature occurs at a radial velocity close to V_{lsr} (within $2 \times \sigma_v$) and it is smaller (less negative) than the radial velocity of the recombination line, the absorption can be interpreted as the cloud being in front of the HII region absorbing the continuum emission most probably at the near distance. On the other hand, if the LSR velocity of the absorption feature does not coincide with the LSR velocity of the cloud, this suggests the far distance as the most probable distance to the cloud. Because of the large linewidths of the HI recombination line ($\Delta v(FWHM) \sim 20 - 30 \text{ km s}^{-1}$), the absorption features fall sometimes inside the recombination linewidth, making it hard to distinguish whether the emission originates in a different location in the Galactic disk than that of the recombination line. In those cases, the distance resolution solved by this technique should be taken with caution. The second method consist of comparing the HI self-absorption of the cold gas against the background of HI warm continuum emission in the Galactic plane with the $^{13}\text{CO}(1-0)$ emission at the same LSR velocity (Busfield et al. 2006; Roman-Duval et al. 2009). If HI self-absorption is identified to be at the same radial velocity of the $^{13}\text{CO}(1-0)$ velocity for a particular source, the source lies almost certainly at the near distance, since being at the far distance, the absorption feature would be “filled up”

with the background of HI continuum emission along the line of sight.

- (d) Observational size-to-linewidth relationship (*first Larson's Law*): the existence of an observational size-to-linewidth relationship for GMCs (Solomon et al. 1987; Scoville et al. 1987; Dame et al. 1986) can be used in some cases to distinguish between the near and far distances. Since the physical radius of a cloud is proportional to the distance, locating a cloud at the wrong position might yield an unrealistically large (more than 200 pc) or small (less than 10 pc) physical radius for the GMC. Concerning the velocity structure of the clouds, very massive GMCs at the far distance present an elongated structure along the radial velocity axis and a very reduced angular extension. An example of this can be found in the latitude-velocity maps in Bronfman et al. (1989) at $337^{\circ}.250$, between $v = -90 \text{ km s}^{-1}$ and $v = -30 \text{ km s}^{-1}$. If a cloud is located at a given distance (near or far), the physical radius of the cloud should be consistent with the overall trend in the observational size-to-linewidth relationship.

- (e) Distance off the Galactic plane following the molecular gas distribution of Bronfman et al. (1988b): the position of a certain cloud relative to the Galactic plane in azimuth direction can be used in some cases to distinguish between near and far distances. We examined the perpendicular projection of the distance to the clouds respect to the plane, and compared it with the distribution of the molecular gas in Bronfman et al. (1988b). The near distance is assigned to clouds which, being located at the far distance, strongly deviate ($\sim 3\sigma_z$) from the molecular gas distribution of the Galactic plane in the azimuth direction.

- (f) Continuity of the near or far side of spiral arms: in a few cases, well defined segments of

spiral arms might also indicate the location of a particular cloud in the Galactic plane. Since spiral arms are seen as lanes of emission in the longitude-velocity diagram, and the near and far sides of the arms are usually separated by a few tens kms^{-1} , clouds located at the far and near distances of the same arm are expected to be separated in LSR velocity well enough to be distinguish from each other.

- (g) CO radial velocity of a cloud lies close ($|v| < 10 \text{ kms}^{-1}$) to the tangential LSR velocity: since the difference between near and far distances decreases toward the tangent point to the line of sight, clouds that are close enough to the tangent LSR velocity at a given Galactic longitude l (Alvarez et al. 1990) are located at the tangent distance, i.e., at the distance where the galactocentric radius is minimum ($R_{gal} = R_{\odot} \sin l$).

We explore the consistency of these criteria by comparing our distance determination results with those obtained for 6.7 GHz methanol (CH_3OH) masers in the work of Green & McClure-Griffiths (2011) using the HI self-absorption method. We associated the methanol masers to their parent GMCs following the criteria explained for the association of the IRAS/CS sources to GMCs. We only considered methanol masers with the most solid distance ambiguity resolution (labeled with “a” in column 5 of Table 2 in their work) that fall within the solar circle, and within the range covered by the present work: $l = 300^\circ$ - 348° and $b = \pm 2^\circ$.

We found 20 GMCs with at least one methanol maser associated in our catalog. These GMCs in Table 2 are: clouds 18, 28, 45, 49, 51, 63, 72, and 78, for which the maser information is fully consistent with the distance assigned to the corresponding GMC; clouds 9, 34, 35, 38, and 76, for which the methanol maser information is contradictory with our distance

estimate but that can be explained in terms of the sensitivity of our work to clouds less massive at the far distance; clouds 57, 64, and 73, associated with the near side of the *3-kpc expanding* arm for which the masers information puts them at the far distance; and clouds 14, 21, 33, and 54, for which there is an unexplained discrepancy between the methanol maser distance determination and our distance estimates. We include a detail discussion of the methanol maser information for each GMC in the following notes on individual clouds.

- 1: The IRAS/CS sources G300.969+1.152 and G301.116+0.966 associated to this cloud have as visual counterparts the objects RCW65 (G301.0+1.2) and RCW66 (G301.1+0.9) (Whiteoak & Gardner 1974; Shaver & Goss 1970; Caswell & Haynes 1987) locating the cloud at the near distance. The radial velocity of this cloud ($V_{lsr} = -39.1 \text{ kms}^{-1}$) was corrected by $+12.2 \text{ kms}^{-1}$ in order to take into account the anomalous terminal CO velocities between $l = 300^\circ - 312^\circ$ in the fourth Galactic quadrant as described in Alvarez et al. (1990).
- 2: The IRAS/CS sources G305.085+0.062, and G305.194+0.036 are associated with the optical object RWC74 (G305.1+0.15) (Shaver & Goss 1970; Caswell & Haynes 1987; Caswell & Robinson 1974; Lockman 1979; Wilson et al. 1970) locating the cloud at the near distance. We did not correct the radial velocity of the cloud ($V_{lsr} = -36.4 \text{ kms}^{-1}$) by the anomalous $+12.2 \text{ kms}^{-1}$ radial velocity since it lies far ($> 15 \text{ kms}^{-1}$) from the terminal velocity $v_{term} = -55 \text{ kms}^{-1}$ (Alvarez et al. 1990) at this Galactic longitude ($l = 305^\circ.250$).
- 3: At the position of the cloud, no observations of absorption or recombination line emission were found in the literature. Locating the cloud at the near distance (1.9

kpc) yields a very small physical radius (~ 10 pc). In this case, the absence of an optical counterpart at such close distance is unlikely. Placing the cloud at the far distance yields a more consistent physical radius (~ 42 pc) with the size-to-linewidth relationship. We adopt the far distance to the cloud.

- 4: The HII region G305.678+1.607 has a visual optical counterpart (Caswell & Haynes 1987). The high latitude of the cloud ($b = +1^\circ.250$) also suggests the near distance. The CO radial velocity ($V_{lsr} = -51.9 \text{ kms}^{-1}$) was corrected by $+12.2 \text{ kms}^{-1}$ in order to take into account the anomalous terminal CO velocities between $l = 300^\circ$ - 312° as described in Alvarez et al. (1990). After this correction, we noticed that its galactocentric radius ($R_{gal} = 6.88 \text{ kpc}$) is slightly smaller than the galactocentric radius at the tangent point of its line of sight ($l = 305^\circ.750$) given by $R_\odot \sin(l) = 6.90 \text{ kpc}$. Since the last is not allowed under the assumption of pure circular motion, the tangent galactocentric radius was chosen and the corresponding heliocentric distance assigned to the cloud.
- 5: Based on $^{13}\text{CO}(1-0)$ and HI absorption observations, Busfield et al. (2006) assigned the far distance to the IRAS/CS source G306.313–0.347 associated with this cloud. Since the HI data present no absorption at the $^{13}\text{CO}(1-0)$ radial velocity of this source, the location of the cloud at the far distance is almost certain.
- 6: The HII region G308.092–0.432 presents deep H_2CO absorption at -57 kms^{-1} and at -13 kms^{-1} , and recombination line emission at -17 kms^{-1} . The absorption features and the absence of an optical counterpart places the source almost certainly at the far distance (Caswell & Haynes 1987) and, by spatial and velocity coincidence,

its parent GMC.

- 7: The radial velocity of this cloud ($V_{lsr} = -59.5 \text{ kms}^{-1}$) was corrected by $+12.2 \text{ kms}^{-1}$ in order to take into account the anomalous terminal CO velocities between $l = 300^\circ - 312^\circ$ as described in Alvarez et al. (1990). After this correction, we noticed that its galactocentric radius ($R_{gal} = 6.59 \text{ kpc}$) is slightly smaller than the galactocentric radius at the tangent point of its line of sight ($l = 308^\circ.375$) given by $R_\odot \sin(l) = 6.66 \text{ kpc}$. Since the last is not allowed under the assumption of pure circular motion, the tangent galactocentric radius was chosen and the corresponding heliocentric distance assigned to the cloud.
- 8: Given the large velocity dispersion of the cloud ($\Delta v(FWHM) = 12.8 \text{ kms}^{-1}$), putting the cloud at the far distance yields a physical radius ($\sim 65 \text{ pc}$) more consistent with the observational size-to-linewidth relationship (*first Larson's Law*) than the physical radius estimated from the near distance ($\sim 30 \text{ pc}$). The continuity of the far side of the *Centaurus* spiral arm also suggests the far distance. Therefore, the far distance is assigned to the cloud.
- 9: The HII region G309.057+0.186 has a visual counterpart and exhibits recombination line emission at -47 kms^{-1} and no absorption, putting the cloud almost certainly at the near distance (Caswell & Haynes 1987). The 6.7 GHz methanol maser 308.754+0.549 is apparently associated to this cloud. The removal of its distance ambiguity done by Green & McClure-Griffiths (2011) seems to contradict our distance determination for the GMC. Nonetheless, there is an explanation for the discrepancy. The maser is very close to a local maximum, far from the bulk of the integrated CO

emission in the GMC’s spatial map. The local maximum can be attributed to a less massive cloud at the far distance (if the distance determination of the associated maser is right) whose CO emission overlaps in phase space with the CO emission of the GMC at the near distance. Since we are sensitive to only the most massive GMCs at the far distance, this is to be expected in some cases. In this sense, there is no contradiction with our determination of the GMC distance, because the maser is associated to a different and less massive cloud at the far distance that we can not properly isolate with the ASM subtraction technique applied in this work.

- 10: The HII region G310.994+0.389 is associated with the catalog object RCW82 (G311.00+0.40) (Caswell & Haynes 1987), locating the cloud at the near distance. The IRAS/CS source G311.625+0.291 (radial velocity from the CS(2-1) line is -56.2 kms^{-1}) associated with this cloud presents H_2CO absorption at -54 kms^{-1} and -49 kms^{-1} , and recombination line emission at -61 kms^{-1} also placing the cloud almost certainly at the near distance. The radial velocity of this cloud ($V_{lsr} = -53.2 \text{ kms}^{-1}$) was corrected by $+12.2 \text{ kms}^{-1}$ in order to take into account the anomalous terminal CO velocities between $l = 300^\circ - 312^\circ$ as described in Alvarez et al. (1990).
- 11: The IRAS/CS source G311.899+0.084 associated to the cloud presents a HI self-absorption feature at the same radial velocity of the recombination line emission locating the cloud almost certainly at the near distance (Goss et al. 1970; Caswell & Robinson 1974; Caswell et al. 1975). The IRAS/CS source G312.109+0.309 (radial velocity from the CS(2-1) line is -48.4 kms^{-1}) associated to this cloud presents H_2CO absorption and recombination line emission at -49 kms^{-1} (Caswell & Haynes 1987; Goss et al. 1970; Caswell & Robinson 1974; Caswell et al. 1975). Since no other

absorption feature is present along the line of sight, this suggests the near distance. Given the velocity dispersion of the cloud ($\Delta v(FWHM) = 9.4 \text{ kms}^{-1}$), putting the cloud at the near distance yields a physical radius (59 pc) more consistent with the observational size-to-linewidth relationship (*first Larson's Law*) than the physical radius estimated from the far distance (103 pc). Therefore, the near distance is assigned to the cloud.

- 12: Given the velocity dispersion of the cloud ($\Delta v(FWHM) = 10.9 \text{ kms}^{-1}$), putting the cloud at the far distance yields a physical radius ($\sim 62 \text{ pc}$) much more consistent with the observational size-to-linewidth relationship (*first Larson's Law*) than the physical radius estimated from the near distance ($\sim 6 \text{ pc}$). Locating the cloud at the near distance yields an heliocentric distance of 0.9 kpc to the cloud. In this case, the absence of an optical counterpart at such close distance is unlikely, suggesting also the far distance. The continuity of the far side of the *Centaurus* spiral arm also suggests the far distance. Therefore, the far distance is assigned to the cloud.
- 13: To assign a heliocentric distance to the cloud, we notice that its CO radial velocity ($V_{lsr} = -61.6 \text{ kms}^{-1}$) is very close to the CO terminal velocity ($V_{lsr} = -65 \text{ kms}^{-1}$) at the line of sight $l = 312^\circ.500$ (Alvarez et al. 1990). Its galactocentric radius ($R_{gal} = 6.07 \text{ kpc}$) is slightly smaller than the galactocentric radius at the tangent point given by $R_\odot \sin(l) = 6.27 \text{ kpc}$. Since the last is not allowed under the assumption of pure circular motion, we extend the Galactic longitude range suggested by Alvarez et al. (1990) and apply the $+12.2 \text{ kms}^{-1}$ correction to the radial velocity of the cloud. The new galactocentric radius $R_{gal} = 6.43 \text{ kpc}$ is slightly larger than the one at the tangent point of the line of sight. Since the calculated galactocentric radii are very close before

and after the correction (less than 5% difference), the galactocentric radius tangent to the line of sight was chosen, and the corresponding heliocentric distance assigned to the cloud.

- 14: Given the velocity dispersion of the cloud ($\Delta v(FWHM) = 9.3 \text{ kms}^{-1}$), putting this cloud at the far distance implies a large physical radius (148 pc), deviating the cloud from the observational size-to-linewidth relationship (*first Larson's Law*). The continuity of the near side of the *Centaurus* arm also suggests the near distance to this cloud. We also notice that clouds at distances further than 4 kpc usually subtend angular scales smaller than 1° (Green et al. 2011) while the angular size of the cloud in Galactic longitude is larger than 2° and in Galactic latitude it is larger than 1° . The 6.7 GHz methanol maser 314.320+0.112 is associated with this cloud. The removal of its distance ambiguity done by Green & McClure-Griffiths (2011) contradicts our distance determination for its parent GMC. The inspection of the spatial distribution of the CO emission as well as the longitude-velocity diagram does not show any particular structure at the position of the maser that could be associated with a less massive cloud at the far distance. In this case, there is no obvious explanation to account for the contradictory evidence. We stick to our result and adopt the near distance to the GMC.
- 15: The HII regions G314.183+0.314 and G314.228+0.473 present H₂CO absorptions features both at -61 kms^{-1} and recombination line emission at -62 kms^{-1} and -63 kms^{-1} . We notice that the terminal velocity at $l = 314^\circ.250$ is around -67 kms^{-1} (Alvarez et al. 1990), implying that the HII regions are either at the near or tangent distance. Since the absorption features at -61 kms^{-1} are close to the CO velocity of the cloud ($V_{lsr} = -57.6 \text{ kms}^{-1}$) and fall within its extension in radial velocity

($\Delta v(FWHM) \sim 8 \text{ kms}^{-1}$), we interpret this as the cloud being in front of the HII regions producing the absorption features, locating the cloud at the near distance.

- 16: At the position of the cloud, no observations of absorption or recombination line emission were found in the literature. We assign the far distance to the cloud based on observational size-to-linewidth relationship (*first Larson's Law*). Putting the cloud at the near distance yields a very small physical radius ($\sim 15 \text{ pc}$) deviating the cloud far away from the general trend ($\Delta v(FWHM) = 11.0 \text{ kms}^{-1}$). We also notice that, in general, clouds at the far distance tend to have a small solid angle and small Galactic latitude (because of the distance projection) but still, if the cloud is massive, a large velocity dispersion ($\Delta v(FWHM) > 10 \text{ kms}^{-1}$). This is in fact the case for this cloud.
- 17: Based on $^{13}\text{CO}(1-0)$ and HI absorption observations Busfield et al. (2006) assigned the far distance to the MYSO G318.2650–00.1269 which coincides in phase space with this cloud. Since the HI data present no absorption at the $^{13}\text{CO}(1-0)$ radial velocity of the MYSO, the location of this source and its parent cloud at the far distance is almost certain. Based also on HI absorption data, Urquhart et al. (2012) place the HII region G318.7251–0.2241 at the far distance. The observational size-to-linewidth relationship (*first Larson's Law*) also suggests the far distance. Putting the cloud at the near distance yields a very small physical radius ($\sim 13 \text{ pc}$) deviating the cloud far away from the general trend ($\Delta v(FWHM) = 12.8 \text{ kms}^{-1}$).
- 18: The HII region G320.153+0.780 is associated with the optical object RCW87 (G320.20+0.80) (Caswell & Haynes 1987; Wilson et al. 1970). The HII regions G319.874+0.770 and G316.808–0.037 present visual optical counterparts

(Caswell & Haynes 1987; Churchwell et al. 1974). Based on $^{13}\text{CO}(1-0)$ and HI absorption observations, Busfield et al. (2006) solved the distance ambiguity for the IRAS/CS source G316.810–0.070 associated to this cloud, putting it at the near distance. Based on HI absorption data, Urquhart et al. (2012) place the HII regions G317.4122+0.1050 and G318.7748–0.1513 at the near distance. The 6.7 GHz methanol maser 318.050+0.087 is associated to this cloud. The removal of its distance ambiguity done by Green & McClure-Griffiths (2011) confirms our distance determination for its parent GMC.

- 19: The HII region G319.157–0.423 and G319.380–0.025 listed by Caswell & Haynes (1987) present H_2CO absorption features at -20 km s^{-1} , and recombination line emission at -22 km s^{-1} and -14 km s^{-1} , respectively. No optical counterparts were found. The authors put these sources at the far distance. Since the H_2CO absorption radial velocity coincides with the CO radial velocity of the cloud ($V_{lsr} = -20.3 \text{ km s}^{-1}$), we locate the cloud at the far distance. Based on HI absorption data, Urquhart et al. (2012) place the HII regions G318.9148–0.1647, G319.1632–0.4208, and G319.3622+0.0126 at the far distance.
- 20: We assign the far distance to the cloud based on the following: given the velocity dispersion of the cloud ($\Delta v(FWHM) = 14.9 \text{ km s}^{-1}$), putting this cloud at the near distance implies an unrealistic small physical radius (5 pc), deviating the cloud from the observational size-to-linewidth relationship (*first Larson's Law*).
- 21: The HII region G320.317–0.208 (possible the same object as the IRAS/CS G320.316–0.180) presents H_2CO absorption at -11.4 km s^{-1} and recombination line

emission at -11 kms^{-1} (Caswell & Haynes 1987). The same occurs with the HII region G320.379+0.139 presenting H_2CO absorption and recombination line emission at the same velocity -3 kms^{-1} (Caswell & Haynes 1987). These observations and the lack of an optical counterpart places the cloud almost certainly at the far distance. Putting the cloud at the near distance leads to an unrealistic physical radius of $\sim 4 \text{ pc}$. The 6.7 GHz methanol maser 320.123–0.504 is associated with this cloud. The removal of its distance ambiguity done by Green & McClure-Griffiths (2011) contradicts our distance determination for its parent GMC. We notice that the maser coincide spatially and spectrally with the IRAS/CS G320.124–0.501 associated to this cloud. In the longitude-velocity diagram, there is no other CO emission feature around this GMC to which the maser could be associated, so the evidence suggests that the maser is indeed at the far distance. Given the strong evidence we have to put the cloud at the far distance, we believe that the distance determination of the maser may be wrong, so we stick to our distance estimate with the GMC at the far distance.

- 22: The IRAS/CS source G320.252–0.296 associated with this cloud presents H_2CO absorption at -13 kms^{-1} and recombination line emission at -68 kms^{-1} (Caswell & Haynes 1987). The absence of absorption features between the IRAS/CS radial velocity and the terminal velocity at its line of sight ($v_{term} \sim -76 \text{ kms}^{-1}$) suggests the near distance for the source. For the IRAS/CS source G320.332–0.307, Georgelin & Georgelin (1976) places it at the near distance applying the criterion of the continuity of the arms. We adopt the near distance to the cloud.
- 23: The HII regions G321.038–0.519 and G321.105–0.549 have visual optical counterparts (Caswell & Haynes 1987; Wilson et al. 1970). The IRAS/CS source

G321.057–0.520 is associated with the optical object RCW91 (G321.20–0.50) (Whiteoak & Gardner 1974; Caswell & Haynes 1987) locating the cloud at the near distance.

- 24: The HII region G324.192+0.109 present several H₂CO absorptions behind -92 kms^{-1} (Caswell & Haynes 1987) with no features between the recombination line velocity and the terminal velocity locating this region at the near distance. One of the H₂CO absorption features of this region occurs at -29 kms^{-1} , very close to the CO radial velocity of the cloud ($V_{lsr} = -31.6 \text{ kms}^{-1}$) locating the cloud in front of the HII region at the near distance. We also notice that, given the velocity dispersion of the cloud ($\Delta v(FWHM) = 4.7 \text{ kms}^{-1}$), putting this cloud at the far distance implies an unrealistic large physical radius (280 pc), deviating the cloud from the general trend observational size-to-linewidth relationship (*first Larson's Law*). The large angular extension of the cloud also supports the near distance.
- 25: The HII region G322.153+0.613 is associated with the optical object RCW92 (G322.20+0.60) locating the cloud at the near distance (Caswell & Haynes 1987; Wilson et al. 1970). Based on HI absorption data, Urquhart et al. (2012) place the HII region G322.1729+0.6442 at the near distance.
- 26: The Caswell & Reynolds (2001) paper is devoted to the IRAS/CS source G323.459–0.079, associated with this cloud. They place the source at the near distance, so we adopt the near distance to its parent cloud.
- 27: Given the velocity dispersion of the cloud ($\Delta v(FWHM) = 8.0 \text{ kms}^{-1}$), putting

the cloud at the near distance yields a physical radius (~ 44 pc) more consistent with the observational size-to-linewidth relationship (*first Larson’s Law*) than the physical radius estimated from the far distance (~ 121 pc). The continuity of the near side of the *Centaurus* spiral arm also suggests the near distance to this cloud.

- 28: Walsh et al. (2002) is devoted to the IRAS/CS source G323.740–0.254 associated with this cloud. From observations of the Bracket- γ recombination line of atomic hydrogen in the near-infrared the authors place the source at the near distance. Phillips et al. (1998) reports CH₃OH emission of two close sources: G323.740–0.263 (-51.2 kms⁻¹) and G323.741–0.263 (-57.1 kms⁻¹). Because of the high luminosity resulting at the far distance, the authors place the source “almost certainly” at the near distance. The HII region G324.192+0.109 present several H₂CO absorptions behind -92 kms⁻¹ (Caswell & Haynes 1987) with no features between the recombination line velocity and the terminal velocity locating this region at the near distance. One of the H₂CO absorption features occurs at -50 kms⁻¹, very close to the CO radial velocity of the cloud ($V_{lsr} = -45.3$ kms⁻¹, $\Delta v(FWHM) = 10.7$ kms⁻¹) locating the cloud in front of the HII region at the near distance. The 6.7 GHz methanol maser 323.740–0.263 is associated to this cloud. The removal of its distance ambiguity done by Green & McClure-Griffiths (2011) confirms our distance determination for its parent GMC.
- 29: The HII regions G326.230+0.976 and G326.315+0.689 and the IRAS/CS source G326.447+0.906 are associated with the optical object RCW94 (G326.20+0.90) (Georgelin & Georgelin 1976; Whiteoak & Gardner 1974; McClure-Griffiths et al. 2001; Caswell & Haynes 1987; Shaver et al. 1983). The IRAS/CS sources

G326.655+0.592, G326.726+0.613, and the HII region G326.645+0.589 are associated with the optical object RCW95 (G326.70+0.80) (Georgelin & Georgelin 1976; Caswell & Haynes 1987; Robinson et al. 1971; Goss et al. 1972; Shaver et al. 1982; Wilson et al. 1970). Concerning these sources, Goss et al. (1972) gives the HI spectrum at position (326°.6,+0°.6) showing absorption at -47 kms^{-1} . The authors place the source at the near distance. Robinson et al. (1971) reports OH absorption at -45 kms^{-1} , at the transitions 1665 MHz, 1667 MHz, and 1720 MHz, and emission at the same velocity at 1612 MHz. There is also absorption at -21 kms^{-1} at 1665 MHz and 1667 MHz. This reference places the source at the near distance. Based on HI absorption data, Urquhart et al. (2012) place the HII region G326.7249+0.6159 at the near distance.

- 30: The HII region G327.313–0.536 is associated with the optical object RCW97 (G327.30–0.55) putting the cloud at the near distance (Caswell & Haynes 1987). Based on HI absorption data, Urquhart et al. (2012) place the HII region G327.3017–0.5382 at the near distance.
- 31: The HII region G326.441–0.396 presents H_2CO absorption at -44 kms^{-1} and recombination line emission at -61 kms^{-1} (Caswell & Haynes 1987) locating the source at the near distance (at the $l = 326^\circ.500$ line of sight, the terminal velocity is $\sim -100 \text{ kms}^{-1}$ as shown by Alvarez et al. (1990)). The HII region G326.660–0.471 presents no H_2CO absorption but recombination line emission at -57 kms^{-1} (Caswell & Haynes 1987) locating the source almost certainly at the near distance. The HII region G326.959–0.031 presents H_2CO absorption at -57.3 kms^{-1} and -45.5 kms^{-1} , and recombination line emission at -64 kms^{-1} (Caswell & Haynes

1987) locating the source at the near distance (at the $l = 327^\circ.000$ line of sight, the terminal velocity is $\sim -107 \text{ kms}^{-1}$ as shown by Alvarez et al. (1990)). Since the CO radial velocity of the cloud is $V_{lsr} = -62.3 \text{ kms}^{-1}$ ($\Delta v(FWHM) = 10.8 \text{ kms}^{-1}$), we associate the previous HII regions to the cloud and put it at the near distance. Based on HI absorption data, Urquhart et al. (2012) place the HII region G326.4719–0.3777 at the near distance.

- 32: The HII region G328.593–0.518 associated to the optical object RCW99 (G328.57–0.53) which locates this source at the near distance (Caswell & Haynes 1987). The source presents H_2CO absorptions features at -71.5 kms^{-1} and -46.1 kms^{-1} , and recombination line emission at -51 kms^{-1} . We notice that the absorption feature coincides with the CO radial velocity of the cloud $V_{lsr} = -70.7 \text{ kms}^{-1}$. Although the absorption feature at -70 kms^{-1} occurs at larger velocities (more negative) than the one of the recombination line emission, the full width at half maximum of the recombination line ($\Delta v(FWHM) = 27 \text{ kms}^{-1}$) shows that the absorption feature falls within $2 \times \sigma_v$ of its velocity profile. Therefore, such feature can not be assigned directly to the cloud in front of the HII region. Based on HI absorption data, Urquhart et al. (2012) place the HII region G327.7579–0.3515 at the near distance. Given the velocity dispersion of the cloud ($\Delta v(FWHM) = 11.3 \text{ kms}^{-1}$), putting this cloud at the far distance implies a large physical radius (137 pc), deviating the cloud from the general trend of the observational size-to-linewidth relationship (*first Larson's Law*). The continuity of the near side of the *Centaurus* spiral arm also suggests the near distance.

- 33: The HII region G328.593–0.518 is associated to the optical object RCW99

(G328.57–0.53) which locate this source at the near distance (Caswell & Haynes 1987). The source presents H₂CO absorptions features at -71.5 kms^{-1} and -46.1 kms^{-1} , the latter coinciding with the CO velocity of the cloud ($V_{lsr} = -45.0 \text{ kms}^{-1}$), putting the cloud in front of the HII region at the near distance. For the IRAS/CS source G328.191–0.571 associated to this cloud, Georgelin & Georgelin (1976) reported the distance to the exiting stars (2.6 kpc) at position ($328^{\circ}.1, -0^{\circ}.5$) locating this cloud at the near distance. Using recombination line velocities (v_{rrl}) from continuum sources and HI absorptions along the same line of sight, Jones & Dickey (2012) locates the continuum source G328.567–0.533 ($v_{rrl} = -51 \text{ kms}^{-1}$) associated to the cloud at the near distance. The 6.7 GHz methanol masers 329.029–0.205, 329.031–0.198, and 329.066–0.308 are associated with this cloud. The removal of its distance ambiguity done by Green & McClure-Griffiths (2011) contradicts our distance determination for the parent GMC. We notice that the maser 329.066–0.308 coincides spatially and spectrally with the IRAS/CS G329.066–0.307 associated to the GMC. The inspection of the spatial distribution of the CO emission as well as the longitude-velocity diagram shows a structure at the position of the masers that could represent a different cloud at the far distance overlapping with this GMC in phase space. The fact that the masers are all around the same CO emission contour, far from the peak of the CO emission in the CO spatial map of the cloud, suggests that they could be indeed tracing another cloud. Since our evidence to put the GMC at the near distance is strong, but the sources found in the literature to assign the near distance go only up to $l = 328^{\circ}.576$, we can not discard that the masers located at larger longitudes are indeed tracing a different GMC.

- 34: The HII region G328.310+0.448 presents H₂CO absorption at -92 kms^{-1} and -52 kms^{-1} , with recombination line emission at -97 kms^{-1} (Caswell & Haynes

1987). Because of its proximity to the terminal velocity ($\sim -111 \text{ kms}^{-1}$ as shown by Alvarez et al. (1990)) and the lack of absorption features toward higher (more negative) velocities, the source is located either at the tangent or at the near distance. Since the CO radial velocity of the cloud ($V_{lsr} = -92.0 \text{ kms}^{-1}$) coincides with the absorption feature, we assign the near distance to the cloud. Using recombination line velocities (v_{rrl}) from continuum sources and HI absorptions along the same line of sight, Jones & Dickey (2012) locates the continuum source G328.311+0.433 ($v_{rrl} = -97 \text{ kms}^{-1}$) associated to the cloud at the near distance. The 6.7 GHz methanol masers 327.590–0.094 and 327.618–0.111 are apparently associated to this cloud. The removal of their distance ambiguity done by Green & McClure-Griffiths (2011) seems to contradict our distance determination for the GMC. Nonetheless, there is an explanation for the discrepancy. The masers are very close to a local maximum, far from the bulk of the integrated CO emission in the GMC’s spatial map. The local maximum can be attributed to a less massive cloud at the far distance (if the distance determination of the associated masers are right) whose CO emission overlaps in phase space with the CO emission of the GMC at the near distance. Since we are sensitive to only the most massive GMCs at the far distance, this is to be expected in some cases. In this sense, there is no contradiction with our determination of the GMC distance, because the masers are associated to a different and less massive cloud at the far distance that we can not properly isolate with the ASM subtraction technique applied in this work.

- 35: In the case of this cloud, none of the previous methods could distinguish between near and far distance, and therefore, no distance was assigned to the cloud. The 6.7 GHz methanol maser 329.469+0.503 is apparently associated to this cloud. The removal of its distance ambiguity done by Green & McClure-Griffiths (2011) seems

to contradict our distance determination for the GMC. Nonetheless, there is an explanation for the discrepancy. The maser is very close to a local maximum, far from the bulk of the integrated CO emission in the GMC’s spatial map. The local maximum can be attributed to a less massive cloud at the far distance (if the distance determination of the associated maser is right) whose CO emission overlaps in phase space with the CO emission of the GMC at the near distance. Since we are sensitive to only the most massive GMCs at the far distance, this is to be expected in some cases. In this sense, there is no contradiction with our determination of the GMC distance, because the maser is associated to a different and less massive cloud at the far distance that we can not properly isolate with the ASM subtraction technique applied in this work.

- 36: In the case of this cloud, none of the previous methods could distinguish between near and far distance, and therefore, no distance was assigned to the cloud.

- 37: The HII region G329.353+0.144 presents H₂CO absorption at -106 km s^{-1} and -85 km s^{-1} , recombination line emission at -107 km s^{-1} , and HI absorption at -109 km s^{-1} (Caswell & Haynes 1987; McClure-Griffiths et al. 2001) locating this source either at the near or tangent distance. The same occurs for the HII region G329.489+0.207 which presents H₂CO absorption at -100 km s^{-1} , recombination line emission at -102 km s^{-1} , and HI absorption at -109 km s^{-1} (Caswell & Haynes 1987; McClure-Griffiths et al. 2001). For both sources, Caswell & Haynes (1987) assigned them the tangent distance. Since the CO radial velocity of the cloud $V_{lsr} = -99.0 \text{ km s}^{-1}$ coincides with the absorption feature at -100 km s^{-1} , we locate the cloud in front of the HII region, at the near distance. Using recombination line velocities

(v_{rrl}) from continuum sources and HI absorptions along the same line of sight, Jones & Dickey (2012) locates the continuum sources G329.478+0.211 ($v_{rrl} = -102$ kms $^{-1}$) and G329.333+0.144 ($v_{rrl} = -107$ kms $^{-1}$) at the tangent point, behind the cloud.

- 38: The HII region G329.353+0.144 presents H₂CO absorption at -106 kms $^{-1}$ and -85 kms $^{-1}$ and recombination line emission at -107 kms $^{-1}$. Since the terminal velocity at $l = 329^{\circ}.5$ is around -110 kms $^{-1}$ (Alvarez et al. 1990), Caswell & Haynes (1987) locate the source at the tangent distance. The absorption at -85 kms $^{-1}$ falls within the CO velocity distribution of the cloud ($V_{lsr} = -80.9$ kms $^{-1}$, $\Delta v(FWHM) = 9.4$ kms $^{-1}$), putting the cloud in front of the source at the near distance. Using recombination line velocities (v_{rrl}) from continuum sources and HI absorptions along the same line of sight, Jones & Dickey (2012) locates the continuum sources G329.478+0.211 ($v_{rrl} = -102$ kms $^{-1}$) and G329.333+0.144 ($v_{rrl} = -107$ kms $^{-1}$) at the tangent point, behind the cloud. The 6.7 GHz methanol maser 329.622+0.138 is apparently associated to this cloud. The removal of its distance ambiguity done by Green & McClure-Griffiths (2011) seems to contradict our distance determination for the GMC. The maser mid-velocity $v_{mid} = -84.7$ kms $^{-1}$ is almost the same as the velocity of the peak emission in the spectrum $v_{peak} = -85.0$ kms $^{-1}$ which, in turn, is identical to the formaldehyde absorption at -85.0 kms $^{-1}$. Green & McClure-Griffiths (2011) put the maser at the far distance due to the lack of HI self-absorption at the mid-velocity. Nonetheless, the HI spectrum of this maser presents a sharp decrease in brightness temperature around ± 5 kms $^{-1}$ of v_{mid} that the authors do not attribute to be an absorption feature. We believe that our distance determination for the GMC is solid and that the methanol maser may have been incorrectly assigned to the far distance due to the complex HI spectrum it shows.

- 39: In the case of this cloud, none of the previous methods could distinguish between near and far distance, and therefore, no distance was assigned to the cloud.

- 40: The location of the cloud in Galactic latitude ($b = 1^\circ.000$) favors the near distance. Putting the cloud at the far distance yields a distance off the plane of 146 pc toward positive latitudes. This is in contradiction with the molecular gas distribution at the galactocentric radius of the cloud $R_{gal} = 4.66$ kpc (for $R_\odot = 8.5$ kpc). The centroid of the molecular gas distribution lies at $z \sim 45$ pc, with a half width half maximum extension of ~ 81 pc (Bronfman et al. 1988b) at this galactocentric radius. We adopt the near distance to the cloud.

- 41: The HII region G332.148–0.446 has an optical counterpart suggesting the near distance (Caswell & Haynes 1987). The IRAS/CS source G330.883–0.369 is discussed in Bash & Leisawitz (1985) as having an anomalous velocity. It is placed at 5.0 kpc, corresponding to the near distance. The IRAS/CS source G331.169–0.455 Whiteoak & Gardner (1970) shows observations of 4830 MHz H_2CO absorption pointing to $331^\circ.1-0^\circ.4$. They report also 1667 MHz OH emission at -41.8 kms^{-1} . This reference places the source at the near distance. The IRAS/CS source G331.333–0.339 Caswell et al. (1975) presents a HI spectrum which shows deep absorption features at about -69 kms^{-1} and -47 kms^{-1} . In an individual note the authors discuss “a single weak possible absorption feature at -94 kms^{-1} ”, however the authors favor the near kinematic distance. Based on HI absorption data, Urquhart et al. (2012) place the HII regions G330.8708–0.3715, G331.1194–0.4955, and G331.4181–0.3546 at the near distance. Using recombination line velocities (v_{rrl}) from continuum sources

and HI absorptions along the same line of sight, Jones & Dickey (2012) locates the continuum source G330.867–0.367 ($v_{rrl} = -56 \text{ kms}^{-1}$), G330.678–0.389 ($v_{rrl} = -61 \text{ kms}^{-1}$), and G331.122–0.533 ($v_{rrl} = -68 \text{ kms}^{-1}$) associated to the cloud at the near distance.

- 42: The HII region G331.026–0.152 presents H_2CO absorption features at -92.2 kms^{-1} and -46.7 kms^{-1} and recombination line emission at -89 kms^{-1} (Caswell & Haynes 1987; Wilson et al. 1970), putting the source at the far distance. According to the pure circular motion assumption, since the recombination line emission occurs at -89 kms^{-1} , the absorption feature at -46.7 kms^{-1} must be located at the near distance. We identify this absorption feature as being produced by the cloud ($V_{lsr} = -45.3 \text{ kms}^{-1}$, and $\Delta v(FWHM) = 8.6 \text{ kms}^{-1}$) along the line of sight of the HII region, locating the cloud at the near distance.
- 43: Caswell et al. (1975) presents a HI spectrum for the IRAS/CS source G331.552–0.115 showing absorption at -90 kms^{-1} and $\text{H}109\alpha$ emission at -89 kms^{-1} . The authors discuss extensively this source and place it at near distance. The HII region G331.517–0.069 has absorption features at -99.8 kms^{-1} and -89.3 kms^{-1} and recombination line emission at -89 kms^{-1} (Caswell & Haynes 1987). Based on HI absorption data, they put the region at the near distance. Goss et al. (1970) presents OH spectra for the same source showing emission between -87 kms^{-1} and -95 kms^{-1} specially at 1665 MHz. Using recombination line velocities (v_{rrl}) from continuum sources and HI absorptions along the same line of sight, Jones & Dickey (2012) locates the continuum sources G331.522–0.078 ($v_{rrl} = -89 \text{ kms}^{-1}$), G331.055–0.144 ($v_{rrl} = -89 \text{ kms}^{-1}$), G331.278–0.189 ($v_{rrl} = -85 \text{ kms}^{-1}$),

and G331.055–0.222 ($v_{rrl} = -89 \text{ kms}^{-1}$), associated to the cloud at the tangent point. This is due to the their adopted tolerance for the difference between the terminal and LSR velocity of the source (25 kms^{-1}) to assign it to the tangent point, which is larger than the one we use in this work (10 kms^{-1}) . We adopt the near distance to the cloud.

- 44: The HII region G332.978+0.792, associated to this cloud presents H_2CO absorption at -48.4 kms^{-1} and recombination line emission at -52 kms^{-1} (Caswell & Haynes 1987). The absence of absorption features between the emission and terminal velocities places the source almost certainly at the near distance. Based on HI absorption data, Urquhart et al. (2012) place the HII regions G333.0058+0.7707 and G333.0162+0.7615 at the near distance. Using recombination line velocities (v_{rrl}) from continuum sources and HI absorptions along the same line of sight, Jones & Dickey (2012) locates the continuum source G332.978+0.767 ($v_{rrl} = -52 \text{ kms}^{-1}$) associated to the cloud at the near distance.
- 45: The HII region G332.662–0.607 is associated to the optical RCW106 (G332.90–0.60) locating the cloud at the near distance (Shaver et al. 1983; Shaver & Goss 1970). Based on HI absorption data, Urquhart et al. (2012) place the HII regions G332.1544–0.4487 to G332.8256–0.5498, G333.0145–0.4438, and from G333.1306–0.4275 to G333.6032–0.2184 at the near distance. The observational size-to-linewidth relationship (*first Larson’s Law*) also suggests the near distance. Putting the cloud at the far distance yields an unrealistic large physical radius ($\sim 218 \text{ pc}$) deviating the cloud far away from the general trend ($\Delta v(FWHM) = 8.9 \text{ kms}^{-1}$). Using recombination line velocities (v_{rrl}) from continuum sources and HI absorptions along the same line of sight, Jones & Dickey (2012) locates the continuum

sources G333.133–0.433 ($v_{rrl} = -52 \text{ kms}^{-1}$), G332.833–0.555 ($v_{rrl} = -57 \text{ kms}^{-1}$), and G332.656–0.611 ($v_{rrl} = -48 \text{ kms}^{-1}$), associated in phase space to the cloud at the near distance, and the G333.689–0.444 ($v_{rrl} = -50 \text{ kms}^{-1}$), also associated in phase space to the cloud at the far distance. Most of the evidence favors the near distance to the cloud. The 6.7 GHz methanol masers 332.352–0.117 and 332.960+0.135 are associated to this cloud. The removal of their distance ambiguity done by Green & McClure-Griffiths (2011) confirms our distance determination for their parent GMC.

- 46: The region HII G333.168–0.081 presents H_2CO absorption features at -88.6 kms^{-1} and -46.6 kms^{-1} , and recombination line emission at -91 kms^{-1} (Caswell & Haynes 1987). The lack of absorption features at higher (more negative) velocities, put this source at the near distance, with this cloud in front of it absorbing at -88.6 kms^{-1} , the same CO radial velocity of the cloud ($V_{lsr} = -88.1 \text{ kms}^{-1}$). For the IRAS/CS source G333.168–0.104 Caswell & Haynes (1975) reports 1612 MHz OH emission at -87 kms^{-1} and absorption at -41 kms^{-1} at position $(333^\circ.1, -0^\circ.1)$ suggesting the near distance for the source. The authors note that this source is associated with an extensive cloud, which is also detected at 100 adjacent positions. Using recombination line velocities (v_{rrl}) from continuum sources and HI absorptions along the same line of sight, Jones & Dickey (2012) locates the continuum source G333.167–0.100 ($v_{rrl} = -91 \text{ kms}^{-1}$) at the tangent point, just behind the cloud.
- 47: Because of the proximity of its CO radial velocity ($V_{lsr} = -105.0 \text{ kms}^{-1}$) to the terminal velocity at $l = 334^\circ$ ($v_{term} = -116 \text{ kms}^{-1}$ as shown by Alvarez et al. (1990)), the difference between the far and near distances to this cloud (2.7 kpc) is not as

large as in other parts of the longitude velocity diagram. The observational size-to-linewidth relationship and the continuity of the near side of the *Norma* spiral arm place the cloud at the near distance. Using recombination line velocities (v_{rrl}) from continuum sources and HI absorptions along the same line of sight, Jones & Dickey (2012) locates the continuum source G333.167–0.100 ($v_{rrl} = -91 \text{ kms}^{-1}$) at the tangent point, that would lie in front of the cloud. We adopt the near distance to the cloud.

- 48: The HII region G334.173+0.068 presents H_2CO absorption at -86 kms^{-1} and -40 kms^{-1} and recombination line emission at -70 kms^{-1} (Caswell & Haynes 1987). The presence of an absorption feature toward the terminal velocity locates the source at the far distance. Since the cloud is located along the line of sight of this HII region at $V_{lsr} = -62.2 \text{ kms}^{-1}$, the absence of absorption features within the velocity dispersion of the cloud locates it behind the HII region at the far distance. We also notice that, in general, clouds at the far distance tend to have a small solid angle and small Galactic latitude (because of the distance projection) but still, if the cloud is massive, a large velocity dispersion ($\Delta v(FWHM) > 10 \text{ kms}^{-1}$). This is in fact the case for this cloud.
- 49: The HII region G335.751+0.110 and G335.978+0.185 present H_2CO absorption features at -38 kms^{-1} and -37 kms^{-1} , and recombination line emission -51 kms^{-1} and -79 kms^{-1} respectively (Caswell & Haynes 1987). The absence of absorption features between the recombination line velocity and terminal velocity at the line of sight ($\sim -131 \text{ kms}^{-1}$ at $l = 336^\circ$ as shown by Alvarez et al. (1990)) strongly supports the near distance for these sources and the position of the cloud in front of them absorbing against their continuum emission ($V_{lsr} = -40.4 \text{ kms}^{-1}$, and $\Delta v(FWHM)$

$= 8.2 \text{ kms}^{-1}$), locating the cloud at the near distance. Putting the cloud at the far distance yields an unrealistic large physical radius ($\sim 258 \text{ pc}$) deviating the cloud far away from the general trend of the size-to-linewidth relationship ($\Delta v(FWHM) = 8.2 \text{ kms}^{-1}$). The 6.7 GHz methanol maser 335.060–0.427 is associated to this cloud. The removal of its distance ambiguity done by Green & McClure-Griffiths (2011) confirms our distance determination for its parent GMC.

- 50: The cloud is located far off the Galactic plane, at $b = -0^\circ.875$. Putting this cloud at the far distance implies a distance off the plane of 182 pc toward negative latitudes. Bronfman et al. (1988b) estimated the distribution of the molecular layer for the southern Galaxy. At the galactocentric radius of this cloud ($R_{gal} = 5.4 \text{ kpc}$), the molecular ring centroid lies at $z = -5 \text{ pc}$, with a half width half maximum extension of $\sim 68 \text{ pc}$. Following the molecular gas distribution, a far distance to this cloud results unlikely. Therefore, we adopt the near distance in this case.
- 51: The IRAS/CS source G336.872–0.014 presents OH absorption at -120 kms^{-1} , HI absorption at -128 kms^{-1} , and recombination line emission at -78.9 kms^{-1} locating the source at the far distance (McGee et al. 1967; Kerr & Knapp 1970; Wilson et al. 1970). The IRAS/CS source G337.121–0.174 presents H_2CO absorption at -119.6 kms^{-1} and at -73.7 kms^{-1} , OH absorption at -118 kms^{-1} (and around this velocity), HI absorption at -116 kms^{-1} and recombination line emission at -73 kms^{-1} suggesting the far distance (Caswell & Haynes 1987; Turner 1979; Caswell et al. 1975; Wilson et al. 1970). The presence of absorption features in several lines between the recombination line velocity and the tangent velocity at $l = 339^\circ$ (-128 kms^{-1} as shown by Alvarez et al. (1990)) in these two sources locates this cloud almost

certainly at the far distance. Based on HI absorption data, Urquhart et al. (2012) place the HII regions G336.8324+0.0301, G337.0047+0.3226, G337.7091+0.0932, and G337.1218–0.1748 at the far distance. Using recombination line velocities (v_{rrl}) from continuum sources and HI absorptions along the same line of sight, Jones & Dickey (2012) locates the continuum sources G337.711+0.089 ($v_{rrl} = -76.7 \text{ kms}^{-1}$), G337.122–0.178 ($v_{rrl} = -73 \text{ kms}^{-1}$), G336.911–0.155 ($v_{rrl} = -73 \text{ kms}^{-1}$), and G336.844–0.000 ($v_{rrl} = -79 \text{ kms}^{-1}$) associated to the cloud at the far distance. The 6.7 GHz methanol masers 337.202–0.094 and 337.258–0.101 are associated to this cloud. The removal of their distance ambiguity done by Green & McClure-Griffiths (2011) confirms our distance determination for their parent GMC.

- 52: The cloud is located far off the Galactic plane, at $b = -1^\circ.125$. Putting this cloud at the far distance implies a distance off the plane of 242 pc toward negative latitudes. Bronfman et al. (1988b) estimated the distribution of the molecular layer for the southern Galaxy. At the galactocentric radius of this cloud ($R_{gal} = 5.6 \text{ kpc}$), the molecular ring centroid lies at $z = -18 \text{ pc}$, with a half width half maximum extension of $\sim 76 \text{ pc}$. Following the molecular gas distribution, a far distance to this cloud results unlikely. Therefore, we adopt the near distance in this case.
- 53: For the IRAS/CS source G336.888+0.049 associated to this cloud, McGee et al. (1967) reports 1665 MHz OH absorption at -120 kms^{-1} and -53.2 kms^{-1} for position $(336^\circ.8, +0^\circ.05)$. Considering the CS radial velocity of this source at -121.2 kms^{-1} we locate it at the near distance. Georgelin & Georgelin (1976) discusses the three close sources G336.8+0.0, G336.9–0.1, and G337.1–0.2 (“group 4”) and places them at the near distance. For the IRAS/CS source G336.993–0.023 associated to this cloud,

Walsh et al. (1997) reports CH_3OH emission at -126 km s^{-1} and adopts a distance of 9.3 kpc (close to the tangent point, for $R_\odot = 10 \text{ kpc}$ and $\Theta_\odot = 250 \text{ km s}^{-1}$), probably because of the resulting spectral type of the exciting star. Using recombination line velocities (v_{rrl}) from continuum sources and HI absorptions along the same line of sight, Jones & Dickey (2012) locates the continuum source G337.533–0.311 ($v_{rrl} = -101 \text{ km s}^{-1}$) associated to the cloud at the tangent point. The source lies just above the lowest intensity contour, so the spatial association with the cloud is dubious. We adopt the near distance to the cloud.

- 54: The HII region G338.014–0.121 presents H_2CO absorption at -88 km s^{-1} and at -49 km s^{-1} and recombination line emission at -54 km s^{-1} (Caswell & Haynes 1987). The HII region G338.131–0.173 presents H_2CO absorption at -89.1 km s^{-1} and -42.7 km s^{-1} and recombination line emission at -53 km s^{-1} . Caswell & Haynes (1987) uses the H_2CO data from Whiteoak & Gardner (1974) and Gardner & Whiteoak (1984) to study the position of the HII region G337.665–0.048 which presents H_2CO absorption at -94.4 km s^{-1} and at -47.5 km s^{-1} and recombination line emission at -55 km s^{-1} . In these three cases, the presence of H_2CO absorption features at velocities higher (more negative) than the recombination line velocity put these sources at the far distance, and because of the spatial and velocity coincidence of the sources with the cloud, we assigned the far distance to the cloud. Fish et al. (2003) presents a HI spectrum at position $(337^\circ.7, -0^\circ.05)$ (coinciding with the IRAS/CS G337.703–0.052 associated to this cloud), showing absorption at -50 km s^{-1} and -106 km s^{-1} . The authors assigned the far distance to the source. Based on HI absorption data, Urquhart et al. (2012) place the HII regions G337.6651–0.1750, and G337.7051–0.0575 at the far distance. Using recombination line velocities (v_{rrl}) from continuum sources and HI absorptions along the same line of sight,

Jones & Dickey (2012) locates the continuum sources G338.122–0.189 ($v_{rrl} = -53$ kms $^{-1}$), G338.078+0.011 ($v_{rrl} = -47$ kms $^{-1}$), G337.711–0.056 ($v_{rrl} = -50$ kms $^{-1}$), G337.622–0.067 ($v_{rrl} = -55$ kms $^{-1}$), G337.667–0.167 ($v_{rrl} = -53$ kms $^{-1}$), and G337.289–0.122 ($v_{rrl} = -54$ kms $^{-1}$), associated to the cloud at the far distance. The 6.7 GHz methanol maser 337.632–0.079 is associated with this cloud. The removal of its distance ambiguity done by Green & McClure-Griffiths (2011) contradicts our distance determination for its parent GMC. The maser is spatially close to the associated IRAS/CS G337.616–0.061, but ~ 10 kms $^{-1}$ appart in LSR velocity. The inspection of the spatial distribution of the CO emission as well as the longitude-velocity diagram does not show any particular structure at the positon of the maser that could be associated with a less massive cloud at the near distance. In this case, there is no obvious explanation to account for the discrepancy. Since our evidence to adopt the far distance to the GMC is strong, we stick to our result in this case.

- 55: The HII region G337.548–0.304 presents H₂CO absorption at -62 kms $^{-1}$ and -35 kms $^{-1}$ and recombination line emission at -101 kms $^{-1}$ (Caswell & Haynes 1987). The absence of absorption features at larger velocities suggests the near distance for the source. Because of the spatial and velocity coincidence of the HII region with the cloud, we assign the near distance to the GMC. Using recombination line velocities (v_{rrl}) from continuum sources and HI absorptions along the same line of sight, Jones & Dickey (2012) locates the continuum source G337.533–0.311 ($v_{rrl} = -101$ kms $^{-1}$) at the tangent point, just behind of the cloud.
- 56: The cloud is located far off Galactic the plane, at $b = -1^{\circ}.000$. Putting this cloud at the far distance (9.4 kpc) implies a distance off the plane of 164 pc toward negative

latitudes (and 206 pc at the far distance of 11.8 kpc suggested by Dame & Thaddeus (2008) for the far side of the arm). Bronfman et al. (1988b) estimated the distribution of the molecular layer for the southern Galaxy. At the galactocentric radius of this cloud ($R_{gal} = 3.5$ kpc), the molecular ring centroid lies at $z = -12$ pc, with a half width half maximum extension of ~ 70 pc. Following the molecular gas distribution, a far distance to this cloud results unlikely. Therefore, we adopt the near distance in this case.

- 57: The HII region G339.089–0.216 associated to the cloud presents no absorption features but recombination line emission at -120 kms^{-1} and is placed at the tangent distance by Caswell & Haynes (1987). For the IRAS/CS source G338.569–0.145, Caswell & Haynes (1975) presents 1612 MHz OH spectrum at position ($338^{\circ}.5, -0^{\circ}.2$), showing emission at -128 kms^{-1} and no absorption features. We also notice that the CO tangent velocity at the line of sight $l = 338^{\circ}.500$ is -126 kms^{-1} (Alvarez et al. 1990), very close to the CO radial velocity of the cloud ($V_{lsr} = -119.1 \text{ kms}^{-1}$). We adopt the near distance to the cloud. The 6.7 GHz methanol maser 339.053–0.315 is associated to this cloud. Using the HI self-absorption method, Green & McClure-Griffiths (2011) put the source at the far distance. This contradicts our determination of the distance to this GMC. The cloud is clearly associated to the near side of the *3-kpc expanding* arm in the longitude-velocity diagram. Since it is known that the arm is expanding, the assumption that presence/absence of a HI self-absorption feature at the same LSR velocity would removed the distance ambiguity (near or far) of the masers at this Galacocentric radius is not clear. Given the LSR expansion velocity of both arm sides (near and far), by definition, there is no material at the same LSR velocity to compare with. Hence, there will be always an absence of HI self-absorption that will put the masers artificially at the far distance.

Also, the invariant manifolds models of Romero-Gómez et al. (2011b) reproduce very well the near side of the *3-kpc expanding* arm in the longitude-velocity diagram, region that coincides with the position of this GMC.

- 58: We assign the near distance to the cloud based on observational size-to-linewidth relationship (*first Larson's Law*). Putting the cloud at the far distance yields a large physical radius (~ 103 pc) deviating the cloud from the general trend of the relationship ($\Delta v(FWHM) = 6.8 \text{ kms}^{-1}$).
- 59: The HII region G338.742+0.641 has a visual optical counterpart (Caswell & Haynes 1987). HI absorption data of the source HII region G338.943+0.604 place this cloud at the near distance (Caswell & Haynes 1987). For the IRAS/CS source G338.851+0.406, Turner (1979) presents the OH spectrum showing emission at -62 kms^{-1} , -60 kms^{-1} , and -40 kms^{-1} at 1665 MHz, 1612 MHz, and 1720 MHz, respectively, and absorption at -2 kms^{-1} at 1667 MHz. The absence of absorption toward the terminal velocity (-128 kms^{-1} as shown by (Alvarez et al. 1990)) at the line of sight $l = 339^\circ.000$ locates this source at the near distance. Based on HI absorption data, Urquhart et al. (2012) place the HII region G338.9217+0.6233 at the near distance. Using recombination line velocities (v_{rrl}) from continuum sources and HI absorptions along the same line of sight, Jones & Dickey (2012) locates the continuum source G338.922+0.622 ($v_{rrl} = -63 \text{ kms}^{-1}$) and G338.711-0.644 ($v_{rrl} = -62 \text{ kms}^{-1}$) associated to the cloud at the near distance.
- 60: We based our determination of the near or far distance to this cloud by inspection of the CO latitude-velocity maps in Bronfman et al. (1989). We notice that, in

general, clouds at the far distance tend to have a small solid angle and small Galactic latitude (because of the distance projection) but still, if the cloud is massive, a large velocity dispersion ($\Delta v(FWHM) \sim 10 \text{ kms}^{-1}$). The elongated structure in radial velocity of this cloud is very similar to those “far” clouds with better determination of their distance ambiguity. It is also interesting to notice that placing the cloud at the far distance, there is a much better agreement between the molecular and viral masses of the cloud, within a factor of two, while at the near distance, the difference between the masses is increased to a factor of 4. The location of the cloud in the longitude-velocity diagram does not allow to distinguish between far and near distances mainly because of the position of the “far distance” clouds of the *3-kpc expanding* arm. Although the continuity of the near side of the *Norma* spiral arm suggests the near side to the cloud, it cannot be ruled out that the cloud belongs to the far side of the *3-kpc expanding* arm. Since the near and far sides of the *3-kpc expanding* arm are separated by more than 100 kms^{-1} (Dame & Thaddeus 2008), some clouds at the far distance are expected to cross the *Norma* and *Centaurus* spiral arms along the radial velocity axis above Galactic longitude $l = 337^\circ$ (tangent point). We choose the far distance to the cloud, but the near distance can not be ruled out completely.

- 61: Using recombination line velocities (v_{rrl}) from continuum sources and HI absorptions along the same line of sight, Jones & Dickey (2012) locates the continuum source G339.289+0.233 ($v_{rrl} = -71 \text{ kms}^{-1}$) associated to the cloud at the far distance. Given the velocity dispersion of the cloud ($\Delta v(FWHM) = 9.3 \text{ kms}^{-1}$), putting the cloud at the far distance yields a physical radius ($\sim 61 \text{ pc}$) more consistent with the observational size-to-linewidth relationship (*first Larson’s Law*) than the physical radius estimated from the near distance ($\sim 29 \text{ pc}$). Therefore, the far

distance is assigned to the cloud. We also notice that, in general, clouds at the far distance tend to have a small solid angle and small Galactic latitude (because of the distance projection) but still, if the cloud is massive, a large velocity dispersion ($\Delta v(FWHM) \sim 10 \text{ kms}^{-1}$). The elongated structure in radial velocity of this cloud is very similar to those “far” clouds with better determination of their distance ambiguity.

- 63: The HII region G339.128–0.408 associated to the cloud has a visual counterpart and presents recombination line emission at -37 kms^{-1} but no absorption features (Caswell & Haynes 1987), putting the cloud at the near distance. Given the velocity dispersion of the cloud ($\Delta v(FWHM) = 7.2 \text{ kms}^{-1}$), putting the cloud at the near distance yields a physical radius ($\sim 31 \text{ pc}$) much more consistent with the observational size-to-linewidth relationship (*first Larson’s Law*) than the physical radius estimated from the far distance ($\sim 156 \text{ pc}$). The cloud is located far off the Galactic plane at $b = -1^\circ.250$. Putting this cloud at the far distance implies a distance off the plane of 288 pc toward negative latitudes. Bronfman et al. (1988b) estimated the distribution of the molecular layer for the southern Galaxy. At the galactocentric radius of this cloud ($R_{gal} = 6.0 \text{ kpc}$), the molecular ring centroid lies at $z = -13 \text{ pc}$, with a half width half maximum extension of $\sim 53 \text{ pc}$. Following the molecular gas distribution, a far distance to this cloud results unlikely. Therefore, we adopt the near distance in this case. The 6.7 GHz methanol maser 340.034–1.110 is associated to this cloud. The removal of its distance ambiguity done by Green & McClure-Griffiths (2011) confirms our distance determination for its parent GMC.
- 65: The HII region G341.050–0.100 has a visual counterpart and presents H_2CO absorption at -42 kms^{-1} (Caswell & Haynes 1987), very close to the CO radial

velocity of the cloud ($V_{lsr} = -42.9 \text{ kms}^{-1}$) locating it at the near distance. The IRAS/CS source G340.053–0.237 associated to this cloud presents absorption at -53.2 kms^{-1} and -35.3 kms^{-1} and recombination line emission at -52 kms^{-1} (Whiteoak & Gardner 1974; Caswell & Haynes 1987). Considering that the CS line velocity for this source is at -53.1 kms^{-1} and the absence of absorption features between the emission and terminal velocities, the source is located at the near distance. Based on HI absorption data, Urquhart et al. (2012) place the HII region G340.2480–0.3725 at the near distance. Using recombination line velocities (v_{rrl}) from continuum sources and HI absorptions along the same line of sight, Jones & Dickey (2012) locates the continuum source G341.211–0.233 ($v_{rrl} = -39 \text{ kms}^{-1}$) and G340.278–0.200 ($v_{rrl} = -43 \text{ kms}^{-1}$) associated to the cloud at the near distance. Putting this cloud at the far distance implies an unrealistic physical radius of 221 pc, displacing the cloud far away of the observational size-to-linewidth relationship ($\Delta v(FWHM) = 12.3 \text{ kms}^{-1}$).

- 66: Based on $^{13}\text{CO}(1-0)$ and H I absorption data, Busfield et al. (2006) locates three MYSOs G339.6221–00.1209 (-93.5 kms^{-1}), G339.8712–00.6701 (-91.89 kms^{-1}), and G340.5454–00.3754 (-90.3 kms^{-1}) at the far distance. Given the velocity dispersion of the cloud ($\Delta v(FWHM) = 5.8 \text{ kms}^{-1}$), putting the cloud at the near distance yields a physical radius ($\sim 69 \text{ pc}$) by far more consistent with the observational size-to-linewidth relationship (*first Larson’s Law*) than the physical radius estimated from the far distance ($\sim 127 \text{ pc}$). The location of the cloud in the longitude-velocity diagram does not allow to distinguish between far and near distances mainly because of the position of the “far distance” clouds of the *3-kpc expanding* arm. Although the continuity of the near side of the *Norma* spiral arm suggests the near distance to the cloud, it cannot be ruled out that the cloud actually belongs to the far side of the *3-kpc*

expanding arm. Since the near and far sides of the *3-kpc expanding* arm are separated by more than 100 km s^{-1} (Dame & Thaddeus 2008), some clouds at the far distance are expected to cross the *Norma* and *Centaurus* spiral arms along the radial velocity axis above Galactic longitude $l = 337^\circ$ (tangent point). We adopt the near distance to this cloud, but given the contradictory evidence, the far distance can not be ruled out.

- 67: The HII region G340.777–1.008 is associated to the optical object RCW110 (G340.79–1.01) (Caswell & Haynes 1987; Shaver & Goss 1970). Using recombination line velocities (v_{rrl}) from continuum sources and HI absorptions along the same line of sight, Jones & Dickey (2012) locates the continuum source G340.789–1.022 ($v_{rrl} = -25 \text{ km s}^{-1}$) associated to the cloud at the near distance. The cloud is located far off the Galactic plane at $b = -1^\circ.000$. Putting this cloud at the far distance implies a distance off the plane of 232 pc toward negative latitudes. Bronfman et al. (1988b) estimated the distribution of the molecular layer for the southern Galaxy. At the galactocentric radius of this cloud ($R_{gal} = 6.0 \text{ kpc}$), the molecular ring centroid lies at $z = -13 \text{ pc}$, with a half width half maximum extension of $\sim 53 \text{ pc}$. Following the molecular gas distribution, a far distance to this cloud results unlikely. Therefore, we adopt the near distance in this case.
- 68: The observational size-to-linewidth relationship suggests the near distance because it improves the place of the cloud in the general trend of the relationship. Also the continuity on the near side of the *Norma* spiral arm also suggests the near distance. We locate this cloud at the near distance.
- 69: In the case of this cloud, none of the previous methods could distinguish between

near and far distance, and therefore, no distance was assigned to the cloud.

- 72: In Busfield et al. (2006), the authors identified three MYSOs G342.2263–00.3801 (-25.9 kms^{-1}), G342.3877+00.0742 (-25.9 kms^{-1}), and G342.3891–00.0723 (-21.5 kms^{-1}) to be at the near distance. These three sources coincide in space and radial velocity ($V_{lsr} = -26.6 \text{ kms}^{-1}$) with this cloud. Given the velocity dispersion of the cloud ($\Delta v(FWHM) = 5.4 \text{ kms}^{-1}$), putting it at the near distance yields a physical radius ($\sim 30 \text{ pc}$) by far more consistent with the observational size-to-linewidth relationship (*first Larson’s Law*) than the physical radius estimated from the far distance ($\sim 152 \text{ pc}$). The 6.7 GHz methanol maser 342.446–0.072 is associated to this cloud. The removal of its distance ambiguity done by Green & McClure-Griffiths (2011) confirms our distance determination for its parent GMC.
- 73: Using recombination line velocities (v_{rrl}) from continuum sources and HI absorptions along the same line of sight, Jones & Dickey (2012) locates the continuum source G342.255+0.300 ($v_{rrl} = -122 \text{ kms}^{-1}$) at the tangent point. This would put the cloud at the tangent point. However, their adopted velocity range (25 kms^{-1}) toward the terminal velocity to assign a source to the tangent point is larger than the one we use in this work (10 kms^{-1}). We stick to our limit and, following the discussions for clouds 62, 64, 70, 71, 77, 83, 84, 89, and 91 at the end of the appendix, adopt the near distance to the cloud. The 6.7 GHz methanol maser 342.251+0.308 is associated to this cloud. Using the HI self-absorption method, Green & McClure-Griffiths (2011) put the source at the far distance. This contradicts our determination of the distance to this GMC. The cloud is clearly associated to the near side of the *3-kpc expanding* arm in the longitude-velocity diagram. Since it is known that the arm is expanding,

the assumption that presence/absence of a HI self-absorption feature at the same LSR velocity would removed the distance ambiguity (near or far) of the masers at this Galacocentric radius is not clear. Given the LSR expansion velocity of both arm sides (near and far), by definition, there is no material at the same LSR velocity to compare with. Hence, there will be always an absence of HI self-absorption that will put the masers artificially at the far distance. Also, the invariant manifolds models of Romero-Gómez et al. (2011b) reproduce very well the near side of the *3-kpc expanding* arm in the longitude-velocity diagram, region that coincides with the position of this GMC.

- 74: Based on $^{13}\text{CO}(1-0)$ and HI absorption data, Busfield et al. (2006) assigned the far distance to the IRAS/CS source G342.954–0.311 associated with this cloud. Since the HI data present no absorption at the $^{13}\text{CO}(1-0)$ radial velocity of source, its location at the far distance is almost certain.
- 75: In the case of this cloud, none of the previous methods could distinguish between near and far distance, and therefore, no distance was assigned to the cloud.
- 76: Based on $^{13}\text{CO}(1-0)$ and HI data, Busfield et al. (2006) locate the MYSO G342.3877+00.0742 (-77.5 km s^{-1}) at the near distance, but the HI absorption feature used to discriminate between near or far distance is less prominent than the 20% of the surrounding continuum emission, making the determination of the distance dubious according to the author. Locating this cloud at the far distance yields a large physical radius of $\sim 170 \text{ pc}$. We also notice that clouds at distances further than 4 kpc usually subtend angular scales smaller than 1° (Green et al. 2011) while

the angular size of the cloud in Galactic longitude is larger than 2° and in Galactic latitude it is larger than 1° . The observational size-to-linewidth relationship suggests the near distance because it improves the place of the cloud in the general trend of the relationship as well as the continuity of the near side of the *Norma* spiral arm. On the other hand, the same authors place three MYSOs G342.3877+00.0742 (-84.8 kms^{-1}), G342.3891–00.0723 (-85.5 kms^{-1}), and G342.8089–00.3825 (-80.6 kms^{-1}) at the far distance. The MYSOs coincide in position and radial velocity with the GMC, suggesting the far distance to the cloud. If we adopted the far distance to this cloud, it would become the most massive GMC in our catalog, with a molecular mass of $M(H_2) = 8.7 \times 10^6 M_\odot$, the same as GMC G337.750+0.000 at the far side of the *Norma* spiral arm. Nonetheless, its FIR Luminosity would be very low around $L_{FIR} = 2.7 \times 10^5 L_\odot$, which is only 4% of the FIR luminosity of the *Norma* GMC. This would yield an extremely massive GMC with almost no massive star formation activity while clouds of the same order of molecular mass in our catalog are very active in forming massive stars. This difference is counterintuitive with what we know from GMCs. We believe, it is unlikely that such a massive GMC could have almost no UC H II regions tracing its massive star formation activity, as it is the case for the *Norma* clouds, and therefore we favor the near distance assignment to this cloud. The 6.7 GHz methanol maser 341.367+0.336 is apparently associated to this cloud. The removal of its distance ambiguity done by Green & McClure-Griffiths (2011) seems to contradict our distance determination for the GMC. Nonetheless, there is an explanation for this. The maser is very close to a local maximum, far from the bulk of the integrated CO emission in the GMC’s spatial map. The local maximum can be attributed to a less massive cloud at the far distance (if the distance determination of the associated maser is right) whose CO emission overlaps in phase space with the CO emission of the GMC at the near distance. Since we are sensitive to only the

most massive GMCs at the far distance, this is to be expected in some cases. In this sense, there is no contradiction with our determination of the GMC distance, because the maser is associated to a different and less massive cloud at the far distance that we can not properly isolate with the ASM subtraction technique applied in this work.

- 78: The HII region G343.150–0.402 presents H₂CO absorption at -23 kms^{-1} and recombination line emission at -33 kms^{-1} (Caswell & Haynes 1987). The lack of absorption features between the recombination and terminal velocities locates the source almost certainly at the near distance. The absorption feature at -23 kms^{-1} coincides with the CO velocity dispersion of the cloud ($V_{lsr} = -26.0 \text{ kms}^{-1}$, $\Delta v(FWHM) = 10.0 \text{ kms}^{-1}$), locating the cloud in front of the HII region at the near distance. The 6.7 GHz methanol maser 343.756–0.163 is associated to this cloud. The removal of its distance ambiguity done by Green & McClure-Griffiths (2011) confirms our distance determination for its parent GMC.

- 79: The HII region G344.439+0.048 associated to this cloud presents H₂CO absorption at -65 kms^{-1} and -62 kms^{-1} and recombination line emission at -67 kms^{-1} . The absence of absorption features toward the terminal velocity locates the cloud at the near distance (Caswell & Haynes 1987). Based on HI absorption data, Urquhart et al. (2012) place the HII regions G344.3976+0.0533 and G344.4257+0.0451 at the near distance.

- 80: The HII region G346.206–0.071 located at the near distance lies in front of this cloud and presents no absorption features within the velocity range of the cloud

implying that the cloud has to be located behind the HII region, at the far distance (see discussion for cloud 73). Nonetheless, putting this cloud at the near distance is more in agreement with the general trend of the observational size-to-linewidth relationship. We adopt the far distance to this cloud, but keeping in mind that the near distance can not be completely discarded.

- 81: Given the velocity dispersion of the cloud ($\Delta v(FWHM) = 4.3 \text{ kms}^{-1}$), putting the cloud at the near distance yields a physical radius ($\sim 32 \text{ pc}$) much more consistent with the observational size-to-linewidth relationship (*first Larson's Law*) than the physical radius estimated from the far distance ($\sim 68 \text{ pc}$). Therefore, the near distance is assigned to the cloud.
- 82: We based our determination of far distance to this cloud by inspection of the $^{12}\text{CO}(1-0)$ latitude-velocity maps in Bronfman et al. (1989). Although the extension in velocity of the cloud is small, it still presents an elongated structure similar to those “far” clouds with better determination of their distance ambiguity. The ratio between virial and molecular mass at the near (~ 2.3) and the far (~ 1.3) distance give a very weak indication that the cloud could be placed at the far distance. It is interesting to note that, assuming that the distances for clouds 82, 88, and 92 are correct, there seems to be a lane of clouds between $l = 345^\circ - 348^\circ$, and $v = -95 \text{ kms}^{-1} - -60 \text{ kms}^{-1}$ located at the far distance, possible tracing the far side of the *3-kpc expanding* arm.
- 85: The IRAS/CS source G345.400–0.941 is associated to the optical object RCW117 (G345.50–1.00) (Caswell & Haynes 1987; Turner 1979). Caswell et al. (1975) and Radhakrishnan et al. (1972) present the HI spectrum showing absorption extending

to -34 km s^{-1} . There is a peak of emission at -100 km s^{-1} in the spectrum of both references which confirms the near distance. Shaver et al. (1982) and Bash & Leisawitz (1985) discuss this source in the context of explaining anomalous motions of HI clouds. Bash & Leisawitz (1985) places the source at 4.7 kpc which corresponds to the near distance.

- 86: The HII regions G345.031+1.540, G345.231+1.035, G345.308+1.471, and G345.404+1.406 associated to the cloud posses visual optical counterparts (Wilson et al. 1970; Caswell & Haynes 1987) locating them at the near distance. The IRAS/CS source G345.208+1.028 and G345.393+1.399 are associated with the supernova remnant CTB 35 (part of RCW116) and RCW116 (G345.00+1.70), respectively (Caswell et al. 1975; Georgelin & Georgelin 1976; Whiteoak & Gardner 1974; Turner 1970). According to the evidence, the near distance to the cloud is almost certain.
- 87: The HII region G346.206–0.071 presents no absorption features but recombination line emission at -108 km s^{-1} (Caswell & Haynes 1987). Since the CO terminal velocity is -171 km s^{-1} at the line of sight $l = 346^\circ$ (Alvarez et al. 1990), it is unlikely that, being this cloud at the far distance ($\sim 11.2 \text{ kpc}$), presents no absorption features across the Galactic plane, favoring the near distance for this source. Putting this cloud at the far distance yields a physical radius $\sim 96 \text{ pc}$ and displaces the position of the cloud from the general trend in the observational *first Larson’s law* ($\Delta v(FWHM) = 7.7 \text{ km s}^{-1}$). We adopt the near distance to this cloud.
- 88: The HII region G346.206–0.071 presents no H_2CO absorption features but

recombination line emission at -108 kms^{-1} favoring the far distance. Also, given the large velocity dispersion of the cloud ($\Delta v(FWHM) = 13.9 \text{ kms}^{-1}$), putting the cloud at the far distance yields a physical radius ($\sim 90 \text{ pc}$) much more consistent with the observational size-to-linewidth relationship (*first Larson's Law*) than the physical radius estimated from the near distance ($\sim 47 \text{ pc}$). We also notice that, in general, clouds at the far distance tend to have a small solid angle and small Galactic latitude (because of the distance projection) but still, if the cloud is massive, a large velocity dispersion ($\Delta v(FWHM) \sim 10 \text{ kms}^{-1}$). The elongated structure in radial velocity of this cloud is very similar to those “far” clouds with better determination of their distance ambiguity. We adopt the far distance to the cloud.

- 90: On the one hand, given the velocity dispersion of the cloud ($\Delta v(FWHM) = 7.4 \text{ kms}^{-1}$), putting the cloud at the near distance yields a physical radius ($\sim 50 \text{ pc}$) much more consistent with the observational size-to-linewidth relationship (*first Larson's Law*) than the physical radius estimated from the far distance ($\sim 118 \text{ pc}$). On the other hand, putting the cloud at the far distance implies a distance off the plane of 202 pc toward positive latitudes. Bronfman et al. (1988b) estimated the distribution of the molecular layer for the southern Galaxy. At the galactocentric radius of this cloud ($R_{gal} = 3.9 \text{ kpc}$), the molecular ring centroid lies at $z = 2 \text{ pc}$, with a half width half maximum extension of $\sim 83 \text{ pc}$. Following the molecular gas distribution, a far distance to this cloud results unlikely. Therefore, we adopt the near distance in this case.
- 92: The HII region G347.386+0.266 presents no H_2CO absorption features but recombination line emission at -97 kms^{-1} . Given the terminal velocity at the

line of sight of this source ($\sim -200 \text{ km s}^{-1}$, estimated by simple inspection of the longitude-velocity diagram of the CO emission) and the absence of absorption features, we locate the HII region at the near distance. Since the HII region coincides with position of the cloud on the sky, the absence of absorption features suggests the far distance to the cloud. We notice that, in general, clouds at the far distance tend to have a small solid angle and small Galactic latitude (because of the distance projection) but still, if the cloud is massive, a large velocity dispersion ($\Delta v(FWHM) \sim 10 \text{ km s}^{-1}$). The elongated structure in radial velocity of this cloud is very similar to those “far” clouds with better determination of their distance ambiguity. We adopt the far distance to the cloud.

- GMCs belonging to the *3-kpc expanding arm*: 62, 64, 70, 71, 77, 83, 84, 89, and 91: In order to distinguish between far and near distances for these clouds, we take advantage of the well known $\sim -53 \text{ km s}^{-1}$ expansion velocity of the *3-kpc expanding* spiral arm. The position of these clouds in the longitude-velocity diagram clearly corresponds to the location of the arm in the fourth Galactic quadrant as it has been traced by the 21 cm line observations in previous surveys (Rougeer & Oort 1960). Dame & Thaddeus (2008) traced, for the first time, the far side of the spiral arm between Galactic longitudes $l = 13^\circ$ and $l = -12^\circ$. The far side of the arm presents also an expanding velocity of $+56 \text{ km s}^{-1}$ being remarkably similar to its near counterpart, and indicating a more than 100 km s^{-1} separation between the near and far sides of the arm, at least, in the range of Galactic longitudes covered in their work. The emission from both sides of the arm behaves as parallel lanes of emission across Galactic longitude. Dame & Thaddeus (2008) fit this emission radial velocity to be a function of Galactic longitude yielding $v = -53.1 + 4.16l$ for the near side and, $v = 56 + 4.08l$ for the far side. Concerning the near side fit, we note that it agrees extremely well with the

position of these clouds in our catalog tracing this arm up to $l = 342^\circ.375$. At smaller longitudes, the position of the clouds in phase space deviates from this trend. Due to the good spatial and velocity correspondence between the near side of the *3-kpc expanding* arm and the clouds 62, 64, 70, 77, 83, 84, 89, and 91 in our catalog, we are confident in our location of these clouds at the near distance. In the case of cloud 64, the 6.7 GHz methanol maser $340.118-0.021$, $340.182-0.047$, and $340.249-0.04$ are associated to it. Using the HI self-absorption method, Green & McClure-Griffiths (2011) put the masers at the far distance. This contradicts our determination of the distance to this GMC. The cloud is clearly associated to the near side of the *3-kpc expanding* arm in the longitude-velocity diagram. Since it is known that the arm is expanding, the assumption that presence/absence of a HI self-absorption feature at the same LSR velocity would removed the distance ambiguity (near or far) of the masers at this Galacocentric radius is not clear. Given the LSR expansion velocity of both arm sides (near and far), by definition, there is no material at the same LSR velocity to compare with. Hence, there will be always an absence of HI self-absorption that will put the masers artificially at the far distance. Also, the invariant manifolds models of Romero-Gómez et al. (2011b) reproduce very well the near side of the *3-kpc expanding* arm in the longitude-velocity diagram, region that coincides with the position of this GMC.

REFERENCES

- Allen, C. W. 1973, *Astrophysical Quantities* (3rd ed.; London: Athlone)
- Alvarez, H., May, J., & Bronfman, L. 1990, *ApJ*, 348, 495
- Bash, F. N., & Leisawitz, D. 1985, *A&A*, 145, 127
- Bertoldi, F., & McKee, C. F. 1992, *ApJ*, 395, 140
- Beuther, H., Tackenberg, J., Linz, H., et al. 2012, *ApJ*, 747, 43
- Blitz, L., Fukui, Y., Kawamura, A., et al. 2007, 2007prpl conf, 81
- Blitz, L., & Rosolowsky, E. 2004, *ArXiv Astrophysics e-prints*, arXiv:astro-ph/0411520
- Brand, J., & Blitz, L. 1993, *A&A*, 275, 67
- Bronfman, A. L. 1986, Ph.D. Thesis, Columbia University, New York.
- Bronfman, L. 1992, in *The center, bulge and disk of the Milky Way*, ed. L. Blitz, p. 131
- Bronfman, L., Alvarez, H., Cohen, R. S., & Thaddeus, P. 1989, *ApJS*, 71, 481
- Bronfman, L., Bitran, M., & Thaddeus, P. 1988a, *LNP*, 315, 318
- Bronfman, L., Casassus, S., May, J., & Nyman, L.-Å. 2000, *A&A*, 358, 521
- Bronfman, L., Cohen, R. S., Alvarez, H., May, J., & Thaddeus, P. 1988b, *ApJ*, 324, 248
- Bronfman, L., Garay, G., Merello, M., et al. 2008, *R. 2008, ApJ*, 672, 391
- Bronfman, L., Nyman, L.-A., & May, J. 1996, *A&AS*, 115, 81
- Burton, W. B. 1971, *A&A*, 10, 76

- Burton, W. B. 1988, *Galactic and ExtraGalactic Radio Astronomy* (2nd ed., eds. G.L. Verschuur & K. Kellerman; New York:Springer)
- Busfield, A. L., Purcell, C. R., Hoare, M. G., et al. 2006, *MNRAS*, 366, 1096
- Casoli, F., Combes, F., & Gerin, M. 1984, *A&A*, 133, 99
- Caswell, J. L. 2003, *MNRAS*, 341, 551
- Caswell, J. L., & Haynes, R. F. 1975, *MNRAS*, 173, 649
- Caswell, J. L., & Haynes, R. F. 1987, *A&A*, 171, 261
- Caswell, J. L., Murray, J. D., Roger, R. S., Cole, D. J., & Cooke, D. J. 1975, *A&A*, 45, 239
- Caswell, J. L., & Reynolds, J. E. 2001, *MNRAS*, 325, 1346
- Caswell, J. L., & Robinson, B. J. 1974, *AuJPh*, 27, 597
- Churchwell, E., Mezger, P. G., & Huchtmeier, W. 1974, *A&A*, 32, 283
- Cohen, R. J., & Davies, R. D. 1976, *MNRAS*, 175, 1
- Combes, F. 1991, *ARA&A*, 29, 195
- Dame, T. M. 1983, Ph.D. Thesis, Columbia University, New York.
- Dame, T. M., Elmegreen, B. G., Cohen, R. S., & Thaddeus, P. 1986, *ApJ*, 305, 892
- Dame, T. M., & Thaddeus, P. 2008, *ApJ*, 683, L143
- Dame, T. M., & Thaddeus, P. 2011, *ApJ*, 734, L24
- Dickman, R. L. 1978, *ApJS*, 37, 407
- Elmegreen, B. G. 1993, *Star Formation, Galaxies and the Interstellar Medium* (J. Franco, F. Ferrini, & G. Tenorio-Tagle ed.; Cambridge:Cambridge Univ. Press)

- Elmegreen, B. G. 1994, *ApJ*, 433, 39
- Englmaier, P., & Gerhard, O. 1999, *MNRAS*, 304, 512
- Evans, N. J., II 1999, *ARA&A*, 37, 311
- Faúndez, S., Bronfman, L., Garay, G., et al. 2004, *A&A*, 426, 97
- Fish, V. L., Reid, M. J., Wilner, D. J., & Churchwell, E. 2003, *ApJ*, 587, 701
- Frerking, M. A., Langer, W. D., & Wilson, R. W. 1982, *ApJ*, 262, 590
- Gardner, F. F., & Whiteoak, J. B. 1984, *MNRAS*, 210, 23
- Georgelin, Y. M., & Georgelin, Y. P. 1976, *A&A*, 49, 57
- Glover, S. C. O., & Mac Low, M.-M. 2011, *MNRAS*, 412, 337
- Goss, W. M., Manchester, R. N., & Robinson, B. J. 1970, *AuJPh*, 23, 559
- Goss, W. M., Radhakrishnan, V., Brooks, J. W., & Murray, J. D. 1972, *ApJS*, 24, 123
- Grabelsky, D. A., Cohen, R. S., Bronfman, L., & Thaddeus, P. 1988, *ApJ*, 331, 181
- Grabelsky, D. A., Cohen, R. S., Bronfman, L., Thaddeus, P., & May, J. 1987, *ApJ*, 315, 122
- Green, J. A., Caswell, J. L., McClure-Griffiths, N. M., et al. 2011, *ApJ*, 733, 27
- Green, J. A., & McClure-Griffiths, N. M. 2011, *MNRAS*, 417, 2500
- Hunter, S. D., Bertsch, D. L., Catelli, J. R., et al. 1997, *ApJ*, 481, 205
- Jones, C., & Dickey, J. M. 2012, *ApJ*, 753, 62
- Kennicutt, R. C., Jr. 1998, *ARA&A*, 36, 189
- Kerr, F. J., & Knapp, G. R. 1970, *AuJPA*, 18, 9

- Kritsuk, A. 2007, KITP Conference: Star Formation, Then and Now:
http://online.kitp.ucsb.edu/online/stars_c07/, article #14
- Krumholz, M. R. 2006, New Horizons in Astronomy: Frank N. Bash Symposium, 352, 31
- Krumholz, M. R., & McKee, C. F. 2005, *ApJ*, 630, 250
- Larson, R. B. 1981, *MNRAS*, 194, 809
- Liszt, H. S. 1995, *ApJ*, 442, 163
- Liszt, H. S., Burton, W. B., & Xiang, D.-L. 1984, *A&A*, 140, 303
- Lockman, F. J. 1979, *ApJ*, 232, 761
- Luna, A., Bronfman, L., Carrasco, L., & May, J. 2006, *ApJ*, 641, 938
- Mac Low, M.-M., & Klessen, R. S. 2004, *RvMP*, 76, 125
- May, J., Alvarez, H., & Bronfman, L. 1997, *A&A*, 327, 325
- McClure-Griffiths, N. M., Green, A. J., Dickey, J. M., et al. 2001, *ApJ*, 551, 394
- McGee, R. X., Gardner, F. F., & Robinson, B. J. 1967, *AuJPh*, 20, 407
- McKee, C. F., & Ostriker, E. C. 2007, *ARA&A*, 45, 565
- Merello, M., Bronfman, L., Garay, G., et al. 2013, *ApJ*, 774, 38
- Myers, P. C., Dame, T. M., Thaddeus, P., et al. 1986, *ApJ*, 301, 398
- Nyman, L.-A., Thaddeus, P., Bronfman, L., & Cohen, R. S. 1987, *ApJ*, 314, 374
- Phillips, C. J., Norris, R. P., Ellingsen, S. P., & McCulloch, P. M. 1998, *MNRAS*, 300, 1131
- Radhakrishnan, V., Goss, W. M., Murray, J. D., & Brooks, J. W. 1972, *ApJS*, 24, 49

- Reid, M. J., Menten, K. M., Brunthaler, A., et al. 2009a, *ApJ*, 693, 397
- Reid, M. J., Menten, K. M., Zheng, X. W., et al. 2009b, *ApJ*, 700, 137
- Robinson, B. J., Caswell, J. L., & Goss, W. M. 1971, *ApL*, 9, 5
- Rodgers, A. W., Campbell, C. T., & Whiteoak, J. B. 1960, *MNRAS*, 121, 103
- Roman-Duval, J., Jackson, J. M., Heyer, M., et al. 2009, *ApJ*, 699, 1153
- Romero-Gómez, M., Athanassoula, E., Antoja, T., & Figueras, F. 2011a, *MNRAS*, 418, 1176
- Romero-Gomez, M., Athanassoula, E., Antoja, T., et al. 2011b, *RevMexAA Conference Series*, 40, 92
- Rosolowsky, E. 2005, *PASP*, 117, 1403
- Rougoor, G. W., & Oort, J. H. 1960, *PNAS*, 46, 1
- Russeil, D. 2003, *A&A*, 397, 133
- Sanna, A., Reid, M. J., Menten, K., & BeSSeL Survey Team 2013, *American Astronomical Society Meeting Abstracts*, 222, #211.02
- Sanders, D. B., Scoville, N. Z., & Solomon, P. M. 1985, *ApJ*, 289, 373
- Schuller, F., Menten, K. M., Wyrowski, F., et al. 2010, *Highlights of Astronomy*, 15, 780
- Scoville, N. Z., Yun, M. S., Sanders, D. B., Clemens, D. P., & Waller, W. H. 1987, *ApJS*, 63, 821
- Shaver, P. A., & Goss, W. M. 1970, *AuJPA*, 14, 133

- Shaver, P. A., McGee, R. X., Newton, L. M., Danks, A. C., & Pottasch, S. R. 1983, MNRAS, 204, 53
- Shaver, P. A., Radhakrishnan, V., Anantharamaiah, K. R., Retallack, D. S., Wamsteker, W., & Danks, A. C. 1982, A&A, 106, 105
- Shaver, P. A., Retallack, D. S., Wamsteker, W., & Danks, A. C. 1981, A&A, 102, 225
- Shetty, R., Glover, S. C., Dullemond, C. P., & Klessen, R. S. 2011, MNRAS, 412, 1686
- Solomon, P. M., & Rivolo, A. R. 1989, ApJ, 339, 919
- Solomon, P. M., Rivolo, A. R., Barrett, J., & Yahil, A. 1987, ApJ, 319, 730
- Tan, J. C. 2005, ArXiv Astrophysics e-prints, arXiv:astro-ph/0504256
- Tan, J. C., Shaske, S. N., & Van Loo, S. 2013, IAU Symposium, 292, 19
- Tanti, K. K., Roy, J., & Duorah, K. 2012, Advances in Astronomy and Space Physics, 2, #.1.39
- Turner, B. E. 1970, ApL, 6, 99
- Turner, B. E. 1979, A&AS, 37, 1
- Ungerechts, H., Umbanhowar, P., & Thaddeus, P. 2000, ApJ, 537, 221
- Urquhart, J. S., Hoare, M. G., Lumsden, S. L., et al. 2012, MNRAS, 420, 1656
- Walsh, A. J., Hyland, A. R., Robinson, G., & Burton, M. G. 1997, MNRAS, 291, 261
- Walsh, A. J., Lee, J.-K., & Burton, M. G. 2002, MNRAS, 329, 475
- Whiteoak, J. B., & Gardner, F. F. 1970, ApL, 5, 5
- Whiteoak, J. B., & Gardner, F. F. 1974, A&A, 37, 389

Williams, J. P., & McKee, C. F. 1997, *ApJ*, 476, 166

Wilson, T. L., Mezger, P. G., Gardner, F. F., & Milne, D. K. 1970, *A&A*, 6, 364

Wood, D. O. S., & Churchwell, E. 1989, *ApJ*, 340, 265

Zinnecker, H., & Yorke, H. W. 2007, *ARA&A*, 45, 481

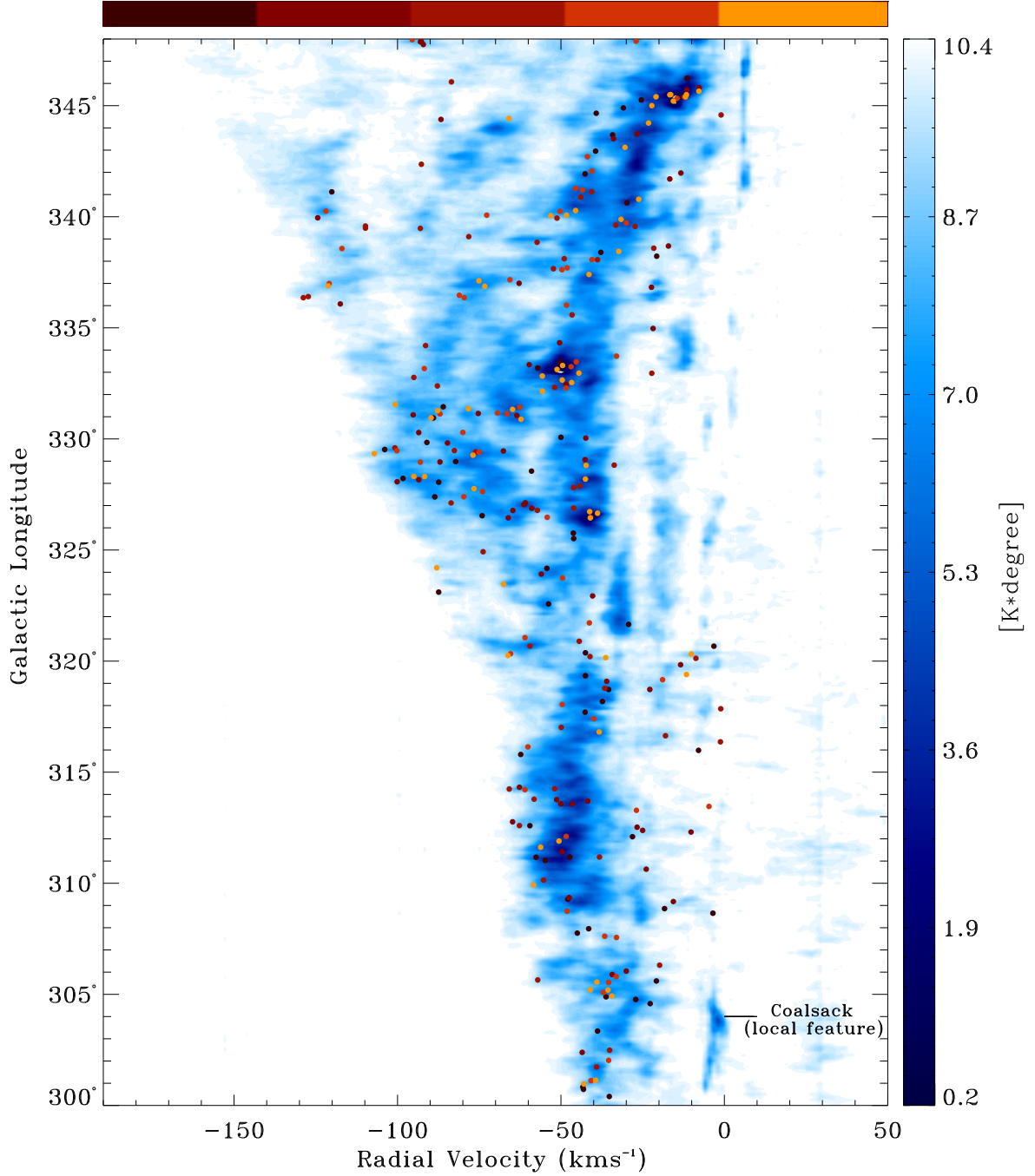


Fig. 1.—: Longitude-velocity diagram of the Columbia Southern CO Survey and IRAS point-like sources with FIR colors of UC HII regions (Wood & Churchwell 1989) (IRAS/CS sources) in the fourth Galactic quadrant. The Longitude-velocity diagram of the CO emission was obtained by integrating the data set over $b = \pm 2.0^\circ$. The bluish color scale denotes values of antenna temperature as $\int T_A db$. A brief summary of the survey parameters is presented in Table 1. For the IRAS/CS sources, the reddish color scale represents the FIR flux (94 - 704 Jy brown; 728 - 1590 Jy dark red; 1629 - 3561 Jy red; 3598 - 8140 Jy orange; and 8160 - 62864 Jy yellow). The kinematic information of the sources was obtained from the most complete current available CS(2-1) survey of IRAS point-like sources with FIR colors characteristic of UC HII regions (Bronfman et al. 1996), complemented by a new CS(2-1) unpublished survey (L. Bronfman et al., in preparation).

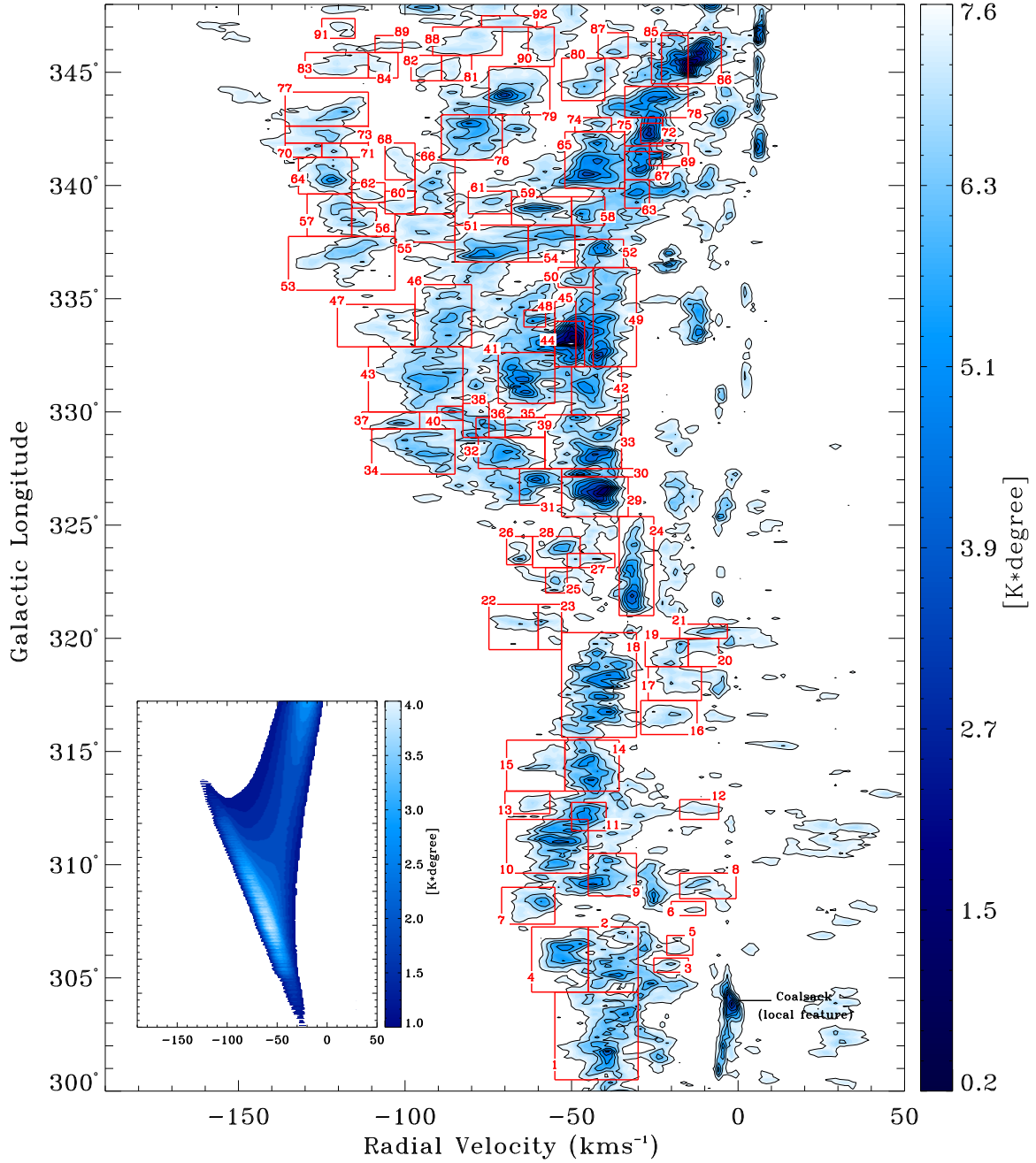


Fig. 2.—: Giant Molecular Clouds in the fourth Galactic quadrant. The longitude-velocity diagram was obtained by integrating the model subtracted CO dataset across the Galactic plane over $b = \pm 2.0^\circ$. The blue color scale denotes values of $\int T_A db$. The first contour is located at 0.25 K degree. The axisymmetric model of the background emission is presented in the insert on the left lower corner of the figure. The model was subtracted from the data in Figure 1 in order to isolate GMCs from their surrounding *background*. The result is shown in the present figure.

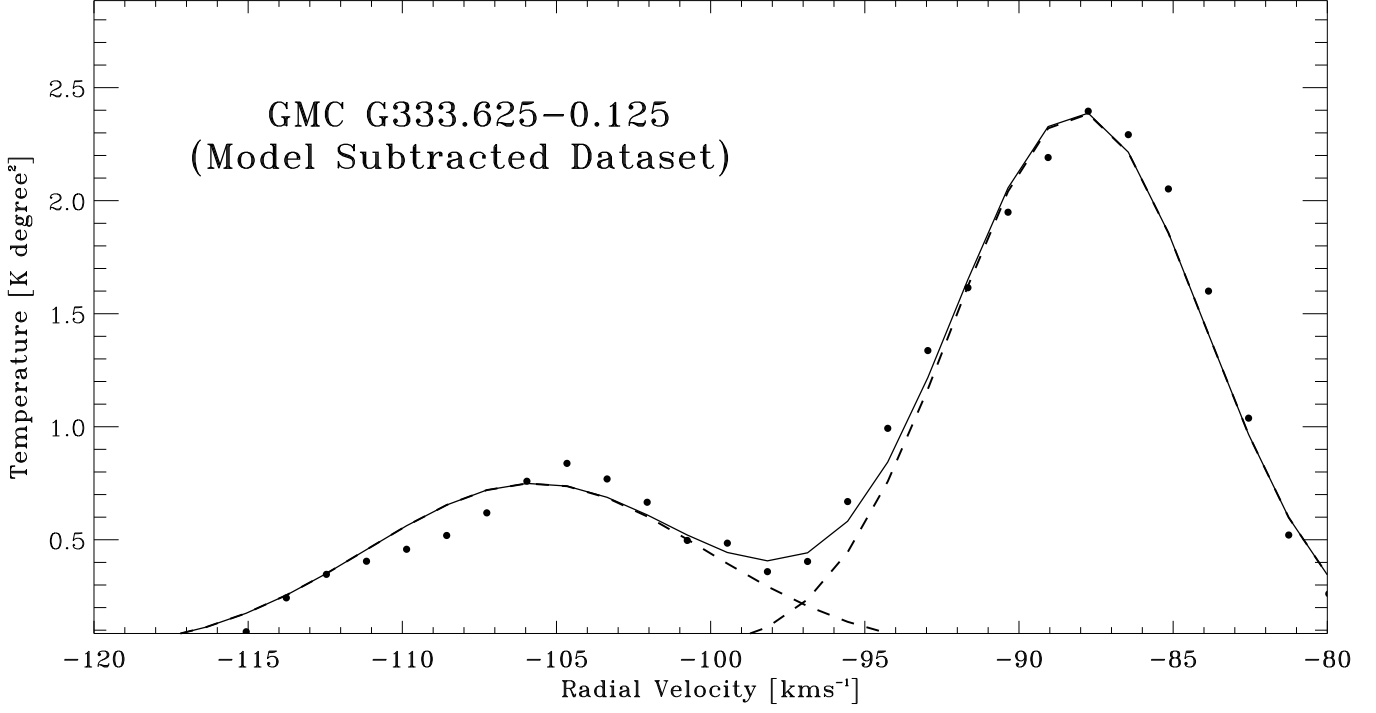


Fig. 3.—: Composite spectrum for GMC G333.625-0.125. Filled circles represent the antenna temperatures in the composite spectrum, after subtraction of the axisymmetric model (ASM) of the CO *background* emission from the original dataset. The solid line shows the results of the two-component Gaussian fit to the composite spectrum. The dashed lines show each individual Gaussian obtained in the fit procedure.

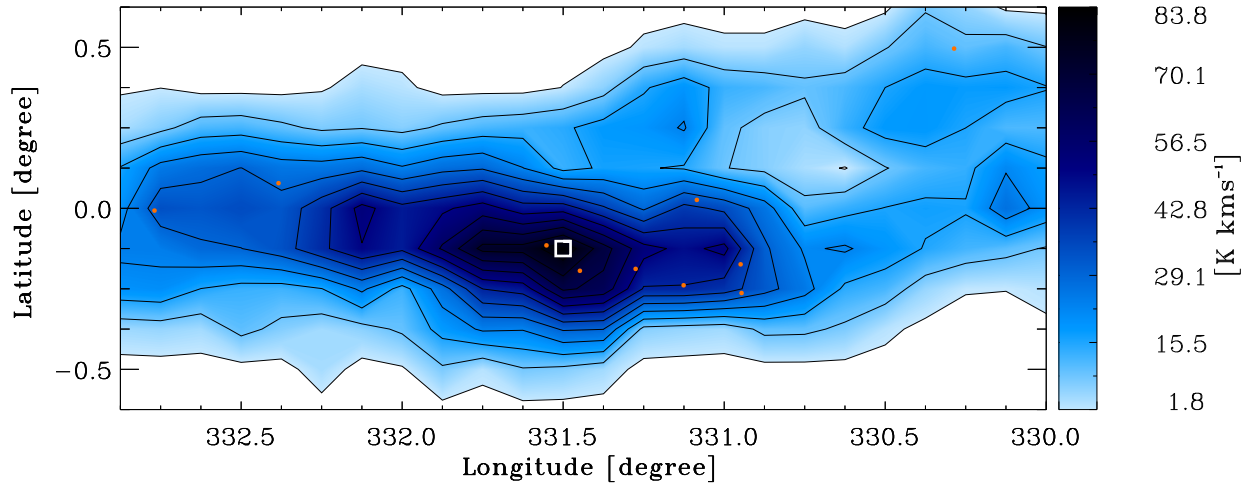


Fig. 4.—: Spatial map for GMC G331.500–0.125. The bluish scale denotes values of CO intensity $\int T_A dv$. Orange dots denote the location of the IRAS/CS sources associated to this cloud in the present work. The white square shows the center of the cloud based on the CO peak intensity. All the intrinsic physical parameters for each cloud are derived from the information contained within the spatial map and composite spectrum of the cloud.

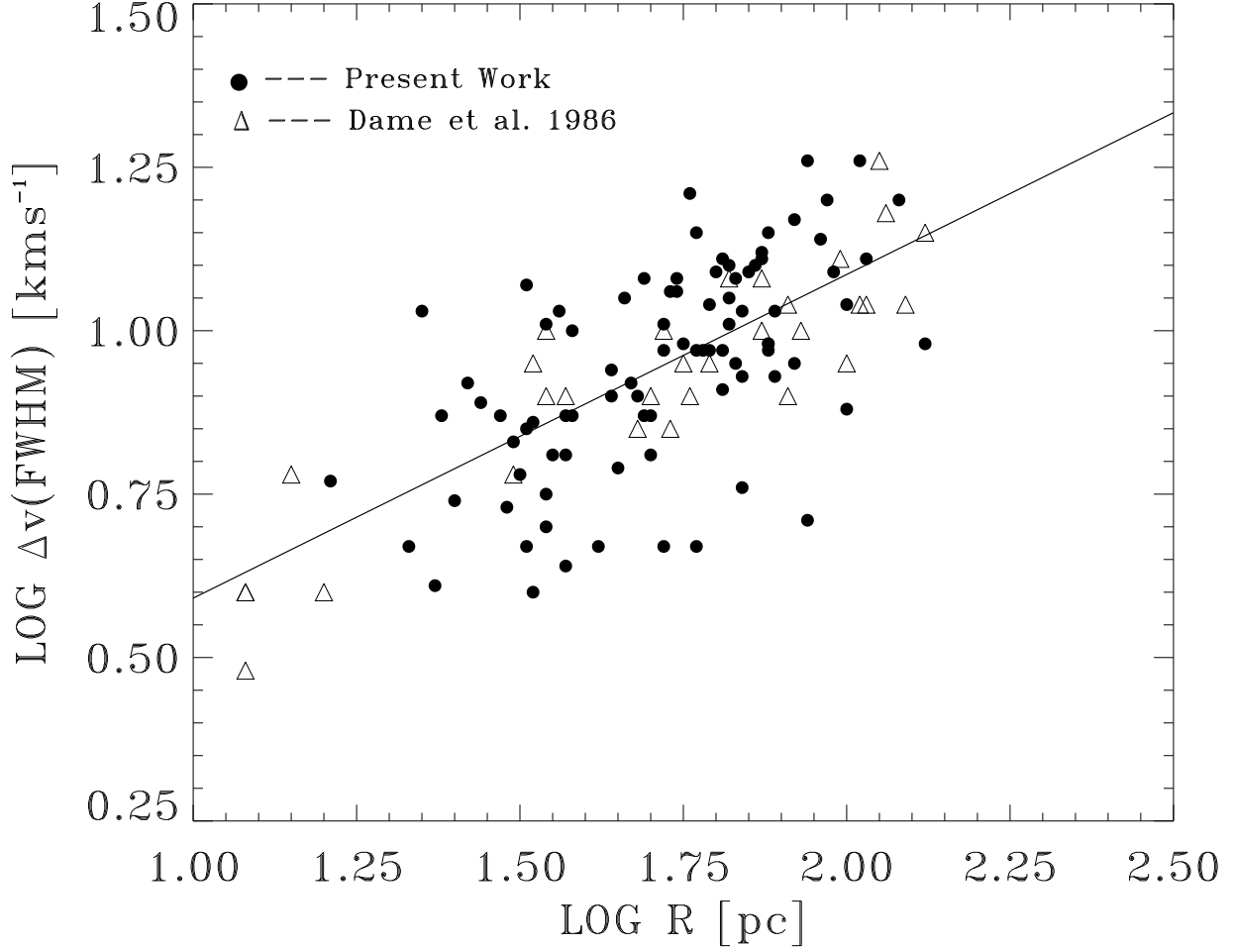


Fig. 5.—: Logarithm of the observed linewidth $\Delta v(FWHM)$ vs. the logarithm of the effective physical radius R of GMCs in Table 2 (filled circles) and for GMCs in the catalog of Dame et al. (1986) (open triangles). The straight line is a least-squares fit to the clouds in our catalog given by the equation $\log \Delta v(FWHM) = 0.10 + 0.50 \log R$.

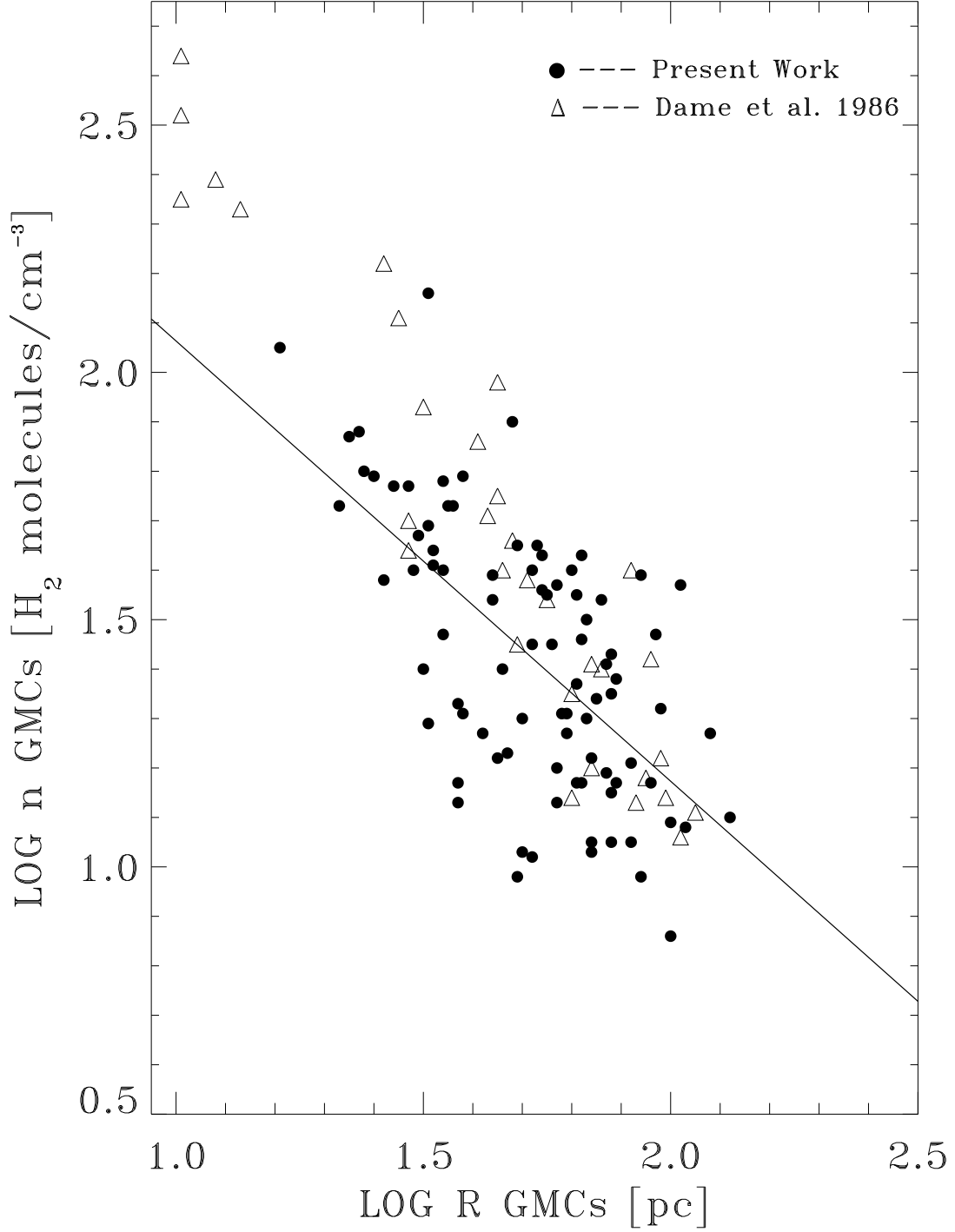


Fig. 6.—: Logarithm of the H_2 volume density corrected for helium $n(\text{H}_2)$ vs. the logarithm of the effective physical radius R for GMCs in Table 2 (filled circles) and for GMCs in the catalog of Dame et al. (1986) (open triangles). The straight line is a least-squares fit given by the equation $\log n(\text{H}_2) = 2.95 - 0.89 \log R$.

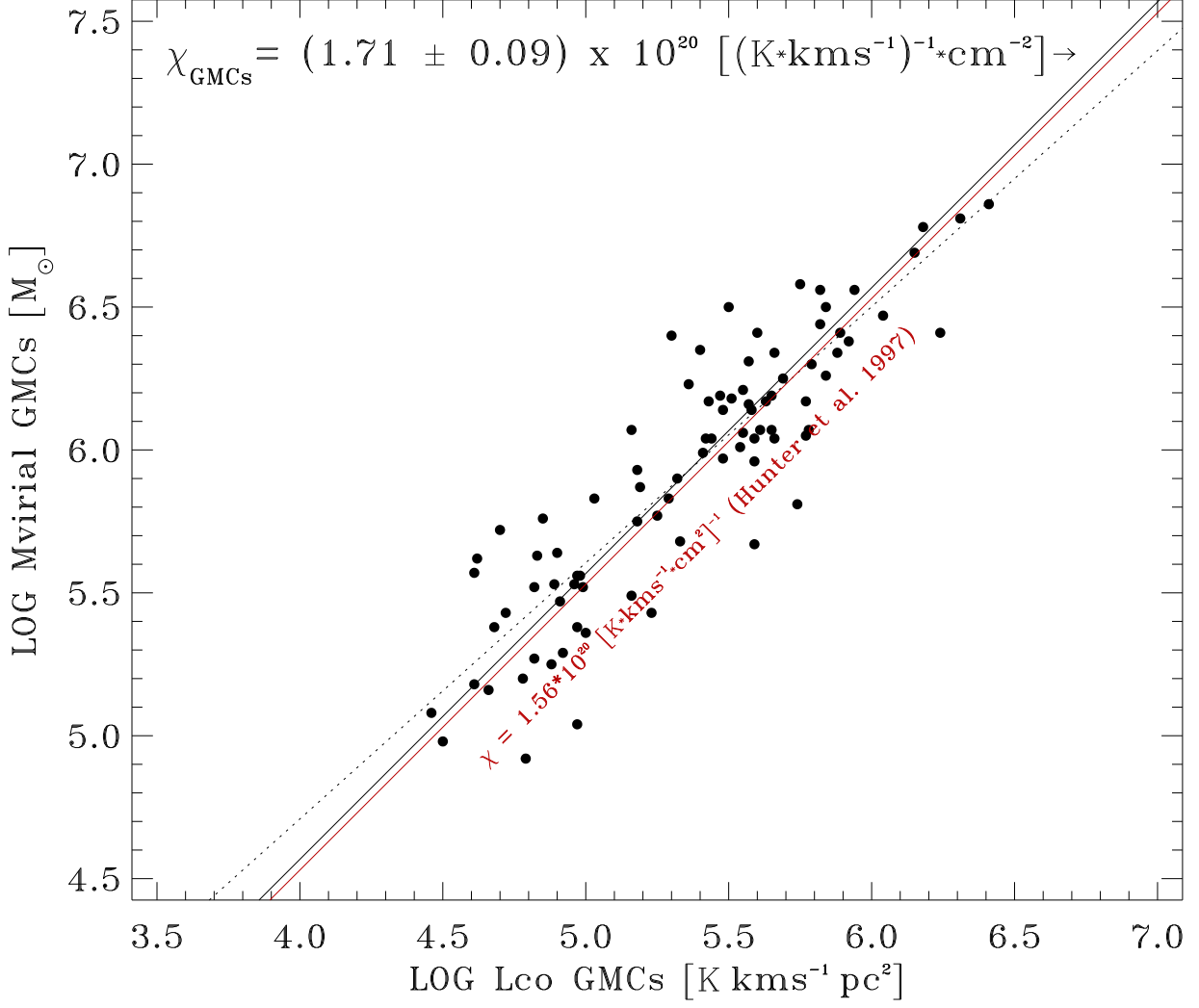


Fig. 7.—: Logarithm of the virial mass vs. the logarithm of the CO luminosity for GMCs in Table 2. The dotted straight line is a least-squares fit given by the equation $\log M_{\text{virial}} = 1.11 + 0.90 \log L_{\text{CO}}$. The solid black straight line is a least-squares fit given by the equation $\log M_{\text{virial}} = 0.57 + \log L_{\text{CO}}$. The red straight line represents the $W(\text{CO})$ -to- $N(\text{H}_2)$ factor utilized in the present work (Hunter et al. 1997).

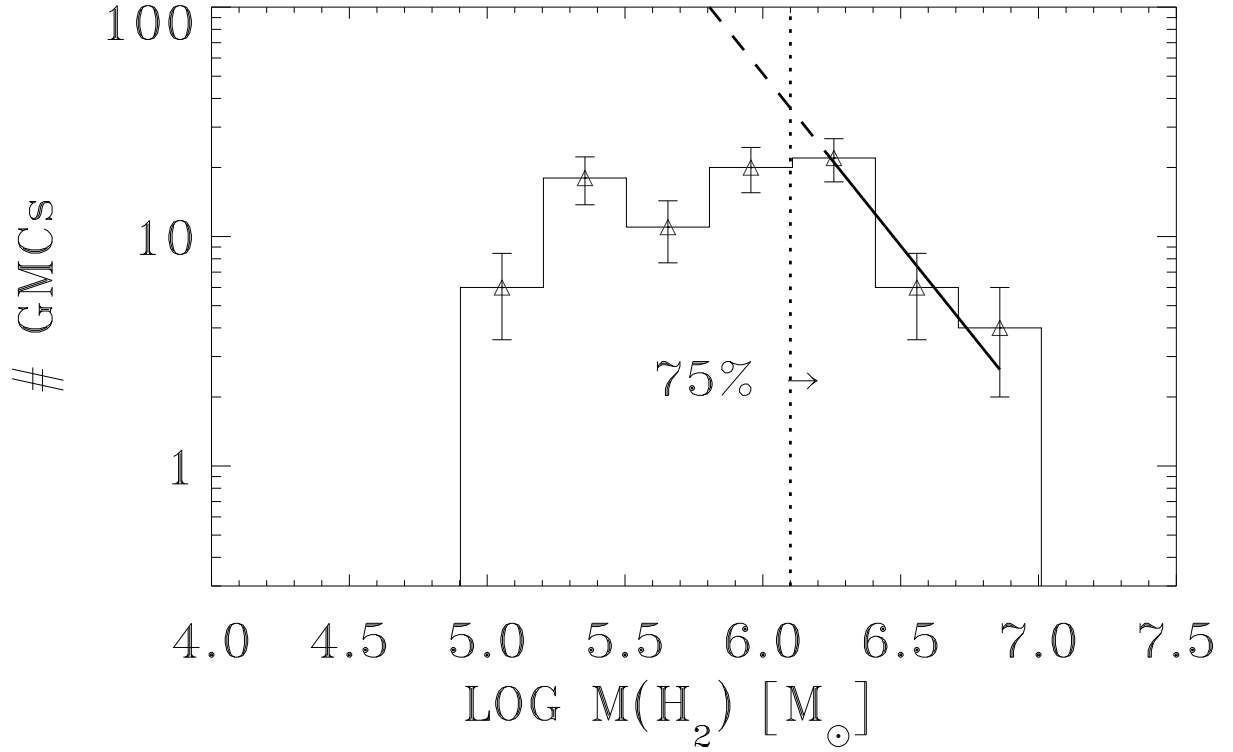


Fig. 8.—: Mass spectrum for GMCs in Table 2. A least-squares fit has been made over the range indicated by the solid line, being the dashed line an extrapolation to the lower mass end of the spectra. The logarithmic mass bin is $\Delta_{log} = 0.3$. Small triangles represent the central mass in each mass bin and the dotted line represents the 75% of the total molecular mass contained to the high mass end of the distribution. The slope of the distribution is $\gamma = 1.50 \pm 0.40$.

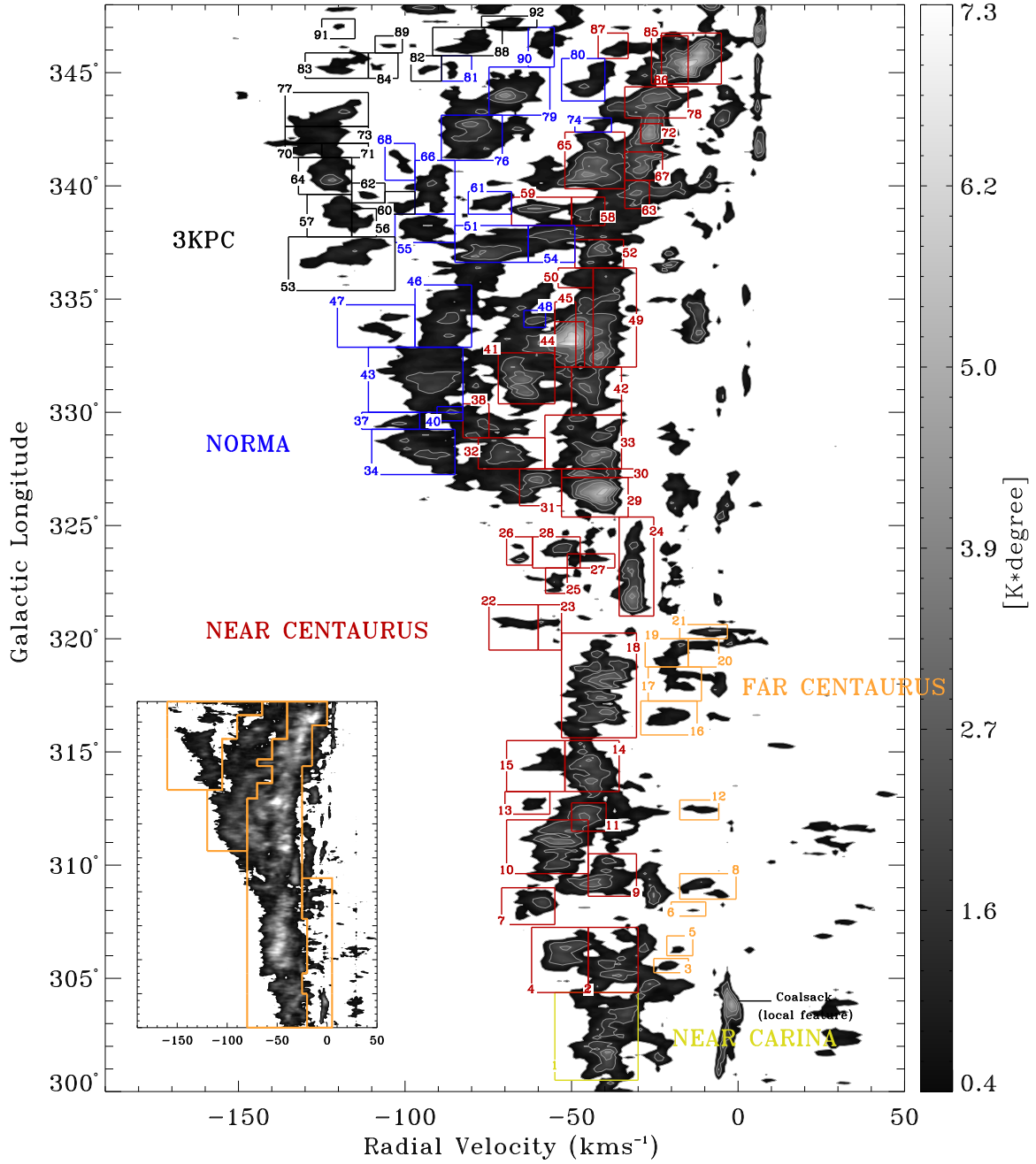


Fig. 9.—: Giant Molecular Clouds in the fourth Galactic quadrant as tracers of the large scale spiral structure in the southern Galaxy. From the plot we identify three spiral arms: *Centaurus* (red clouds tracing the near side and orange clouds tracing the far side); *Norma* (blue clouds tracing the near and far sides of the arm); and *3-kpc expanding arm* (black box clouds tracing near and far sides of the arm). Based on spatial coincidence, we also identify one cloud (yellow box) belonging to the well known *Carina* spiral arm (Grabelsky et al. 1987). Based on the distribution of GMCs in the longitude-velocity diagram, a tentative picture of the limits in CO radial velocity and Galactic longitude of the spiral features is presented in the insert on the left lower corner of the figure. The limits are plotted over the CO data of the Columbia Survey.

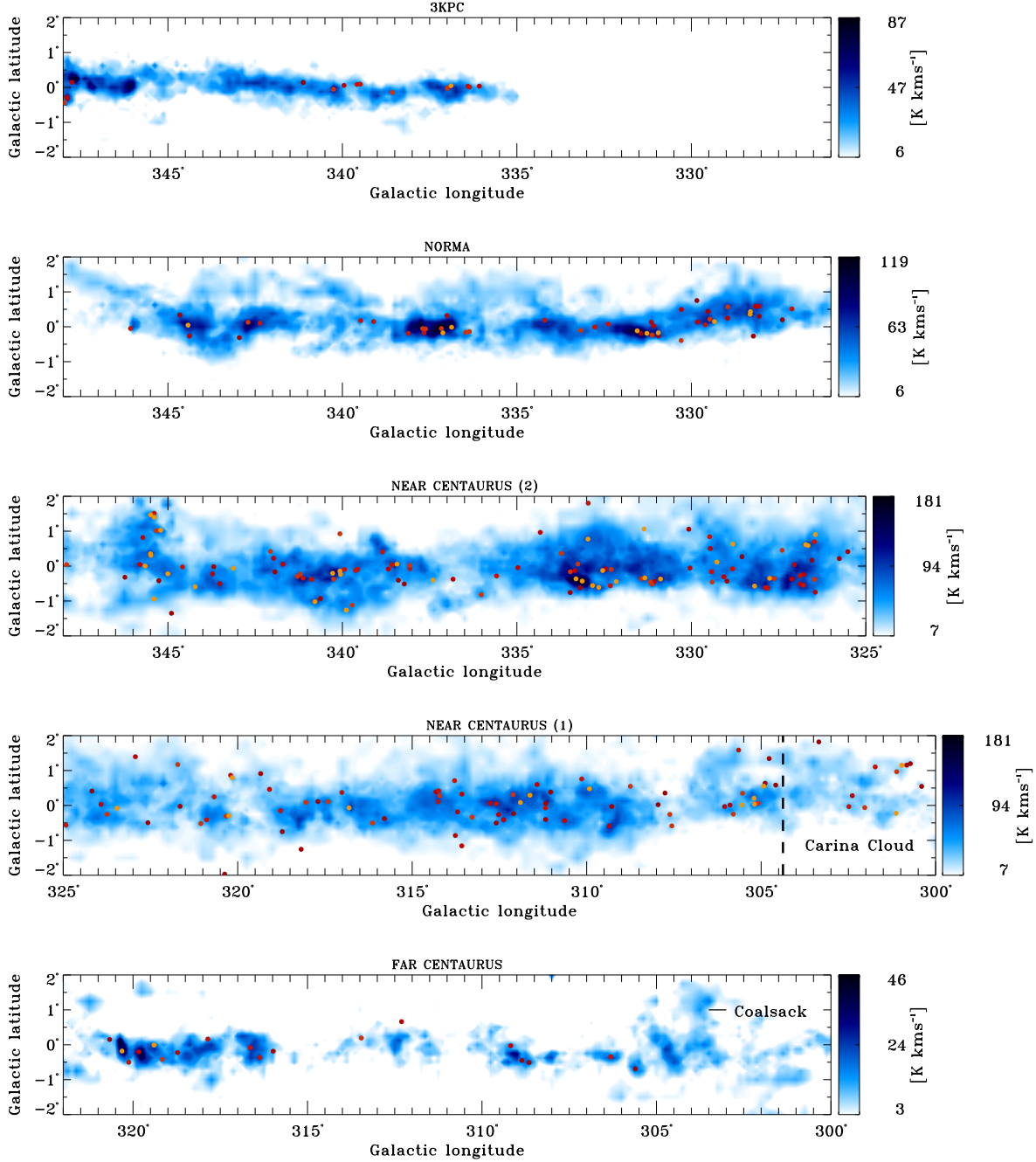


Fig. 10.—: Spatial edge-on maps of the Galactic spiral arms obtained by integrating the CO data of the Columbia Survey across the corresponding velocity range presented in Figure 9 for each arm. Contours denote values of CO intensity $I(l, b) = \int T_A dv$. Each map has its own intensity color scale (except for the two maps showing the near side of the *Centaurus* arm, which share a common color scale), being the lowest intensity at 7σ of the corresponding map, where σ is the characteristic intensity noise of the map. The Spatial distribution of 284 IRAS/CS sources utilized in the present work along the spiral arms is also shown as superimposed filled circles.

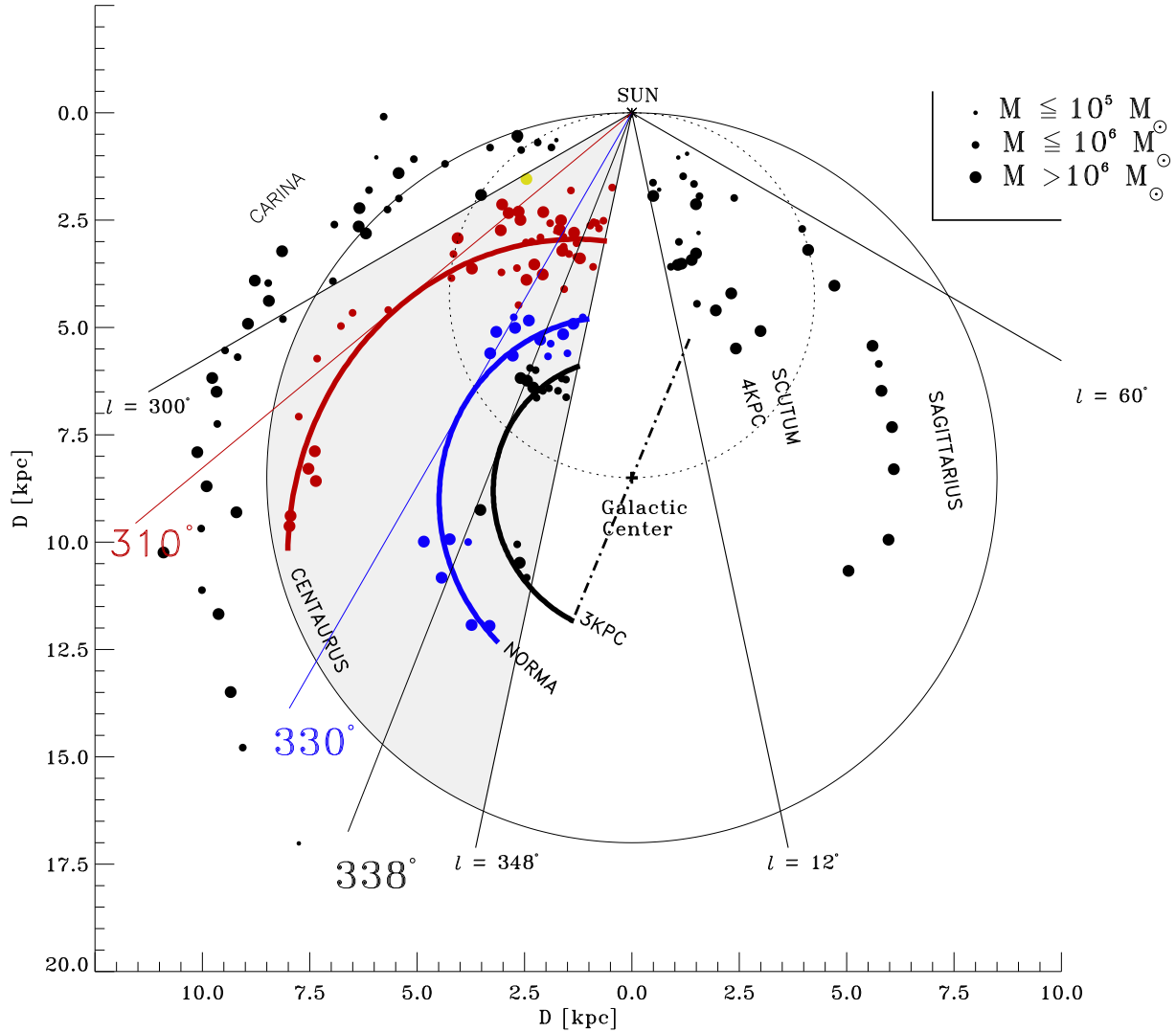


Fig. 11.—: Spatial distribution (face-on view) of giant molecular clouds in the first and fourth Galactic quadrants. In the fourth Galactic quadrant, the 87 molecular complexes from Table 2 are drawn within the covered area in this work (gray filled area between $l = 300^\circ$ and $l = 348^\circ$), and are associated by colors to their corresponding spiral arm, as explained in Figure 9. The size of a circle is related to the molecular mass of the cloud. Toward lower Galactic longitudes, the molecular complexes tracing the *Carina* arm plotted as black filled circles are from Grabelsky et al. (1987). In the first Galactic quadrant, between $l = 12^\circ$ and $l = 60^\circ$, the molecular complexes plotted as filled black circles are from Dame et al. (1986). The dotted large circle represents the tangent region within the solar circle, and the dashed-dotted straight line represents the position of the Galactic bar taken from Englmaier & Gerhard (1999). The parameters for the three fitted spiral arms (seen as thick color lines) in our catalog are summarized in Table 3. The fit was done weighting each point by its Galactocentric radius error.

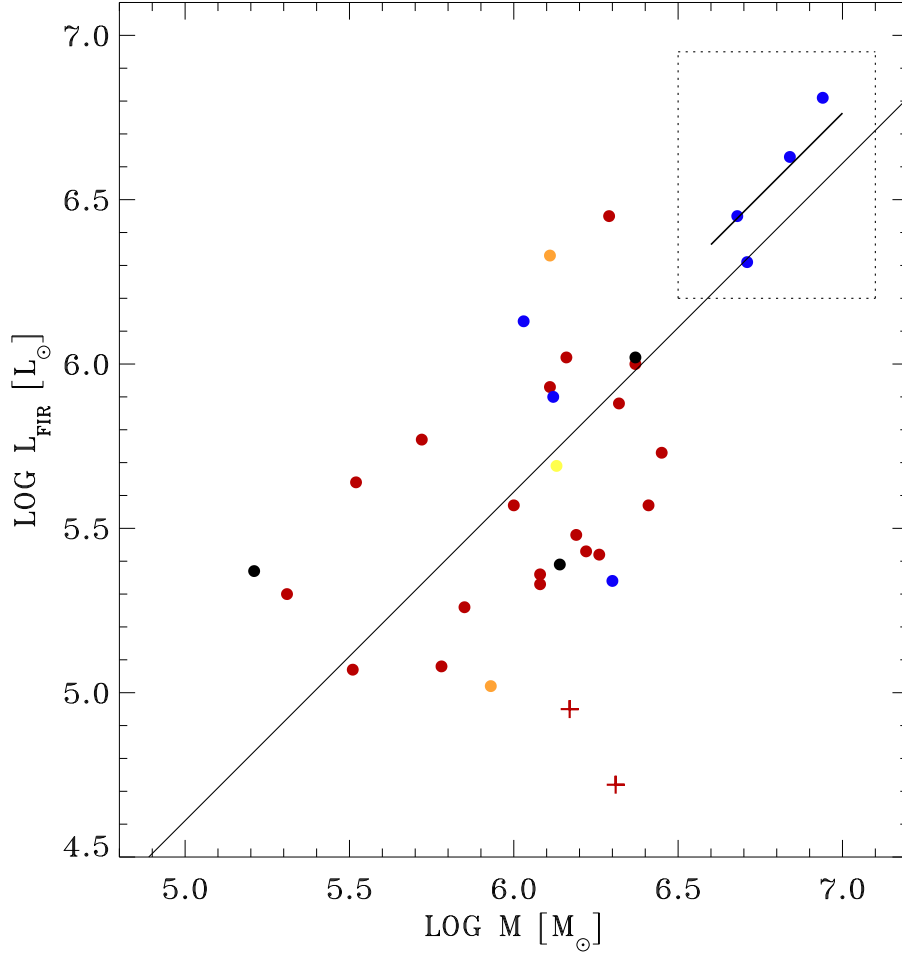


Fig. 12.—: Logarithm of the Far-Infrared luminosity in Table 4 vs. molecular mass of GMCs. Only clouds with more than one IRAS/CS source associated are included in the figure. The straight line is a least-squares fit given by $\log L_{\text{FIR}} = -0.39 + \log M(H_2)$. Colors are associated to spiral arms features as explained in Figure 9. Red crosses are GMCs 9 and 14 in Table 2 belonging to the *Centaurus* spiral arm, and were not considered in the fit. The straight line in the upper right square is a least-squares fit given by $\log L_{\text{FIR}} = -0.24 + \log M(H_2)$ to the four most massive GMCs in the figure. We notice that the most intense massive star formation activity takes place in the *Norma* spiral arm (blue filled circles).

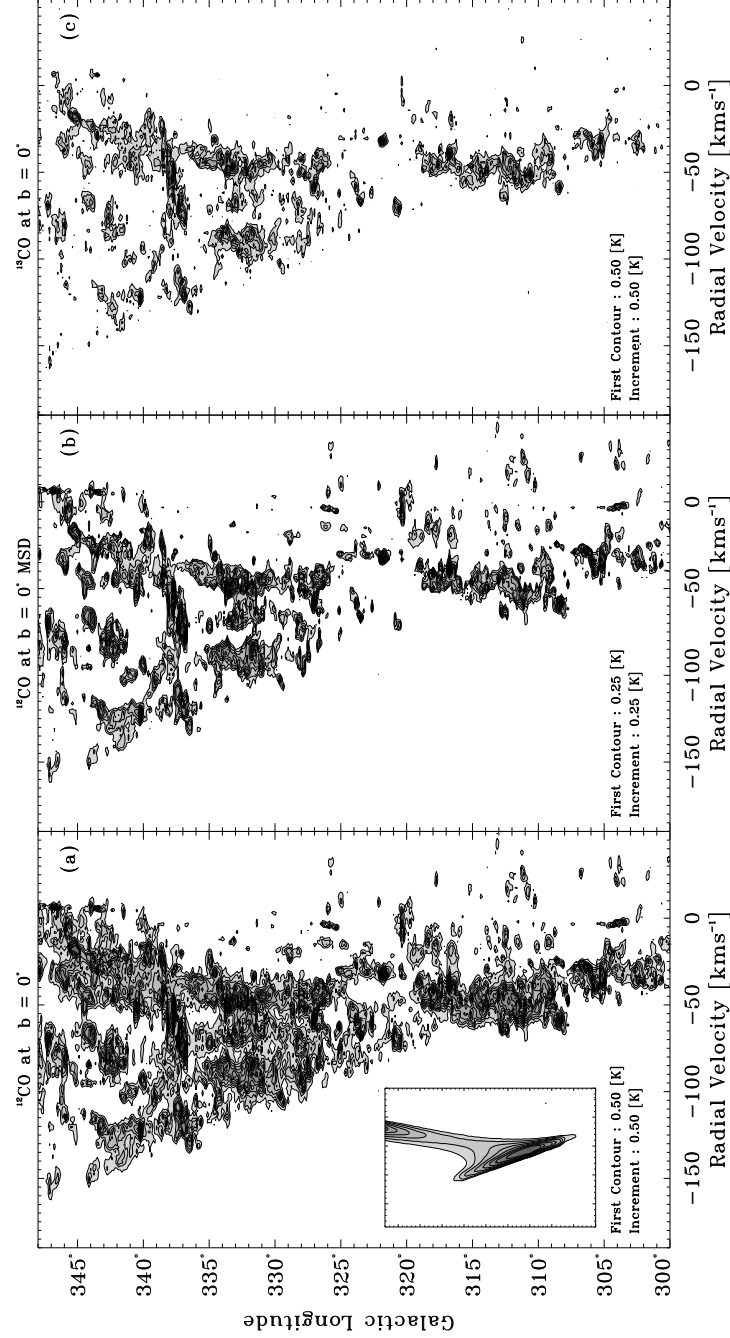


Fig. 13.—: Longitude-velocity diagrams of CO and ^{13}CO emission at $b = 0^\circ$ in the fourth Galactic quadrant. The panels represent: (a) CO observations the Columbia CO Survey. The insert on the lower left corner shows the axisymmetric model subtracted to the CO data. The first contour in the model insert is at 0.06 K degree, and contour intervals are at 0.01 K degree; (b) model subtracted CO emission; and (c) ^{13}CO Observations of the Galactic plane (Bronfman et al. 1988a). The subtraction of the axisymmetric model from the CO data dramatically improves the similitude between the ^{13}CO (tracer of higher molecular densities than CO) and the CO data.

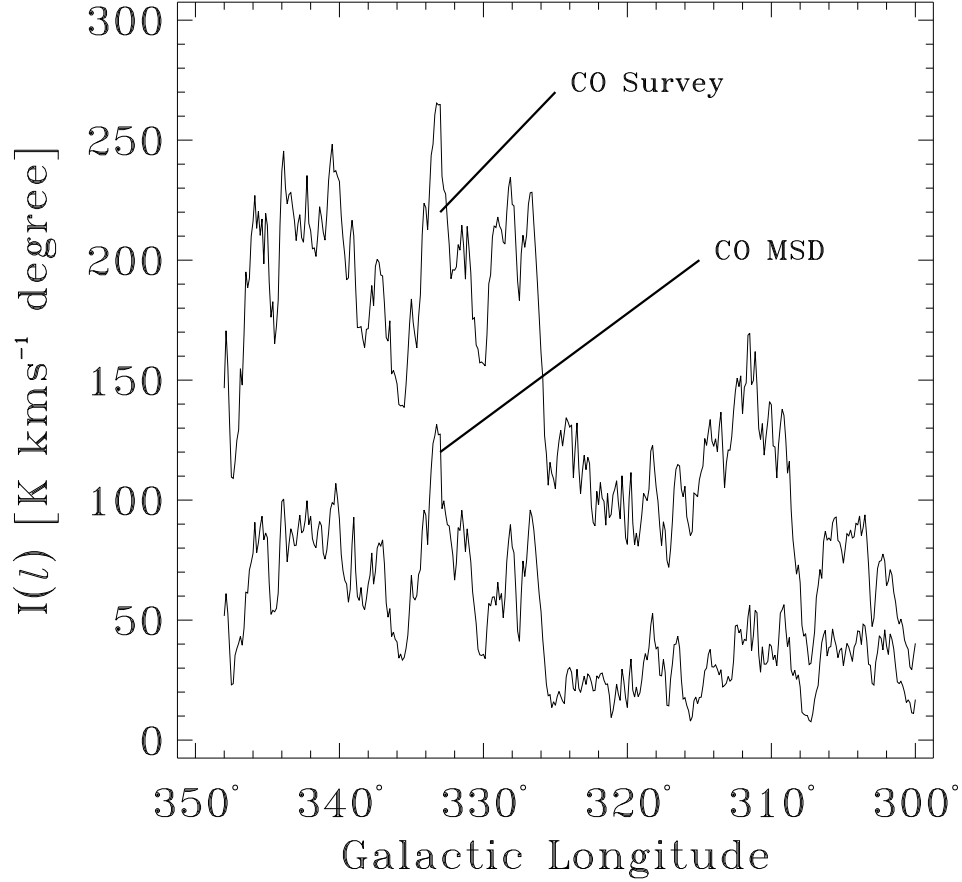


Fig. 14.—: Intensity distribution along Galactic longitude ($I(l) = \int T_A dv db$) of the Columbia Survey (CO raw data), and the model subtracted dataset (MSD). Although a large fraction of the CO emission was removed from the observed dataset by the model subtraction (63% of the non local, $|v| < 20 \text{ km s}^{-1}$, emission), the intensity structure of the emission is preserved, and features like tangent directions toward spiral arms around 309° (*Centaurus* arm), 328° (*Norma* arm), and 337° (*3-kpc expanding* arm) (Bronfman 1992) appear in both datasets.

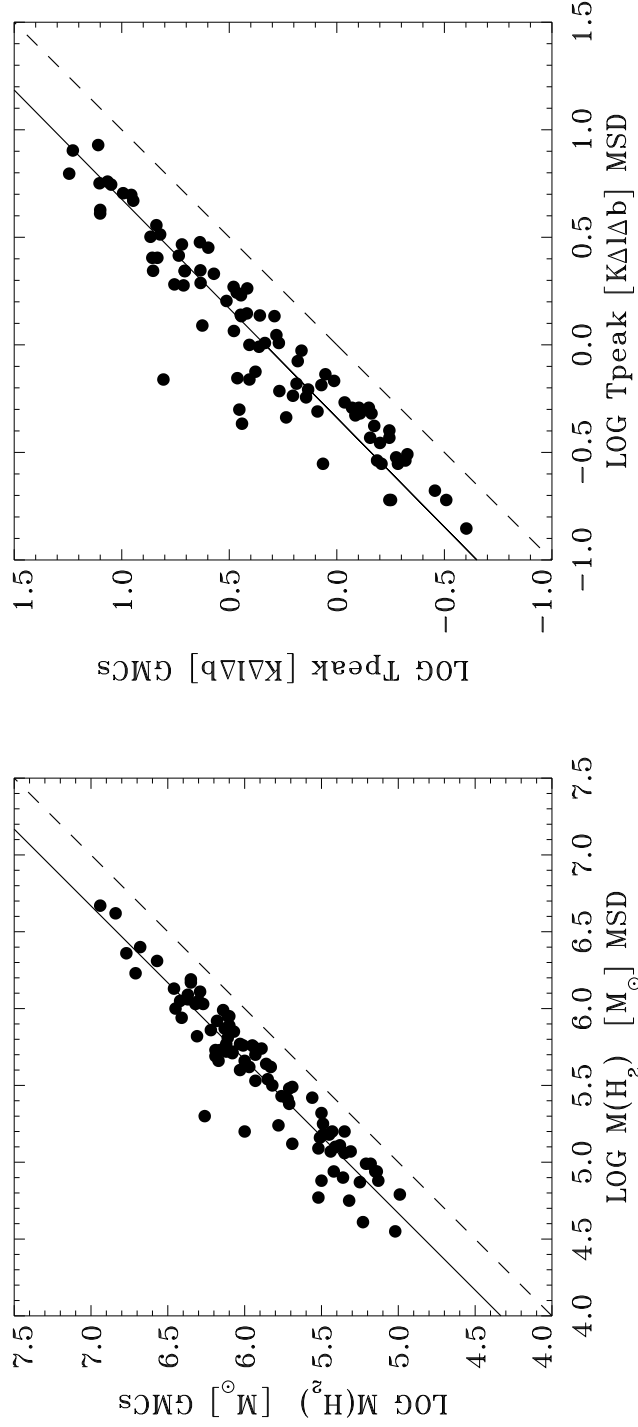


Fig. 15.—: Left panel: molecular mass of GMCs versus the molecular mass obtained from Gaussian fits in the subtracted model dataset (MSD). The solid straight line represents a proportionality fit of the form $\log M(\text{H}_2)_{\text{GMCs}} = 0.33 + \log M(\text{H}_2)_{\text{MSD}}$. Right panel: peak antenna temperature of GMCs versus the peak antenna temperature obtained from Gaussian fits in the MSD. The solid straight line represents a power law fit of the form $\log T_{\text{peak}}(\text{GMCs}) = 0.33 + 0.98 \log T_{\text{peak}}(\text{MSD})$. All values are summarized in Table 5.

Table 1. The Columbia - U. de Chile Deep CO Survey of the Southern Milky Way.

Galactic longitude	300° to 348°
Galactic latitude	−2° to +2°
Velocity coverage	−166 kms ^{−1} to +166 kms ^{−1} (300° ≤ l ≤ 335°) −180 kms ^{−1} to +153 kms ^{−1} (335° ≤ l ≤ 345°) −218 kms ^{−1} to +144 kms ^{−1} (345° ≤ l ≤ 348°)
Sampling interval	0°.125 (0°.00 ≤ $ b $ ≤ 0°.75) 0°.250 (0°.75 ≤ $ b $ ≤ 2°.00)
Telescope HPBW	0°.147
Velocity resolution	1.3 kms ^{−1}
Sensitivity ^a	$\Delta T_{rms} \leq 0.13$ K
Main Beam efficiency	$\eta = 0.82$

Note. — A detailed description of the Columbia Southern Deep CO Survey of the Milky Way can be found in Bronfman et al. (1988b, 1989).

^aAt velocity resolution of 1.3 kms^{−1}

Table 2. Giant Molecular Clouds in the Fourth Galactic Quadrant, Within the Solar Circle.

cloud	l	b	V_{lsr}	Δv ($FWHM$)	D	$D.R.$	R	M_{virial}	$M(H_2)$ GMCs
	($^\circ$)	($^\circ$)	(kms^{-1})	(kms^{-1})	(kpc)		(pc)	$\log(M/M_\odot)$	$\log(M/M_\odot)$
1	302.125	+0.750	−26.9*	12.8	2.9	N ^{a,b}	74	6.41	6.13
2	305.250	+0.375	−35.1	11.4	3.7	N ^{a,b}	54	6.17	6.16
3	305.625	−0.625	−20.7	4.7	8.0	F ^d	41	5.29	5.45
4	305.750	+1.250	−39.7*	9.6	5.0	T ^{a,e,g}	75	6.16	6.10
5	306.250	−0.375	−18.7	6.2	8.4	F ^b	45	5.56	5.49
6	308.000	−0.375	−13.2	4.7	9.3	F ^c	32	5.18	5.13
7	308.375	+0.000	−47.3*	10.8	5.3	T ^g	69	6.23	5.89
8	309.000	−0.250	−10.8	12.8	7.3	F ^{d,f}	65	6.35	5.93
9	309.125	−0.375	−40.2	11.5	3.7	N ^a	55	6.19	6.17
10	311.125	+0.125	−41.0*	12.6	3.5	N ^{a,c}	66	6.34	6.41
11	311.875	+0.125	−47.1	9.4	4.1	N ^{b,c,d}	58	6.04	6.19
12	312.375	+0.125	−11.5	10.9	10.5	F ^d	62	6.19	6.00
13	312.500	+0.125	−49.4*	6.5	5.7	T ^g	35	5.50	5.69
14	313.875	−0.125	−44.9	9.3	3.6	N ^{d,f}	65	6.07	6.31
15	314.250	+0.250	−57.6	8.0	5.2	N ^c	48	5.81	6.26
16	316.875	+0.250	−21.3	11.0	10.8	F ^d	100	6.41	6.42
17	317.750	+0.000	−17.6	12.8	11.2	F ^{c,d}	106	6.56	6.46
18	318.250	−0.375	−41.8	12.5	3.1	N ^{a,b,c}	73	6.38	6.45
19	319.375	−0.125	−20.3	7.5	11.3	F ^c	100	6.07	6.18
20	319.750	−0.375	−8.4	14.9	12.3	F ^d	82	6.58	6.27
21	320.375	+0.125	−7.8	9.0	12.5	F ^{c,d}	82	6.14	6.11

Table 2—Continued

cloud	l	b	V_{lsr}	Δv ($FWHM$)	D	$D.R.$	R	M_{virial}	$M(H_2)$ GMCs
	($^\circ$)	($^\circ$)	(kms^{-1})	(kms^{-1})	(kpc)		(pc)	$\log(M/M_\odot)$	$\log(M/M_\odot)$
22	320.750	−0.375	−66.3	11.7	4.8	N ^b	32	5.97	6.00
23	320.750	−0.250	−55.3	5.6	3.9	N ^{a,b}	34	5.36	5.52
24	321.875	+0.000	−31.6	4.7	2.3	N ^{c,d}	58	5.43	5.76
25	322.125	+0.625	−54.8	4.1	3.8	N ^{a,c}	23	4.92	5.32
26	323.500	+0.000	−65.5	4.0	4.5	N ^b	33	5.04	5.50
27	323.500	+0.625	−45.3	10.7	3.2	N ^{d,f}	22	5.72	5.23
28	323.750	−0.250	−52.3	8.0	3.6	N ^{b,c}	43	5.77	5.78
29	326.625	+0.625	−42.1	9.6	3.0	N ^{a,b,c}	56	6.04	6.11
30	327.250	−0.500	−46.7	6.0	3.3	N ^{a,c}	16	5.08	4.99
31	327.250	−0.250	−62.3	10.2	4.2	N ^c	52	6.06	6.08
32	327.750	−0.375	−70.7	11.3	4.6	N ^{c,d,f}	65	6.24	6.22
33	328.250	−0.500	−45.0	11.9	3.2	N ^{a,b,c}	54	6.21	6.08
34	328.250	+0.375	−92.0	18.4	6.0	N ^c	86	6.78	6.71
35	329.250	+0.750	−66.2	5.5
36	329.375	−0.250	−74.3	7.7
37	329.500	+0.125	−99.0	12.1	6.5	N ^c	49	6.18	6.03
38	329.500	+0.500	−80.9	9.4	5.2	N ^c	52	5.99	5.93
39	329.625	+0.125	−65.3	6.5
40	330.000	+1.000	−86.2	4.7	5.5	N ^e	21	4.98	5.02
41	331.125	−0.500	−65.0	10.6	4.3	N ^{a,b,c}	78	6.26	6.37
42	331.125	+0.000	−45.3	8.6	3.3	N ^c	43	5.83	5.82

Table 2—Continued

cloud	l	b	V_{lsr}	Δv ($FWHM$)	D	$D.R.$	R	M_{virial}	$M(H_2)$ GMCs
	($^\circ$)	($^\circ$)	(kms^{-1})	(kms^{-1})	(kpc)		(pc)	$\log(M/M_\odot)$	$\log(M/M_\odot)$
43	331.500	−0.125	−92.0	15.9	5.7	N ^{b,c}	92	6.69	6.68
44	333.000	+0.750	−48.0	5.0	3.5	N ^c	34	5.25	5.41
45	333.250	−0.375	−50.1	8.9	3.6	N ^{a,c,d}	67	6.05	6.29
46	333.625	−0.125	−88.1	9.6	5.4	N ^{b,c}	75	6.17	6.30
47	333.875	−0.375	−105.0	12.2	6.3	N ^{d,f}	70	6.34	6.19
48	334.125	+0.500	−62.2	12.2	11.1	F ^{c,d}	95	6.47	6.57
49	334.250	−0.125	−40.4	8.2	3.1	N ^{c,d}	64	5.96	6.12
50	336.000	−0.875	−48.3	7.4	3.6	N ^e	23	5.44	5.25
51	336.875	+0.125	−74.2	16.0	10.8	F ^{b,c}	121	6.81	6.84
52	337.000	−1.125	−42.2	7.4	3.3	N ^e	29	5.53	5.49
53	337.250	+0.000	−116.1	14.2	6.7	N ^c	75	6.50	6.37
54	337.750	+0.000	−55.1	18.2	11.7	F ^{b,c}	104	6.86	6.94
55	338.000	−0.125	−94.1	16.2	5.7	N ^c	57	6.50	6.03
56	338.250	−1.000	−111.5	7.4	6.4	N ^e	37	5.63	5.36
57	338.625	−0.125	−119.1	8.4	6.7	N ^{b,c}	69	6.01	6.07
58	338.875	−0.625	−45.7	6.8	3.6	N ^d	30	5.47	5.44
59	339.000	+0.625	−60.5	10.6	4.4	N ^{a,c}	35	5.93	5.71
60	339.125	+0.000	−100.3	9.3	9.9	F ^d	76	6.14	6.01
61	339.125	+0.250	−78.9	9.3	10.7	F ^{c,d}	60	6.04	5.97
62	339.500	+0.125	−111.6	6.1	6.4	N ^f	31	5.38	5.21
63	339.750	−1.250	−30.7	7.2	2.8	N ^{a,d,e}	33	5.56	5.51

Table 2—Continued

cloud	l	b	V_{lsr}	Δv ($FWHM$)	D	$D.R.$	R	M_{virial}	$M(H_2)$ GMCs
	($^\circ$)	($^\circ$)	(kms^{-1})	(kms^{-1})	(kpc)		(pc)	$\log(M/M_\odot)$	$\log(M/M_\odot)$
64	340.250	+0.000	−122.1	8.6	6.8	N ^f	77	6.07	6.14
65	340.375	−0.375	−42.9	12.3	3.6	N ^{a,c,d}	63	6.30	6.32
66	340.625	−0.625	−90.8	5.8	5.7	N ^d	68	5.68	5.86
67	340.750	−1.000	−28.9	5.5	2.7	N ^{a,e}	25	5.20	5.31
68	341.000	+0.000	−101.1	6.5	6.0	N ^{d,f}	49	5.64	5.43
69	341.375	+0.250	−24.3	8.6
70	341.500	−0.125	−129.3	11.2	7.0	N ^f	45	6.08	5.69
71	341.500	+0.000	−121.9	6.5	6.8	N ^f	37	5.51	5.35
72	342.125	+0.500	−26.6	5.4	2.7	N ^{c,d}	30	5.27	5.35
73	342.250	+0.250	−122.8	8.3	6.8	N ^f	47	5.83	5.56
74	342.625	+0.125	−41.5	5.1	12.5	F ^b	87	5.67	6.12
75	342.750	−0.500	−27.0	7.7
76	342.750	+0.000	−79.8	13.2	5.4	N ^{d,f}	75	6.44	6.35
77	343.250	+0.125	−120.1	10.3	6.7	N ^f	66	6.17	5.95
78	344.125	−0.625	−26.0	10.0	2.8	N ^c	38	5.90	5.85
79	344.500	+0.125	−68.2	12.0	5.1	N ^c	67	6.31	6.10
80	344.500	+0.125	−44.1	9.6	12.4	F ^c	131	6.41	6.77
81	345.000	−0.250	−85.9	4.3	5.8	N ^d	36	5.16	5.18
82	345.125	−0.250	−93.8	4.7	10.4	F ^d	52	5.38	5.50
83	345.125	+0.125	−119.6	14.2	6.7	N ^f	59	6.40	5.83
84	345.250	−1.000	−108.0	7.4	6.4	N ^f	37	5.62	5.15

Table 2—Continued

cloud	l	b	V_{lsr}	Δv	D	$D.R.$	R	M_{virial}	$M(H_2)$
				($FWHM$)					GMCs
	($^\circ$)	($^\circ$)	(kms^{-1})	(kms^{-1})	(kpc)		(pc)	$\log(M/M_\odot)$	$\log(M/M_\odot)$
85	345.250	−0.750	−22.1	7.0	2.6	N ^{a,b}	32	5.52	5.52
86	345.250	+1.000	−13.7	10.1	1.8	N ^{a,b}	34	5.87	5.72
87	345.875	+0.000	−36.0	7.7	3.7	N ^{c,d}	27	5.53	5.42
88	346.000	+0.000	−79.8	13.9	10.8	F ^{c,d}	90	6.56	6.35
89	346.125	−0.125	−104.9	8.3	6.4	N ^f	26	5.57	5.14
90	346.500	+1.000	−57.6	7.4	4.9	N ^{d,e}	49	5.75	5.71
91	347.000	+0.250	−118.4	7.4	6.8	N ^f	49	5.76	5.38
92	347.250	+0.000	−68.8	9.3	11.1	F ^{c,d}	61	6.04	5.94

(*).- The CO radial velocity of the cloud was corrected by $+12.2 \text{ kms}^{-1}$ in order to take into account the unusual velocity excess toward terminal velocities up to galactocentric longitude 312° reported by Alvarez et al. (1990).

(...)- The two-fold distance ambiguity could not be removed for these clouds.

Note. — The following letters represent the method in which the two-fold distance ambiguity was removed:

^a.- Spatial association with optical objects from the RWC catalog (Rodgers et al. 1960) or visual optical counterparts (Caswell & Haynes 1987).

^b.- IRAS/CS source associated to the cloud with distance ambiguity already removed.

^c.- Presence or absence of absorption features from species like H_2CO or OH against the $\text{H}\alpha$ continuum

emission from HII regions, or cold (10 - 30 K) HI absorption against the warm ($100 - 10^4$ K) HI continuum background.

^d.- Observational size-to-linewidth relationship (*Larson's Law*).

^e.- Latitude criterion.

^f.- Continuity of spiral arm.

^g.- CO radial velocity of the cloud close ($|v| < 10 \text{ kms}^{-1}$) to the tangential velocity.

Table 3:: Fitted Parameters for the Logarithmic Spiral Arms Model in the Fourth Galactic Quadrant.

Spiral Arm	r_{\circ} (kpc)	p ($^{\circ}$)	Tangent ($^{\circ}$)
Centaurus	5.40 ± 0.14	13.4 ± 2.0	310
Norma	3.72 ± 0.16	6.6 ± 2.3	330
3-kpc	2.75 ± 0.16	5.6 ± 3.0	338

Table 4. FIR Luminosity and Massive Star Formation Efficiency for GMCs.

cloud	# sources	F_{IRAS}	L_{FIR}	ϵ	cloud	# sources	F_{IRAS}	L_{FIR}	ϵ
		$(L_{\odot} kpc^{-2})$	$\log(L/L_{\odot})$	(%)			$(L_{\odot} kpc^{-2})$	$\log(L/L_{\odot})$	(%)
1	10	57344	5.69	2.4	37	4	32191	6.13	8.1
2	11	76319	6.02	4.8	38	4	13121
3	1	306	4.30	0.5	41	7	54382	6.00	2.8
4	1	1763	4.64	0.2	42	1	1462	4.19	0.2
5	1	1693	5.08	2.5	43	10	85494	6.45	3.8
8	3	1957	5.02	0.8	44	1	8433	5.00	2.5
9	3	6501	4.95	0.4	45	14	218249	6.45	9.2
10	8	30355	5.57	0.9	46	2	7361	5.34	0.7
11	3	17899	5.48	1.3	49	1	3017	4.46	0.1
13	1	1343	4.65	0.6	50	1	4492	4.76	2.1
14	3	4059	4.72	0.2	51	2	36413	6.63	4.0
15	3	9828	5.42	0.9	53	5	23309	6.02	2.9
16	1	1825	5.33	0.5	54	8	46858	6.81	4.8
17	1	797	5.00	0.2	57	1	4807	5.34	1.2
18	11	56481	5.73	1.3	59	1	3119	4.77	0.7
19	1	5874	5.88	3.2	61	1	2210	5.41	1.8
20	1	748	5.05	0.4	62	2	5697	5.37	9.4
21	2	13753	6.33	10.7	63	2	15141	5.07	2.4
22	2	16087	5.57	2.4	64	3	5286	5.39	1.1
23	1	6657	5.02	2.0	65	11	59526	5.88	2.4
24	1	321	3.24	0.0	67	2	26713	5.30	6.4
26	1	11122	5.35	4.7	69	1	1272
28	3	9132	5.08	1.3	74	2	5097	5.90	3.9
29	7	93905	5.93	4.2	76	1	2304	4.83	0.2
31	7	12227	5.33	1.1	78	5	22821	5.26	1.7
32	3	12550	5.43	1.1	79	1	13478	5.55	1.8
33	5	22562	5.36	1.3	80	1	254	4.59	0.0
34	7	55326	6.31	2.6	85	2	63312	5.64	8.5
35	1	1565	86	12	174892	5.77	7.2
36	2	6612	88	1	2196	5.41	0.7

Table 5. Peak Antenna Temperature and Molecular Mass Derived from the Model Subtracted Dataset (MSD) and GMCs.

cloud	MSD				GMCs	
	l	b	T_{peak}	$M(H_2)$	T_{peak}	$M(H_2)$
	($^{\circ}$)	($^{\circ}$)	($K\Delta l\Delta b$)	$\log(M/M_{\odot})$	($K\Delta l\Delta b$)	$\log(M/M_{\odot})$
1	302.125	+0.750	4.98	5.87	9.03	6.13
2	305.250	+0.375	2.54	5.73	6.83	6.16
3	305.625	−0.625	0.37	5.18	0.70	5.45
4	305.750	+1.250	2.83	5.95	3.96	6.10
5	306.250	−0.375	0.30	5.25	0.53	5.49
6	308.000	−0.375	0.14	4.88	0.25	5.13
7	308.375	+0.000	1.36	5.74	1.95	5.89
8	309.000	−0.250	0.54	5.70	0.92	5.93
9	309.125	−0.375	2.21	5.66	7.15	6.17
10	311.125	+0.125	4.24	5.94	12.59	6.41
11	311.875	+0.125	2.54	5.73	7.21	6.19
12	312.375	+0.125	0.28	5.66	0.62	6.00
13	312.500	+0.125	0.46	5.12	1.72	5.69
14	313.875	−0.125	4.08	5.82	12.60	6.31
15	314.250	+0.250	0.69	5.30	6.40	6.26
16	316.875	+0.250	0.66	6.05	1.54	6.42
17	317.750	+0.000	0.62	6.13	1.36	6.46
18	318.250	−0.375	6.25	6.00	17.55	6.45
19	319.375	−0.125	0.65	5.92	1.18	6.18
20	319.750	−0.375	0.35	6.03	0.63	6.27
21	320.375	+0.125	0.48	5.95	0.69	6.11
22	320.750	−0.375	0.43	5.20	2.76	6.00
23	320.750	−0.250	0.50	4.77	2.84	5.52
24	321.875	+0.000	8.01	5.43	16.88	5.76
25	322.125	+0.625	0.69	4.75	2.55	5.32
26	323.500	+0.000	0.70	4.88	2.90	5.50
27	323.500	+0.625	0.28	4.61	1.16	5.23
28	323.750	−0.250	1.23	5.24	4.22	5.78
29	326.625	+0.625	5.56	5.81	11.20	6.11
30	327.250	−0.500	0.73	4.79	1.13	4.99
31	327.250	−0.250	2.20	5.72	5.09	6.08
32	327.750	−0.375	2.21	5.86	5.10	6.22
33	328.250	−0.500	3.18	5.71	7.35	6.08
34	328.250	+0.375	1.91	6.23	5.69	6.71

Table 5—Continued

cloud	MSD				GMCs	
	l	b	T_{peak}	$M(H_2)$	T_{peak}	$M(H_2)$
	($^{\circ}$)	($^{\circ}$)	($K\Delta l\Delta b$)	$\log(M/M_{\odot})$	($K\Delta l\Delta b$)	$\log(M/M_{\odot})$
35	329.250	+0.750	0.35	...	0.96	...
36	329.375	−0.250	0.40	...	0.98	...
37	329.500	+0.125	0.58	5.60	1.60	6.03
38	329.500	+0.500	1.00	5.53	2.55	5.93
39	329.625	+0.125	0.31	...	1.01	...
40	330.000	+1.000	0.19	4.55	0.57	5.02
41	331.125	−0.500	4.68	6.09	8.84	6.37
42	331.125	+0.000	2.60	5.50	5.43	5.82
43	331.500	−0.125	3.60	6.40	6.90	6.68
44	333.000	+0.750	1.60	5.10	3.26	5.41
45	333.250	−0.375	8.49	6.11	12.87	6.29
46	333.625	−0.125	2.93	6.05	5.25	6.30
47	333.875	−0.375	0.75	5.69	2.39	6.19
48	334.125	+0.500	1.02	6.31	1.86	6.57
49	334.250	−0.125	5.64	5.77	12.68	6.12
50	336.000	−0.875	0.57	4.87	1.39	5.25
51	336.875	+0.125	1.70	6.62	2.79	6.84
52	337.000	−1.125	1.38	5.18	2.80	5.49
53	337.250	+0.000	1.36	6.06	2.78	6.37
54	337.750	+0.000	1.40	6.67	2.62	6.94
55	338.000	−0.125	0.84	5.77	1.52	6.03
56	338.250	−1.000	0.19	4.90	0.56	5.36
57	338.625	−0.125	1.37	5.85	2.28	6.07
58	338.875	−0.625	0.98	5.07	2.30	5.44
59	339.000	+0.625	1.11	5.48	1.91	5.71
60	339.125	+0.000	0.47	5.76	0.82	6.01
61	339.125	+0.250	0.29	5.62	0.65	5.97
62	339.500	+0.125	0.29	4.99	0.48	5.21
63	339.750	−1.250	1.94	5.16	4.30	5.51
64	340.250	+0.000	1.83	5.99	2.61	6.14
65	340.375	−0.375	5.07	6.03	9.85	6.32
66	340.625	−0.625	1.75	5.64	2.92	5.86
67	340.750	−1.000	2.14	5.07	3.73	5.31
68	341.000	+0.000	0.51	5.20	0.85	5.43

Table 5—Continued

cloud	MSD				GMCs	
	l	b	T_{peak}	$M(H_2)$	T_{peak}	$M(H_2)$
	($^{\circ}$)	($^{\circ}$)	($K\Delta l\Delta b$)	$\log(M/M_{\odot})$	($K\Delta l\Delta b$)	$\log(M/M_{\odot})$
69	341.375	+0.250	0.75	...	1.73	...
70	341.500	−0.125	0.42	5.49	0.67	5.69
71	341.500	+0.000	0.40	5.20	0.57	5.35
72	342.125	+0.500	2.22	5.06	4.31	5.35
73	342.250	+0.250	0.51	5.42	0.71	5.56
74	342.625	+0.125	0.49	5.72	1.23	6.12
75	342.750	−0.500	1.92	...	3.61	...
76	342.750	+0.000	3.00	6.19	4.33	6.35
77	343.250	+0.125	0.94	5.76	1.46	5.95
78	344.125	−0.625	3.26	5.54	6.63	5.85
79	344.500	+0.125	1.86	5.89	3.02	6.10
80	344.500	+0.125	1.16	6.36	3.01	6.77
81	345.000	−0.250	0.51	4.99	0.79	5.18
82	345.125	−0.250	0.31	5.32	0.47	5.50
83	345.125	+0.125	0.48	5.62	0.78	5.83
84	345.250	−1.000	0.21	4.94	0.35	5.15
85	345.250	−0.750	1.89	5.09	5.16	5.52
86	345.250	+1.000	5.74	5.41	11.64	5.72
87	345.875	+0.000	0.61	4.94	1.85	5.42
88	346.000	+0.000	0.68	6.17	1.03	6.35
89	346.125	−0.125	0.19	4.94	0.31	5.14
90	346.500	+1.000	1.02	5.38	2.16	5.71
91	347.000	+0.250	0.28	5.11	0.52	5.38
92	347.250	+0.000	0.37	5.75	0.57	5.94